Summer 8-15-2021

Novel Photothermal Materials and Thermally Engineered Membranes for Solar Desalination

Sisi Cao
Washington University in St. Louis

WASHINGTON UNIVERSITY IN ST. LOUIS

Department of Mechanical Engineering and Materials Science

Dissertation Examination Committee:

Srikanth Singamaneni, Chair

Guy Genin

Young-Shin Jun

Mark Meacham

Rohan Mishra

Novel Photothermal Materials and Thermally Engineered Membranes for Solar Desalination

by

Sisi Cao

A dissertation presented to
The Graduate School
of Washington University in
partial fulfillment of the
requirements for the degree
of Doctor of Philosophy

August 2021

St. Louis, Missouri

Table of Contents

List of Figures

List of Abbreviations

PMD	Photothermal driven membrane distillation
RO	Reverse osmosis
DCMD	Direct contact membrane distillation
AMD	Air gap membrane distillation
PDA	Polydopamine
ROS	Reactive oxygen species
SOD	Superoxide dismutase
TBA	Tert-butanol
HA	Hydroxyapatite
AuNRs	Gold nanorods
LSPR	Localized surface plasmon resonance
FTCS	(Tridecafluoro-1,1,2,2-tetrahydrooctyl)-trichlorosilane
MPTES	(3-Mercaptopropyl) triethoxysilane
PPy	Polypyrrole
PEM	Polyelectrolyte
PSS	Poly(styrene sulfonate)
PAH	Poly(allyl amine hydrochloride)
BNC	Bacterial nanocellulose
PP	Polypropylene
PTFE	Polytetrafluoroethylene
PVDF	Polyvinylidene fluoride
PVA	Polyvinyl alcohol

CS	Chitosan
E.coli	*Escherichia coli*
SEM	Scanning electron microscopy
TEM	Transmitted electron microscopy
TGA	Thermogravimetric analysis
UV-vis	Ultraviolet-visible
XPS	X-ray photoelectron spectroscopy
XRD	X-ray diffraction
AFM	Atomic force microscopy
LbL	Layer-by-layer
EM	Electromagnetic
RIU	Refractive index unit

Acknowledgements

First and foremost, I would like to thank my advisor Prof. Srikanth Singamaneni who guided me well throughout my academic research. Without his invaluable supervision and continuous support during my PhD study, none of this would be possible. His enthusiasm for science and immense knowledge inspired me all the time during my academic research. Besides my advisor, I would also like to thank my PhD committee Prof. Guy Genin, Prof. Mark Meacham, Prof. Rohan Mishra, Prof. Young-Shin Jun for their valuable guidance and insightful encouragement on my research. I would like to thank the National Science Foundation (CBET-1604542) for financial support.

I would like to thank all the previous and current members of the soft nanomaterials lab: Dr. Limei Tian, Dr. Kengku Liu, Dr. Sirimuvva Tadepalli, Dr. Congzhou Wang, Dr. Hongcheng Sun, Dr. Huzeyfe Yilmaz, Dr. Bo Hu, Dr. Anushree Seth, Dr. Qisheng Jiang, Dr. Jingyi Luan, Dr. Zheyu Wang, Dr. Hamed Gholami Derami, Mr. Rohit Gupta, Mr, Prashant Gupta, Ms. Priya Rathi, Ms. Lin Liu, Ms. , Ms. Marilee Fisher, Mr. Sang hyun Park, Mr. Max Fei, Ms. Emily Lu Wang, Mr. Sang hyun Bae, Mr. Abishek Debnath, Ms. Yixuan Wang, Ms. Qingjun Zhou, Mr. Abishek Venkatesan Iyer, Mr. Jieun Yim. Their help and support made my study and life in our lab a wonderful time.

Most of all, I am indebted to my parents who have always there for me no matter where I am and for all unconditional supports and patience. Thank for being so understanding and supportive. I consider myself of nothing without them.

Finally, I would like to thank my husband, Ziyi Wang. Thank you for encouraging and supporting me to accomplish the personal goals.

Sisi Cao

Washington University in St. Louis

August 2021

ABSTRACT OF THE DISSERTATION

Novel Photothermal Materials and Thermally Engineered Membranes for Solar Desalination

by

Sisi Cao

Doctor of Philosophy in Mechanical Engineering and Materials Science

Washington University in St. Louis, 2021

Professor Srikanth Singamaneni, Chair

Although 71% of earth surface is covered with water, more than 97% of it is saltwater, and freshwater is limited to only about 2.5%. The freshwater shortage has been exacerbated due to the environmental pollution, increased agriculture needs, socio-economic development, and population growth. Among various desalination technologies, membrane distillation has gained wide attention due to its ability to treat highly saline water utilizing waste heat from industrial processes. However, the implementation of conventional membrane distillation is hindered in the remote regions and disaster-struck communities where the low-grade thermal energy from industrial plants and electricity are not readily available. To address this problem, photothermal driven membrane distillation (PMD), where membrane distillation is integrated with photothermal materials that can effectively convert light to thermal energy, has been recognized as an attractive and sustainable technology for freshwater generation. The overall objective of this work is to overcome several fundamental scientific challenges in realizing efficient PMD by exploring two key components of photothermal membranes, namely, substrates and photothermal materials.

In the first part of this work, we have designed and investigated environmentally benign substrates (hydroxyapatite (HA) nanowires) for efficient PMD. Their structure and properties of this novel substrate material have been systematically investigated to reveal their potential in replacing the widely used polymeric substrates for efficient PMD. In the second part, we have investigated high-

performance photothermal materials (polydopamine (PDA), MXene and polypyrrole (PPy)) for efficient PMD. Their excellent photothermal property, abundant functional groups and facile processability make them highly appealing in achieving high-performance PMD membranes. Taken together, this work further our understanding of the structure, properties, stability and performance of these novel materials and open up novel avenues in designing and realizing highly efficient PMD systems.

Chapter 1: Introduction and Motivation

1.1 Photothermal driven membrane distillation (PMD)

The United Nations reports that 4 billion people currently lack access to freshwater at least one month of the year in 2019, and the water crisis has exacerbated due to the environmental pollution, agriculture and population growth.[1, 2] Various desalination technologies have been developed to alleviate the stress of water scarcity.[3] Reverse osmosis (RO), which doesn't involve phase change process, accounts for more than 60% of global desalination.[4] These thermally driven desalination technologies which separates water from non-volatile contaminants by phase change process, such as multi-effect distillation and multi-stage flash distillation, accounts for 34%.[5]

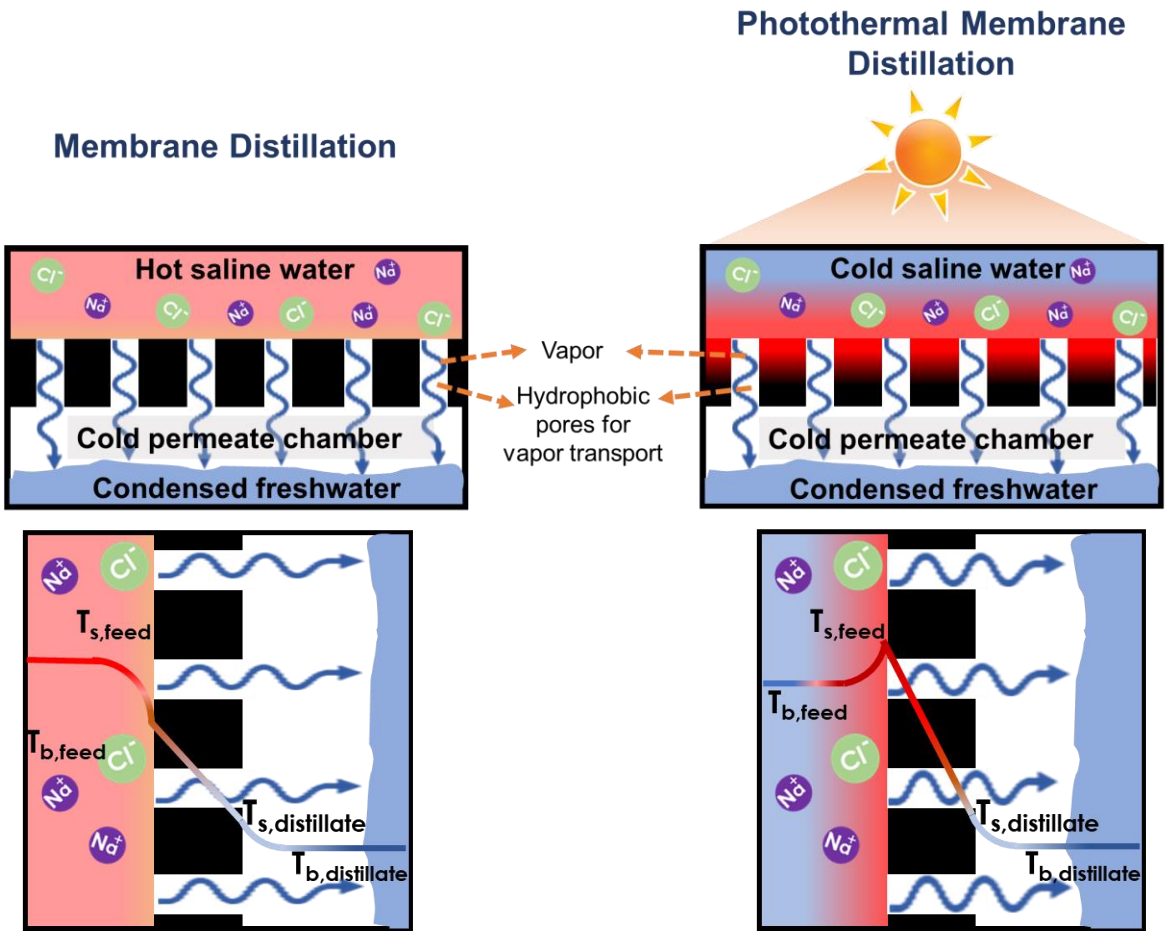

Advantages:

- Operation at low pressure.
- Utilization of low-grade heat.

Disadvantages:

- Incapability in treating cold saline water.
- Temperature polarization for reduced thermal efficiency.

Advantages:

- All advantages of membrane distillation.
- Utilization of sunlight as energy input for treating cold saline water.
- Surface heating by photothermal membrane for reduced temperature polarization.

Figure 1.1. Schematic illustration of membrane distillation and PMD.

Considering that the current desalination technologies require large energy input, membrane distillation, which enables the treatment of high-salinity water using low-grade thermal energy, has gained immense attention as a potential alternate strategy.[6-8] The membrane distillation can be performed at lower pressure compared to RO and lower temperature than conventional thermal distillation technology.[9-11] As a thermally-driven membrane-based separation process, the hot feed

saline water and cold distillate locate on the opposite sides of the porous hydrophobic membrane (Figure 1.1).[12] Driven by the vapor-pressure gradient caused by the temperature difference, the steam, generated at the interface of membrane and hot feed water, transports across the pores within the hydrophobic membrane to the cold distillate side, where the condensation occurs.[13] The merits for membrane distillation include the utilization of waste heat from industry process,[14] capability to purify high-salinity water,[15] anti-fouling property[16]. However, the implementation of conventional membrane distillation is hindered in remote regions and disaster-struck communities where low-grade thermal energy from industrial plants and electricity are not readily available. In addition, the conductive heat transfer across the membrane leads to temperature polarization and reduces the temperature difference between the feed side and permeate side, which eventually lowers vapor transfer and thus impairs desalination efficiency (Figure 1.1).[17, 18]

To overcome this inherent limitation, PMD, where membrane distillation integrates with photothermal materials to achieve local heating on the membrane surface, is proposed and validated (Figure 1.1).[19] Upon solar irradiation, the surface heating is achieved on the photothermal membrane, and the vapor is generated at the interface between the feed water and the hydrophobic photothermal membrane. Driven by the vapor pressure caused by the temperature difference across the photothermal membrane, the vapor transports from the hot feed side to the cold permeate side of the photothermal membrane, where the vapor condenses for freshwater generation. In particular, harnessing the abundant sunlight as a source of thermal energy offers great potential to extend it to developing countries and rural communities.[20] Another merit of PMD is the high thermal efficiency compared to the conventional membrane distillation process.[21-23] For conventional membrane distillation, the conductive heat transfer across the membrane leads to temperature polarization, eventually impairing desalination efficiency.[18, 24] Localized surface heating can be achieved on photothermal membranes,[25] which remarkably alleviates the temperature polarization

and results in higher thermal efficiency (Figure 1.1). For all the above-mentioned reasons, PMD is a highly promising technology to desalinate seawater or brackish water, especially for developing countries and resource-limited regions, where no power infrastructure or waste heat from industrial plants is available (Figure 1.1).

The thermal efficiency of photothermal membrane is determined by the ratio of heat flux required to generate distillate flux to the total irradiated solar flux, $\eta = \frac{\dot{m}h_{vap}}{I}$, where $\dot{m}$ represents the distillate flux of water, h_{vap} refers to the total evaporation enthalpy change, and I is the total incident solar flux. For PMD, photothermal membrane should possess excellent photothermal property, which maximizes the heat generation under sunlight irradiation for high thermal efficiency.[26] In addition, the photothermal membrane should be hydrophobic to avoid liquid water transport and porous to ensure efficient vapor transport.[21] For hydrophobic microporous membrane, only vapor can diffuse across the membrane, whereas mass transfer in liquid phase is prevented.[27] To facilitate the vapor transport, the membrane with interconnected porous structure and high porosity are highly appealing. Furthermore, the membrane should also exhibit low thermal conductivity, which can effectively reduce conductive heat for fast vapor transport. Therefore, to achieve high thermal efficiency in PMD, the photothermal membrane should possesses excellent photothermal performance, low resistance to vapor transport and high resistance to heat transfer.

1.2 Bilayered photothermal membrane using environment friendly substrates

Thermal management is essential for high efficiency of PMD. The vapor transport is driven by the pressure difference caused by the temperature difference across the membrane. The pressure difference across the membrane causes vapor transport from the hot top surface to the cold bottom layer. The larger temperature difference results in fast vapor transport. However, the conductive

heat loss across photothermal membrane leads to smaller temperature difference and thus increases resistance of the vapor transport. To achieve efficient vapor transport, bilayered photothermal membranes using substrates as a thermal insulation have been recognized promising to reduce temperature polarization.[28, 29] The substrates with low thermal conductivity can effectively reduce the conductive heat transfer across the membrane and confines the heat to the top layer. This heat localization realized by the thermal insulating layer can greatly improve the vapor transport efficiency. Owing to the importance of thermal insulation for high thermal efficiency, exploring substrates with low thermal conductivity and constructing photothermal membrane with good thermal management structure is critical for achieving high performance of PMD.

Most of the photothermal membranes reported to date employ synthetic polymers as substrates, such as polypropylene (PP),[30] polytetrafluoroethylene (PTFE)[31, 32] and polyvinylidene fluoride (PVDF),[33-36] owing to their low price, scalability and low thermal conductivity. It should also be noted that these materials have a finite lifetime owing to pore clogging, degradation, and alteration of the surface properties. The disposal of these materials poses great threats on the environment and ecosystems, because they are not biocompatible or biodegradable.[37-39] Microplastics formed due to the breakdown and degradation of polymeric substrates can have severely negative consequences on the health of ecosystems.[40] Furthermore, preparation of these membranes *via* precursor polymer powders generally involves toxic organic solvents.[19, 41, 42] Moreover, incorporation of photothermal materials on surface of these synthetic polymers is not straightforward. To assist the loading of the photothermal materials, the inert surfaces of polymer substrates have been coated with binder materials with sticky functional groups.[24] These concerns associated with utilizing synthetic polymer-based membranes highlight the need to transition to environmentally-benign substrate materials and development of simple and green processes for PMD.

1.3 Novel photothermal materials for highly efficient PMD

Photothermal materials absorb incident light and convert it to thermal energy.[26] For maximum heat generation during solar irradiation, photothermal materials should exhibit efficient light harvesting and high light-to-heat conversion efficiency.[43] To achieve excellent photothermal performance, adequate and stable deposition of photothermal materials on the supporting substrates is critical to construct highly efficient photothermal membrane.[26] However, one of challenges is the low adhesion of photothermal materials to substrates materials, leading to poor mechanical stability.[44] The addition of binder materials is required,[17] but it increases the difficulty of fabrication of photothermal materials. This problem highlights the need for exploring photothermal materials with high affinity to various substrates *via* simple and fast process. After exposing the photothermal membrane to water during solar-driven desalination, the photodegradation of photothermal materials is a concern for long-term stable performance. Various reactive oxygen species (ROS) present in water obtained from different natural sources (*e.g.*, river, lake, ocean),[45] may result in the degradation of photothermal materials. Therefore, it is important understand the fate and transformation of photothermal materials in ROS. In addition, multifunctional photothermal materials that can render functionality beyond photothermal conversion are also highly attractive. For example, biofouling accounts for 45% of all membrane fouling and leads to lower water flux in membrane-based desalination.[46-48] There is an immediate need for highly efficient and cost-effective methods that overcome biofouling on PMD. Thus, photothermal materials with multifunctionalities allowing excellent antibiofouling are highly attractive.

1.4 Research Goals and Objectives

The goal of this research effort is to design, synthesize and validate novel supporting substrate and photothermal materials for realizing environmentally benign and thermally engineered photothermally-driven membrane distillation process (Figure 1.2).

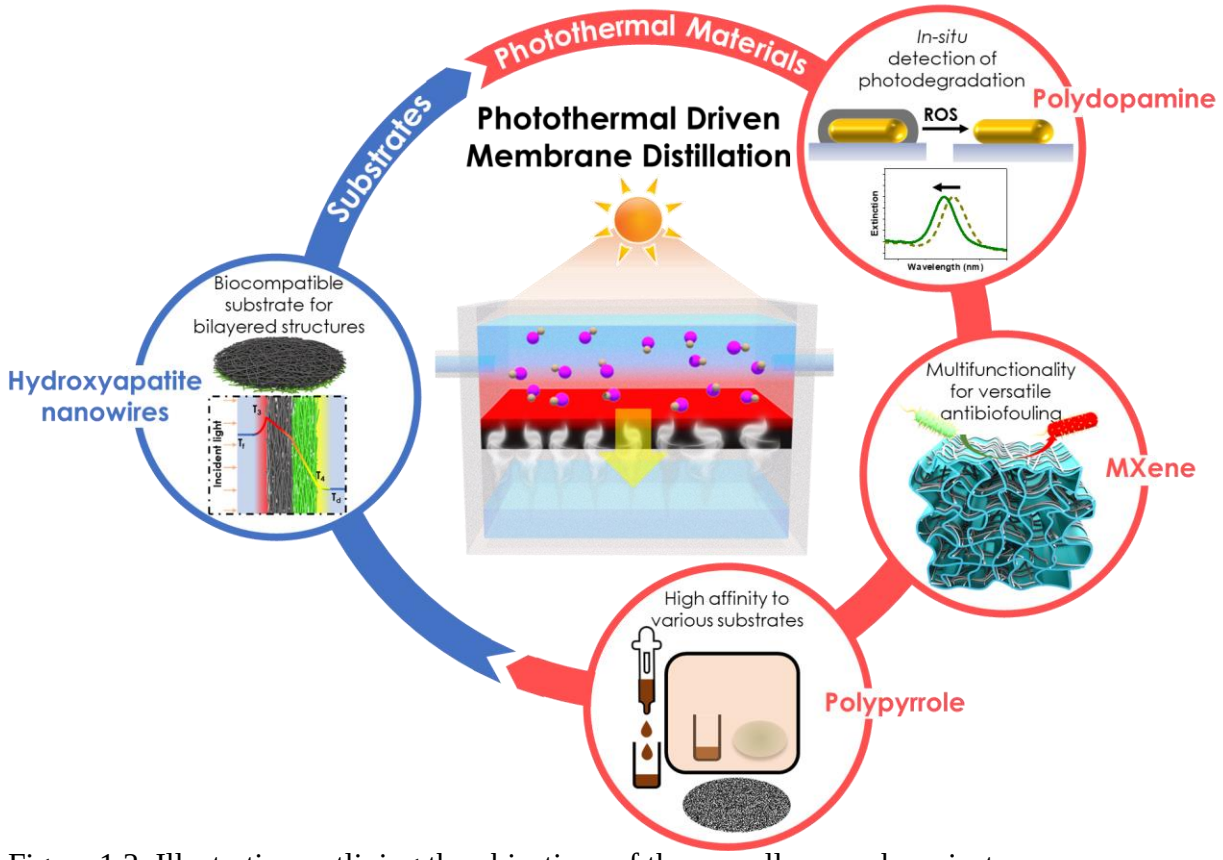

Figure 1.2. Illustration outlining the objectives of the overall research project.

Objective 1: Design and demonstrate environment-friendly substrates for thermally engineered photothermal membrane towards efficient PMD.

Objective 2: Design and demonstrate novel and efficient photothermal materials for PMD with multifunctionalities.

Objective 2A: Understand the photodegradation of PDA under ROS using plasmonic nanotransducers.

Objective 2B: Design and demonstrate a strategy of realizing multifunctional MXene aerogel for highly efficient PMD with dual-mode anti-biofouling properties.

Objective 2C: Demonstrate the universality of polypyrrole (PPy) as a photothermal material on various commercial polymeric substrates to achieve efficient PMD.

1.5 Overview of the Dissertation

The current chapter (Chapter 1) provides an overview of the research efforts and provides a brief background of photothermal membranes in terms of substrates and photothermal materials for highly efficient PMD performance.

Chapter 2 describes a highly efficient bilayered photothermal membrane based on hydroxyapatite (HA) nanowires for highly efficient PMD. The abundant functional groups of HA nanowires allow easy and fast coating of PDA for excellent photothermal performance, and the low thermal conductivity of HA nanowires can effectively reduce conductive heat loss. We demonstrate that HA nanowires is a promising material platform to realize high-performance photothermal membranes for PMD, owing to the excellent biocompatibility, mechanical flexibility, low thermal conductivity, easy processability, and facile surface modification.

In Chapter 3, we investigate photodegradation of PDA by probing the localized surface plasmon resonance (LSPR) shift of PDA-coated gold nanorods (AuNRs). The AFM results confirm the reliability of plasmonic nanosensor in revealing the degradation of the PDA layer. Compared to conventional methods such as AFM, plasmonic nanosensors enable fast and *in-situ* detection. Using the plasmonic nanotransducer, we successfully probe real-time chemical transformation of PDA during its dissolution and understand the photodegradation of PDA under different ROS condition.

Chapter 4 describes MXene composite aerogel for highly efficient PMD with dual-mode antimicrobial capability. Structural and chemical optimization of the MXene composite aerogel rendered high porosity and low thermal conductivity material, which in turn resulted in high thermal efficiency and long-term chemical stability during PMD. In addition, photothermally-driven and electric field-driven antibiofouling performance is achieved on the MXene composite aerogel because of excellent photothermal property and electrical conductivity of MXene. The

multifunctionality of MXene make it promising in realizing highly efficient, stable and biofouling-resistant photothermal membrane for high-performance PMD.

In Chapter 5, we introduce universal deposition of PPy on different polymeric membranes for efficient PMD. Using a two-step chemical vapor polymerization, PPy is deposited on different commercial polymer substrates for realizing excellent photothermal performance, regardless of surface energy and curvature of supporting substrates. The thin and conformal coating of PPy on the polymer substrates results in preserved interconnected porous network. In addition, the deposition is highly stable under vigorous mechanical agitation. We demonstrate that the universal PPy coating can be easily and quickly deposited on various substrates to achieve high thermal efficiency in PMD.

Chapter 2: Polydopamine/Hydroxyapatite Nanowire-based Bilayered Membrane for Photothermal Driven Membrane Distillation

2.1 Abstract

In developing countries and resource-limited regions, where no power infrastructure or waste heat from industrial plants is available, photothermal driven membrane distillation (PMD) has been recognized as an attractive and sustainable technology for freshwater generation. PMD enables easy water collection, inherent fouling resistance, low-pressure operation, and high-salinity water treatment. Hydroxyapatite (HA) nanowires with excellent mechanical flexibility owing to their high aspect ratio, low thermal conductivity, easy surface modification and scalable production offer great potential for highly efficient membrane distillation. Herein, we demonstrate that the environmental-benign HA nanowires-based bilayered film offers the highest photothermal efficiency (62%) and water flux (0.89 $kg \bullet m^{-2} \bullet h^{-1}$) with 1-sun irradiation (1 $kW \bullet m^{-2}$), among the

exiting PMD systems without auxiliary heating or multilayer heat recovery reported so far. The hierarchical porous structure formed by the remarkably flexible and intertwined HA nanowires allows low resistance to vapor transport, which is critical for high water flux. Simultaneously, the low thermal conductivity of the thermal insulator layer comprised of HA nanowires prevents conductive heat transfer across membrane, which significantly enhances the thermal efficiency of the membrane. The completely biocompatible, scalable, and thermally-engineered bilayered film demonstrated here achieves highly efficient PMD.

2.2 Introduction

Although 71% of earth surface is covered with water, more than 97% of it is saltwater, and freshwater is limited to only about 2.5%.[1] The water crisis has been exacerbated due to environmental pollution, increased agriculture needs, socio-economic development, and population growth.[49, 50] Among various desalination technologies, membrane distillation has gained wide attention due to its ability to treat highly saline water utilizing waste heat from industrial processes.[5-7, 14, 51, 52] The membrane distillation process can be carried out at a lower pressure compared to reverse osmosis (RO) and at a lower temperature than conventional thermal distillation technology.[9-11] In membrane distillation system, the hot feed saline water and cold distillate are present on opposite sides of a porous hydrophobic membrane.[12] Driven by the vapor-pressure gradient caused by the temperature difference, the steam, generated at the interface of membrane and hot feed water, transports across the membrane to the cold distillate side, where condensation occurs.[13] However, the implementation of conventional membrane distillation is hindered in remote regions and disaster-struck communities where low-grade thermal energy from industrial plants and electricity are not readily available.

To address this problem, photothermal-driven membrane distillation (PMD), where membrane distillation is integrated with photothermal materials that can effectively convert light to thermal

energy, is being proposed.[19, 53-55] In particular, harnessing the abundant sunlight as a source of thermal energy offers great potential to propel it to developing countries and rural communities. Another merit for PMD is the high thermal efficiency compared to the conventional membrane distillation process.[21-23] For conventional membrane distillation, the conductive heat transfer across the membrane leads to temperature polarization, eventually impairing desalination efficiency.[18, 24] Localized surface heating can be achieved on photothermal membranes,[25] which remarkably alleviates the temperature polarization and results in higher thermal efficiency.

Most of the photothermal membranes reported to date employ synthetic polymers, such as polypropylene (PP),[30] polytetrafluoroethylene (PTFE)[31, 32] and polyvinylidene fluoride (PVDF),[33-36] as substrates, which are non-biocompatible and non-biodegradable. The disposal of these materials poses a great threat to the environment and ecosystems.[37] Preparation of these membranes *via* precursor polymer powders generally involves toxic organic solvents.[19, 41, 42] Moreover, incorporation of solar absorbers on surface of these synthetic polymers is not straightforward. To assist the loading of the solar absorbers, the inert surfaces of polymer substrates have been coated with binder materials with sticky functional groups.[24] These concerns associated with utilizing synthetic polymer-based membranes highlight the need to transition to environmentally-benign membrane materials and to develop simple and green processes for PMD. As a major inorganic mineral in bone and tooth of vertebrates, hydroxyapatite ($Ca_{10}(PO_4)_6(OH)_2$, HA) is well-known for its biocompatibility, biodegradability, and abundance.[56, 57] HA nanowires with a high aspect ratio of length to diameter (> 100) exhibit remarkable mechanical flexibility,[58] and they can be assembled into a flexible film by simple vacuum filtration. The film possesses an interconnected porous network and allows facile transfer of vapor across the film.[59] Owing to their low thermal conductivity, HA nanowires-based films have been employed as thermal insulators in solar steam generators to enhance localized surface heating.[60] Moreover, the

hydrophilicity/hydrophobicity of the HA nanowires can be readily tuned by harnessing hydrogen bonding *via* hydroxyl groups or electrostatic interaction *via* charged moieties (*e.g.*, Ca^{2+} ions), which enable facile surface modification.[61, 62] For those reasons, we posit that the biocompatibility, mechanical flexibility, low thermal conductivity, easy processability, and facile surface modification of HA nanowires make them as a promising material platform to realize high-performance photothermal membranes for PMD.

Herein, we introduce a highly efficient bilayered photothermal membrane based on HA nanowires with low resistance for vapor transport and high resistance for heat transfer. For this bilayered structure, the top layer comprises polydopamine (PDA)-coated HA (HA@PDA) nanowires to effectively convert solar energy to heat and a bottom layer comprises chitosan (CS)-bonded HA nanowires (HA-CS) as a thermal insulator (Figure 2.1). The CS in the bottom layer serves as a bio-degradable molecular glue. The hierarchical structure formed by the highly flexible and intertwined HA nanowires provides a network of channels for facile vapor transport. In addition, the easy surface modification and large surface area of HA nanowires allow dense coating of PDA that is a highly biocompatible and biodegradable solar absorber.[39, 63, 64] More importantly, the HA nanowires with low thermal conductivity can significantly reduce the conductive heat transfer across the membranes and increase the thermal efficiency in PMD. Although bilayered structures have been applied in PMD, the importance of a thermal insulator has not been well studied. Our work represents the first detailed study elucidating the role of thermal insulation layer in achieving high photothermal efficiency in PMD. This completely environmentally-friendly bilayered photothermal film exhibits outstanding light absorption, heat insulation, stability, and porosity, leading to high thermal efficiency in PMD. This work illuminates the great potential of HA nanowires in constructing a high-performance and environmentally-friendly photothermal membrane *via* a simple and green processing method.

2.3 Experimental Section

Preparation of hydroxyapatite (HA) nanowires

HA nanowires were synthesized by the calcium oleate precursor solvothermal method reported previously.[62] For all experiments, unless otherwise mentioned, we have used deionized water (≥ 18.2 MΩ-cm, Barnstead). Briefly, sodium hydroxide (NaOH, Sigma Aldrich) aqueous solution (1.73 M, 56.3 ml), calcium chloride ($CaCl_2$, Sigma Aldrich) aqueous solution (250 mM, 45 ml), and sodium dihydrogen phosphate dihydrate ($NaH_2PO_4 \cdot 2H_2O$, Alfa Aesar) aqueous solution (333 mM, 67.5 ml) were added to the mixture of H_2O (50.6 ml), methanol (22.5 ml) (Sigma Aldrich), and oleic acid (35.1 g) (Sigma Aldrich) under stirring, respectively. Then, the mixture was transferred to a Teflon-lined stainless-steel autoclave (Parr Co., Moline, IL) and maintained at 180 ˚C for 24 h. The precipitates were centrifuged at 1500 rpm for 5 min and the supernatant was decanted. The collected product was dispersed in the mixture of ethanol (95%, Sigma Aldrich) and deionized water with volume ratio of 1 to 1. The mixture was centrifuged at 1500 rpm for 5 min, and the supernatant was subsequently removed. This wash step was repeated for three times. Finally, the products were dispersed in deionized water and the supernatant was decanted after centrifuging at 4000 rpm for 5 min. The rinsing step was repeated for three times and the final products were dispersed in deionized water. To determine the HA concentration, the HA suspension (1 ml) was dried in the 70 °C oven for overnight, and the weight of dry HA was measured.

Preparation of polydopamine (PDA)-coated HA (HA@PDA) nanowires

To ensure the uniform dispersion of HA nanowires in solution, HA nanowires (20 mg) were dispersed in Tris-HCl buffer solution (10 mM, pH = 8.5, 50 ml) followed by sonication for 1 min. Then dopamine (20 mg, Sigma Aldrich) was added to the above suspension, followed by stirring for 24 h in open air to get the homogeneous PDA coating on HA nanowires. Finally, the resultant

products were collected, and to remove the salt and PDA nanoparticles, they were washed with deionized water for three times by centrifuging at 6000 rpm for 5 min. The collected products were dispersed in deionized water.

Preparation of HA-CS film, HA@PDA film, and HA@PDA/HA-CS bilayered film

The chitosan (CS) powders (200 mg, Sigma Aldrich) were dispersed in the acetic acid (Sigma Aldrich) aqueous solution (1% v/v, 10 ml), and the mixture was kept in an oil bath at 60 ˚C for 2 h under stirring to obtain a homogenous solution. CS solution (20 mg/ml, 111 μl) was added to HA nanowires suspension (1 mg/ml, 20 ml), and the mixture was left on a rotating mixer for 10 min to ensure uniform coatings of CS on the HA nanowires. The mixture of CS and HA was homogenous, and no aggregation was observed. Then, the mixture was vacuum-filtered through hydrophilic polypropylene (PP) membrane (diameter = 90 mm, pore size = 0.45 μm, Cole-Parmer) to fabricate the HA-CS film. Once all water passed through the filter, the film was dried at 60 ˚C for 10 min. The HA-CS film was obtained by peeling from the membrane filter.

The HA@PDA film was also obtained by vacuum-filtering HA@PDA nanowires suspension (20 mg) on PP membrane. To obtain the HA@PDA/HA-CS bilayered film, the above mixture (10 ml) of HA nanowires and CS was vacuum-filtered on PP membrane. Once all water passed through the filter, the HA@PDA nanowires suspension (1 mg/ml, 10 ml) was vacuum-filtered on the top surface of HA-CS film. The film was dried at 60 ˚C for 10 min and finally the HA@PDA/HA-CS bilayered film was peeled from the membrane filter.

In both membrane preparation, the peeling process does not affect the mechanical strength.

Preparation of PDA hollow nanowires

HCl solution (1M, Sigma Aldrich) was used to dissolve the HA nanowires from the core of the HA@PDA nanowires. After adding HCl solution to HA@PDA nanowires suspension, the mixture

was vortexed for 5 s and then washed with deionized water for three times by centrifuging at 6000 rpm for 10 min. The collected the products were dispersed in deionized water.

FTCS treatment

To obtain the hydrophobic surface, the obtained films were treated with (tridecafluoro-1,1,2,2-tetrahydrooctyl)-trichlorosilane (Sigma Aldrich) vapor in a sealed container at 70 ˚C for 24 h. Then, to confirm the hydrophobic surface modification after FTCS treatment, water contact angle of films was measured using a contact angle analyzer (Phoenix 300, Surface Electro Optics Co. Ltd).

Nano-/Micro-structure characterization

SEM images of the surface and the cross section of the films and the nanowires were obtained after sputter coating the samples with gold. FEI Nova 2300 field-emission scanning electron microscope (SEM) was used at an acceleration voltage of 10.5 kV. The transmission electron microscope (TEM) images of nanowires were obtain using JEOL JEM-2100F field emission microscopy. Thermogravimetric analysis (TGA) was performed using TA Instruments Q5000 IR Thermogravimetric Analyzer in nitrogen gas flow (at rate of 10 °C•min^{-1}). The pore size distribution of films was measured by a CFP-LEP-1100A capillary flow porometer. Zeta potential measurements were performed using a Zetasizer Nano ZS (ZEN3600) dynamic light scattering system (Malvern Instruments).

Thermal conductivity measurement

The thermal conductivities of HA-CS film and HA@PDA film were measured by monitoring the temperature distributions across the thickness of films that were sandwiched between two glass microscope slides. The bottom glass slide was in contact with a hot plate and the top glass slide was in contact with ice. The temperature of hot plate was increased from 70 °C to 120 °C, in steps of 10 °C. The vertical temperature distribution for the sandwich was monitored by a high-speed IR camera (Telops FAST M3k). The emissivity coefficient of a glass slide and a sample was

assumed to be 0.9 to obtain the temperature distribution.[39] Fourier equation was used to calculate the thermal conductivity of each sample:

$$q' = K\frac{\Delta T}{\Delta X}$$

The heat flux ($q^{'}$) was calculated by assuming the thermal conductivity (K) of 1.05 $W \bullet m^{-1} \bullet K^{-1}$ for glass slides. Because the glass slide and samples experience the same heat flux, the heat flux value obtained for glass slide was used to measure the thermal conductivity for HA-CS film and HA@PDA film samples, respectively.

Optical properties and photothermal performance measurement

Reflectance and transmittance spectra of films were obtained using a CRAIC micro spectrophotometer (QDI 302) coupled to a Leica optical microscope (DM 4000M) with 20x objective in the range of 450–800 nm with 10 accumulations and 100 ms exposure time in reflection and transmission mode, respectively. The surface temperature of films was monitored by an IR camera (Ti 100, FLUKE) under light illumination using a solar simulator (Newport 66921 Arc Lamp) under both unfocused irradiation (1 sun) and focused irradiation (9 sun).

Photothermal driven membrane distillation performance measurement

The PMD performance was evaluated using a direct contact membrane distillation (DCMD) module. The PMD cell was constructed using acrylonitrile butadiene styrene (ABS) plastic by 3D printing. The diameter for membrane distillation cell was 1.5 cm. A Teflon substrate with thickness of 1 mm was placed between the feed side and distillate side to support the photothermal membrane. The 0.5 M NaCl aqueous solution was chosen to simulate the seawater as the feed water and deionized water was chosen as distillate stream at the bottom of the membrane, both of which were at room temperature (20 °C). The feed and distillated water were continuously circulated using two peristaltic pumps (Welco WPX1-F1 and Stenner 85MHP5), with a flow rate

of 3.6 ml•min^{-1} and 16.2 ml•min^{-1}, respectively. The thickness of feed water was maintained at 8 mm. The collected permeate water was recorded using a weight scale (Sartorius ELT402) to measure the weight of the distillate reservoir every 2 min. The light illumination to DCMD was achieved using a solar simulator (Newport 66921 Arc Lamp) under both 1 and 9 sun illumination.

Mechanical agitation

The HA@PDA/HA@-CS film (1 cm x 1 cm, L x W) was placed in a 50 ml test tube filled with water, then it was subjected to rigorous mechanical agitation a tube rotator (VWR Multimix Tube Rotator Mixer 13916-822) for 2 weeks.

Liquid entry pressure calculation

The liquid entry pressure of HA@PDA and HA@PDA/HA-CS film was calculated based on the Cantor–Laplace equation.[65, 66]

$$LEP = \frac{-2B\gamma_L Cos\theta}{r_{max}}$$

where LEP was the liquid entry pressure of pure water in Pa, B represented a dimensionless geometrical factor that includes the irregularities of the pores (B = 1 for assumed cylindrical pores), γ_L referred the liquid surface tension in N•m^{-1} (in this case water at 20°C, 0.07286 N•m^{-1}), θ represented the contact angle in degree, and r_{max} was the maximal pore radius in m (non-closed pore, r_{max} = 0.86 x 10^{-6} m according to the measurement of flow capillary porometry).

2.4 Results and Discussion

The PDA/HA nanowires bilayered film was fabricated by sequential vacuum filtration of HA-CS and HA@PDA nanowires (Figure 2.1). The fabrication process is fast and scalable compared to freeze-drying and physical/chemical vapor deposition. HA nanowires were synthesized by a previously reported calcium oleate precursor *via* hydrothermal method, and large-scale synthesis (with a volume up to 100 L) could be achieved using a large stainless-steel autoclave.[62] HA

nanowires with diameter of around 20 nm and high aspect ratio (>100) exhibited remarkable flexibility (Figure 2.2A, B). After dispersing in water, a stable wool-like suspension was observed (inset of Figure 2.2A). CS, a biopolymer that enables strong interfacial interaction (*e.g.*, hydrogen bonding and electrostatic interaction) with the nanowires, is added to improve the mechanical stability for the HA-CS film.[58]

To fabricate the HA-CS film (thermal insulation layer), the mixture of HA nanowires suspension with 10% (w/w) CS was vacuum filtered. The as-prepared pristine HA-CS film was white (Figure 2.2D) and the intertwined nanowires formed an interconnected porous network (Figure 2.2E). The pore size of HA-CS film was analyzed by flow capillary porometry and the mean diameter for pores was found to be around 200 nm (Figure 2.3A). Thermogravimetric analysis (TGA) showed that the loading of CS was around 4% (w/w) for the pristine HA-CS film (Figure 2.3B), which was found to be an optimal loading amount for a stable HA-CS film. In contrast, the film fabricated using a mixture of HA nanowires suspension with 5% (w/w) CS could not be successfully peeled from the filter membrane as they broke and disintegrated during the peeling process, suggesting that the HA nanowires are not firmly bound together (Figure S1.1). Higher loading of CS is also detrimental to the PMD performance as it compromises the porosity of the film. Therefore, the optimal loading of CS, which serves as the binding material, is important to ensure mechanical stability of the film and high PMD performance.

In this work, photothermally-active PDA was used as the solar absorber, because of its excellent biocompatibility, biodegradability, broadband light absorption and high light-to-heat conversion efficiency.[53, 67] To obtain PDA coating, HA nanowires were dispersed in the 10 mM Tris-HCl solution (pH = 8.5) followed by the addition of dopamine. PDA was formed *via* oxidative self-polymerization of dopamine and the reaction was stopped after 24 hours. The coating resulted in a color change of HA nanowires suspension from white (inset of Figure 2.2A) to dark brown (inset

of Figure 2.2F). Transmission electron microscope (TEM) images revealed the ultrathin PDA coating on the HA nanowires surface, and the surface became significantly rougher (Figure 2.2G) than the pristine HA nanowires (Figure 2.2B). The successful coating was confirmed by the PDA nanotubes obtained after dissolving the HA nanowire cores by HCl, and the thickness for the PDA shell was found to be around 15 nm (Figure S1.2A). The isoelectric point (pH_{iep}) of pristine HA nanowires was around 2.3, whereas that of HA@PDA suspension was around 4, which is similar to pure PDA and PDA coated surfaces,[68, 69] indicating the successful coating of PDA on HA nanowires (Figure S1.2B).

To validate the importance of incorporating HA-CS layer as a thermal insulator in PMD, a HA@PDA film with same thickness, consisting of only a solar absorber layer without a thermal insulating layer (HA-CS layer), was fabricated as a comparison. The HA@PDA film was obtained by vacuum filtering the HA@PDA nanowires. In stark contrast with the white color of pristine HA-CS film (Figure 2.2C), the HA@PDA film was dark brown (Figure 2.2H). The interconnected pores were also observed for the HA@PDA film, with mean diameter of 230 nm (Figure 2.3A). Based on TGA analysis, the weight percentage for PDA in the HA@PDA film was around 20% (Figure 2.3B), which was achieved by 24-hours oxidative self-polymerization of dopamine on HA nanowires. It is important to note that the PDA loading efficiency achieved here is much higher than reported in the case of hydrophilic PVDF film (9.7%) after seven polymerization cycles (each cycle for 24 hours).[53] The difference is ascribed to the much larger surface area of HA nanowires compared to the porous PVDF membrane. HA nanowires were dispersed in the dopamine solution and provided a significantly larger surface for *in situ* PDA coating compared to PVDF membrane. Considering that adequate PDA loading is critical for effective light absorption and solar energy harvesting, HA nanowires offer a unique advantage as templates for PDA loading.

To obtain the bilayered HA-CS/HA@PDA film, HA@PDA nanowires were vacuum-filtered on the surface of HA-CS film (Figure 2.1). The color of upper layer (Figure 2.2K) and bottom layer (Figure 2.2L) of the as-prepared hybrid film was the same as HA@PDA film and HA-CS film, respectively, which confirmed the bilayered structure. Owing to the mechanical flexibility of the HA nanowires, HA-CS film, HA@PDA film, and the bilayered films could be easily bent without inducing brittle fracture (Figure 2.2D, I, M). A nacre-like multilayered structure was observed in the cross-section of bilayered film (Figure 2.2N-O) and HA@PDA film (Figure S1.3A-B), resulting from the physical and chemical interactions between the nanowires (*e.g.*, physical entanglements, hydration forces, van der Waals interaction, hydrogen bonding and electrostatic interaction).[61] These available pores and interlayer spacings in the films will provide sufficient channels for effective vapor transport during the PMD operation.

Considering that the heat transfer resistance of the membrane plays a key role in the thermal efficiency of MD, we investigated the thermal conductivity of HA@PDA film and HA-CS film, which constitute the top and bottom layers of the hybrid film, respectively. The measurements were conducted according to our previously reported method.[70] The film was sandwiched between two glass slides, with the top glass slide in contact with ice and the bottom one in contact with a hot plate, which was employed as heat source to establish heat flow (the temperature was increased from 70 °C to 120 °C with an interval of 10 °C). The temperature gradient along cross-section film was monitored by an infrared camera (insets of Figure 2.3C-D). The thermal conductivity for HA-CS film was measured to be 0.048 $W \bullet K^{-1} \bullet m^{-1}$ (Figure 2.3C), which is comparable to the widely used thermal insulator materials for interfacial heating systems, such as polystyrene foam (0.040 $W \bullet K^{-1} \bullet m^{-1}$).[71] On the other hand, the HA@PDA film exhibited a thermal conductivity of 0.147 $W \bullet K^{-1} \bullet m^{-1}$ (Figure 2.3D), which is three times higher than the HA-CS film. The low thermal conductivity of HA-CS film makes it as an excellent thermal insulator. Under light illumination,

the thermal energy is generated in HA@PDA layer at the top and the HA-CS film at the bottom reduces the conductive heat transfer across the membrane. Therefore, the enhanced heat localization enabled by including the thermal insulator can significantly reduce the temperature polarization, which offers a higher driving force for vapor transport across the membrane and greatly improves the thermal efficiency of the photothermal membrane.

The hydrophobicity of membrane is critical for MD process.[14, 27, 72, 73] For hydrophobic microporous membranes, only vapor can to diffuse across the membrane, whereas mass transfer of liquid phase is prevented. Although as-prepared HA nanowires are highly hydrophilic, their facile surface modification allows easy hydrophobization. The films were subjected to fluorosilanization using (tridecafluoro-1,1,2,2-tetrahydrooctyl)-trichlorosilane (FTCS) to obtain a hydrophobic surface.[74] SEM images confirmed that the porous network was not affected by FTCS treatment (Figure S1.5), and contact angle measurement indicated the successful hydrophobic modification. The original surfaces of HA-CS film (Figure S1.4A), HA@PDA film (Figure S1.4B) and bilayered films (Figure S1.4C-D) were hydrophilic with water contact angles of 0°, following hydrophobization, the contact angles were 120°, 130°, and 126°, respectively (insets of Figure S1.5).

To investigate the light absorption of and HA@PDA/HA-CS film, the optical transmittance and reflectance of HA-CS, HA@PDA and HA@PDA/HA-CS film after FTCS treatment are measured and compared (with the film thickness ~70 μm) (Figure 2.4A-B). The pristine HA-CS film exhibited high transmittance (~33.3%) and reflectance (~46.2%) in the visible region, implying relatively small light extinction (~20.5%). On the other hand, the HA@PDA film exhibited extremely low light transmittance (~0%) and reflectance (~2.5%), which translated into a large extinction (~97.5%). The difference in optical properties is associated with the presence of PDA, which is known to exhibit broadband light absorption. In addition, the interconnected porous

structure of the film causes the multiple reflection within the film, enabling high light absorption.[75] Owing to the presence the HA@PDA layer at the top, the bilayered film also displayed very low light transmittance (~0%) and reflectance (~2.3%), which corresponds to a high light extinction (~97.7%). The bilayer structure of the membrane does not affect the optical properties. Hence, the large optical absorption and excellent light-to-heat conversion efficiency enabled by PDA makes the bilayered film a promising membrane for PMD.

Now, we turn our attention to the photothermal conversion efficiency of these films, which critically determines their thermal efficiency for PMD operation. The surface temperature of films in open air was measured using an infrared camera, under simulated solar light illumination at a power density of 1 kW•m^{-2} (1 sun) and 9 kW•m^{-2} (9 sun) (Figure 2.4C). After light irradiation for 120 seconds, the surface temperature for pristine HA-CS film increased from ~25 °C to ~28 °C at 1-sun irradiation and to ~32 °C at 9-sun irradiation, while the temperature increased to ~43 °C at 1-sun and to ~238 °C at 9-sun illumination for HA@PDA film (Figure 2.4D-E). In the presence of the HA-CS as a thermal insulator layer, the surface temperature of bilayered film increased to ~46 °C at 1-sun irradiation and ~245 °C at 9-sun irradiation. The higher surface temperatures for the bilayered structures, compared to the pure HA@PDA film in the open air, highlights the importance of integrating a thermal insulating layer into the photothermal membrane, which effectively mitigates the heat dissipation and enhances the localized heating at the surface.

The PMD performance of HA@PDA/HA-CS bilayered film was evaluated in a specially designed direct contact membrane distillation (DCMD) module (Figure S1.6), with a HA@PDA film with the same thickness as a control for comparison (Figure 2.5A). The PMD setup was maintained to be same as our reported test condition.[53] Simulated seawater, 0.5 M NaCl solution at ambient temperature (20 °C), was used as the feed water. Because the feed water flow rate can affect the water collection as we showed in our previous work,[53] the flow rate was fixed at 3.6 ml•min^{-1},

based on our previous work. The distillate at room temperature with a flow rate of 16.2 ml•min^{-1} was circulated on the opposite side of the membrane, and the generated freshwater was quantified by measuring the weight increase of the distillate as a function of irradiation time (Figure 2.5C) (all tests were conducted for 60 minutes). The water flux for HA@PDA film was 0.65 kg•m^{-2}•h^{-1} and 6.16 kg•m^{-2}•h^{-1} under 1-sun and 9-sun illumination, respectively. On the other hand, for the HA@PDA/HA-CS bilayered film, the water flux was found to be 0.89 kg•m^{-2}•h^{-1} and 8.28 kg•m^{-2}•h^{-1} under 1-sun and 9-sun irradiation, respectively. These results indicated that the presence of a thermal insulation layer led to ~27% and ~34% higher water flux compared to the HA@PDA film under 1-sun and 9-sun illumination, respectively.

The thermal efficiency of HA@PDA film is 45% under 1-sun and is 46% under 9-sun irradiation. This efficiency is much higher than the previously reported efficiency achieved by carbon black nanoparticles-coated PVDF membrane (~22%). The superior performance is closely related with the high loading of PDA and hierarchical porous network of the membrane. The large surface area and facile surface modification of HA nanowires allow dense and stable coating of PDA, resulting in high thermal energy output from HA@PDA nanowires under light irradiation. Furthermore, the nanowires with high aspect ratio intertwine with each other and form the interconnected porous structure, which results in a low resistance for vapor transport. As for the carbon black nanoparticles-loaded PVDF membrane, polymeric binder is added to prevent the desorption and leaching of the light-absorbing nanoparticles from the porous matrix, which inevitably narrows the pores and reduce the mass transport.[24, 76]

Under identical test conditions, we also evaluated the performance of HA@PDA/HA-CS bilayered film. The efficiency reached 62% and 63% under 1-sun and 9-sun irradiation, respectively, which is much higher than the HA@PDA film and previously reported PDA-coated PVDF membrane (~45%).[53] This bilayered membrane represents the highest efficiency for PMD among those

reported so far, treating the saline water at room temperature without auxiliary heating or heat recovery system.[24, 53] The improvement is mainly attributed to the enhanced localized heating at the evaporative surface owing to the presence of the HA-CS thermal insulation layer. Membranes with a high thermal efficiency have a relatively high resistance to conductive heat transfer as well as low resistance to mass transfer.[77] The low thermal conductivity of HA-CS layer in the hybrid film significantly reduces the conductive heat dissipation across the membrane and remarkably impairs the temperature polarization, yielding much stronger driving force for vapor transport.

During PMD, the thermal energy generated by the PDA leads to surface heating, so that the temperature of membrane surface (T_1) is larger than that of feed water (T_f). The generated vapor on the hot surface transfers to the cold distillate side due to the temperature difference between two sides of the membrane ($T_1 > T_2$). However, the conductive heat transfer across the membrane results in the temperature increase on the permeate side of membrane (Figure 2.5B). The smaller temperature difference across the membrane eventually lowers driving force for the vapor transfer. In the presence of HA-CS layer as a thermal insulator, the conductive heat from the hot surface (T_3) to the permeate side (T_4) of membrane can be greatly reduced (Figure 2.5B). Hence, more thermal energy is preserved on the surface for localized heating, and thus a larger temperature difference across the membrane is achieved with the bilayered film, ultimately resulting in higher solar efficiency for PMD.

To evaluate the long-term PMD performance, the HA@PDA film and bilayered film were tested over 5 cycles (each cycle for 1 hour). The average fluxes of the HA@PDA film were 0.63 $kg \cdot m^{-2} \cdot h^{-1}$ and 5.83 $kg \cdot m^{-2} \cdot h^{-1}$, and those of HA@PDA/HA-CS film were 0.89 $kg \cdot m^{-2} \cdot h^{-1}$ and 8.13 $kg \cdot m^{-2} \cdot h^{-1}$, under 1-sun and 9-sun illumination, respectively (Figure 2.5D). The average thermal efficiencies of HA@PDA film were 43% and 44%, and those of bilayered film were 61% and 62%, under 1-sun and 9-sun illumination, respectively (Figure 2.5E). The performance using both films

remained constant during the 5 cycles, and the variations in flux and thermal efficiency were less than 5%. As mentioned above, the anti-wetting property of membranes is critical for membrane distillation process. Therefore, the durability of hydrophobic modification of the membrane has also been investigated. The contact angle of HA@PDA film before PMD test was 129° and it was 125° for the bilayered film after 5-cycles testing (Figure S1.7). The negligible change (variation less than 5%) in the contact angle of the films indicates the durability of hydrophobic modification over repeated use of the membranes. Based on the Cantor–Laplace equation,[65, 78] the calculated liquid entry pressure for HA@PDA film and bilayered film is 110 kPa and 100 kPa, respectively. We then evaluated the mechanical stability of the film. Even after the vigorous mechanical agitation for 2 weeks, the bilayered film did not display any signs of disintegration (Figure S1.8A), and no change in morphology and hydrophobicity was observed (Figure S1.8B, S1.8C), highlighting the potential for long-term PMD application. This excellent durability of the membrane is ascribed to the outstanding mechanical properties (*e.g.*, high flexibility) of HA nanowires and the intertwined morphology of the network, which serves as mechanical interlocks. In fact, numerous reports in the past demonstrated that the strong interfacial interactions (*e.g.*, hydrogen bonding and electrostatic interactions) of HA nanowires with materials possessing polar functional groups (*e.g.* glass fiber, cellulose fiber, and CS) provides excellent mechanical strength of HA nanowires-based films, which can be used as printing papers,[57] separators for lithium battery,[59] bone-fracture fixation materials,[58] and fire-alarm wallpapers.[56] Considering the excellent mechanical stability, low thermal conductivity, interconnected porous network, facile surface modification, scalable synthesis and environmentally-benign nature, HA nanowire-based membranes are highly comparable to, if not better than, conventional materials for membrane distillation, such as PVDF, PTFE and PP.

2.5 Conclusions

Here, we have successfully designed and fabricated a biocompatible HA@PDA/HA-CS bilayered film membrane for highly efficient PMD. The photothermal efficiency of the PDA/HA nanowires film reached 62% under 1-sun illumination and represents the highest efficiency for PMD reported so far for treating saline water at room temperature without any auxiliary heating system or heat recovery system. The facile surface modification and large surface area make HA nanowires an outstanding template for forming a dense, stable, and efficient PDA coating, which in turn ensures broadband light absorption and high light-to-heat conversion. More importantly, the interconnected porous structure, formed by the highly flexible and intertwined nanowires, leads to low resistance to vapor transfer. Simultaneously, the low thermal conductivity of HA nanowires layer significantly reduces the conductive heat transfer from the evaporative surface to the cold permeate side. This further improved the localized heating and vapor transfer across the membrane. In the presence of HA nanowires layer as a thermal insulator, the water flux of bilayered film is ~27% (under 1 sun) and ~34% (under 9 sun) higher than those of the HA@PDA film under identical test condition, respectively. Furthermore, the excellent mechanical robustness of bilayered film contributes to long-term and stable PMD performance, showing great potential for real-world application. This environmentally-benign, highly efficient and mechanically stable HA nanowires-based photothermal membrane is highly promising for freshwater generation in the remote regions and disaster-struck communities by utilizing the abundantly available sunlight and saline water.

2.6 Supporting information

Supporting Information for chapter 2 is provided in appendix 1.

2.7 Figures

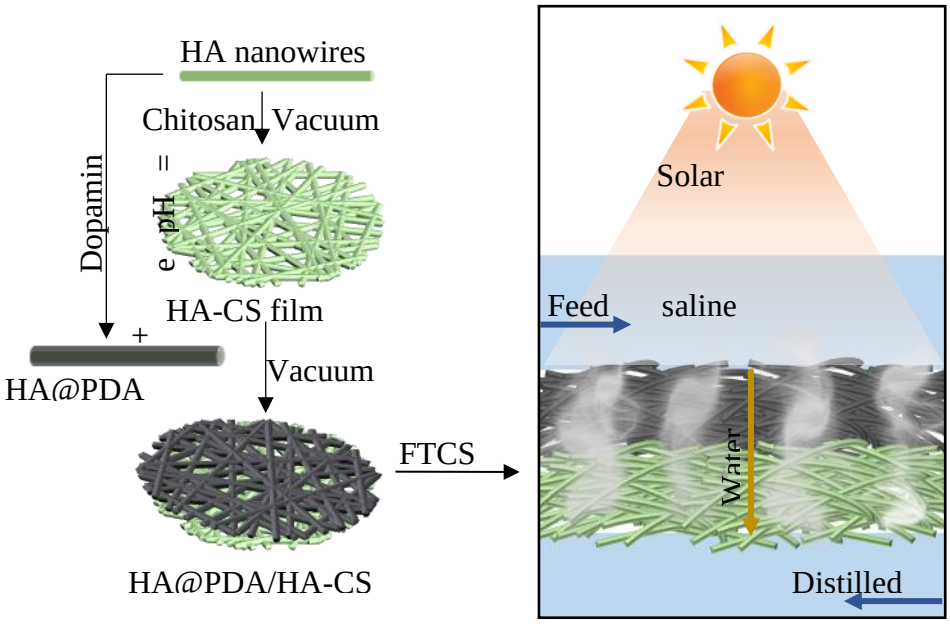

Figure 2.1. Schematic illustration depicting the fabrication of HA@PDA/HA-CS bilayered photothermal film and PMD based on this bilayered structure. Chitosan (CS) is added to the HA nanowires suspension and subsequently the mixture is vacuum filtered to prepare the HA-CS film. HA nanowires are dispersed in the dopamine solution (pH = 8.5) to allow the PDA coating on the HA surface and the obtained HA@PDA nanowires were vacuum filtered onto the HA-CS film to prepare the bilayer photothermal film. Finally, to obtain hydrophobic surface, the film was fluorosilanized using (tridecafluoro-1,1,2,2-tetrahydrooctyl)-trichlorosilane (FTCS). PMD was conducted using a direct contact membrane distillation cell under simulated solar irradiation.

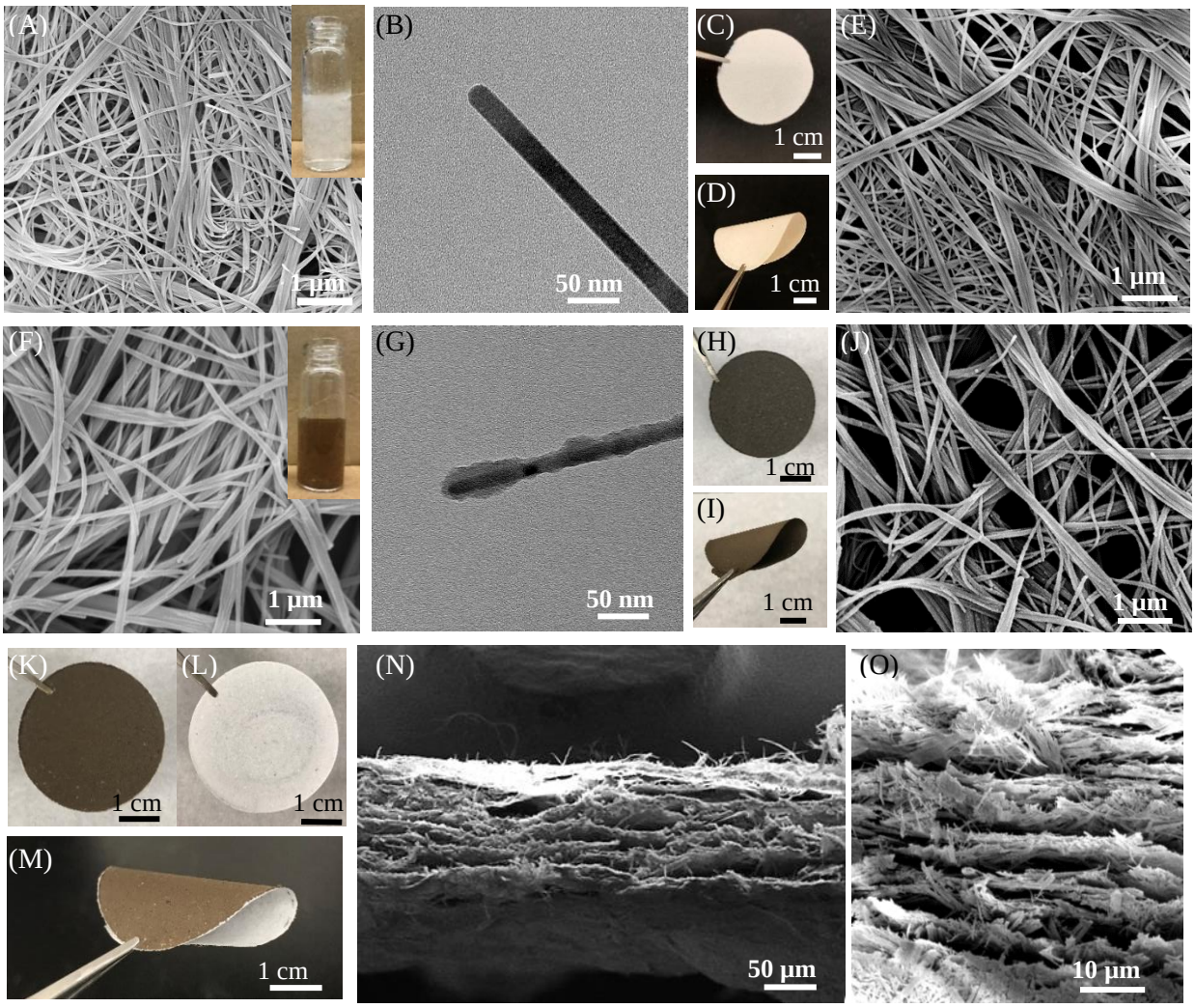

Figure 2.2. (A) SEM image of HA nanowires (inset shows the photograph of HA nanowires suspension). (B) TEM image of HA nanowires. Photograph of a flat (C) and deformed (D) HA-CS film. (E) SEM image of the HA-CS film. (F) SEM image of HA@PDA nanowires (inset shows the photograph of HA@PDA nanowire suspension). (G) TEM image of HA@PDA nanowires. Photograph of a flat (H) and deformed (I) HA@PDA film. (J) SEM image of the HA@PDA film. Photograph of top (K), bottom (L) of HA@PDA/HA-CS film and a deformed bilayered film (M). The cross-section SEM images of the HA@PDA/HA-CS film in low magnification (N) and high magnification (O).

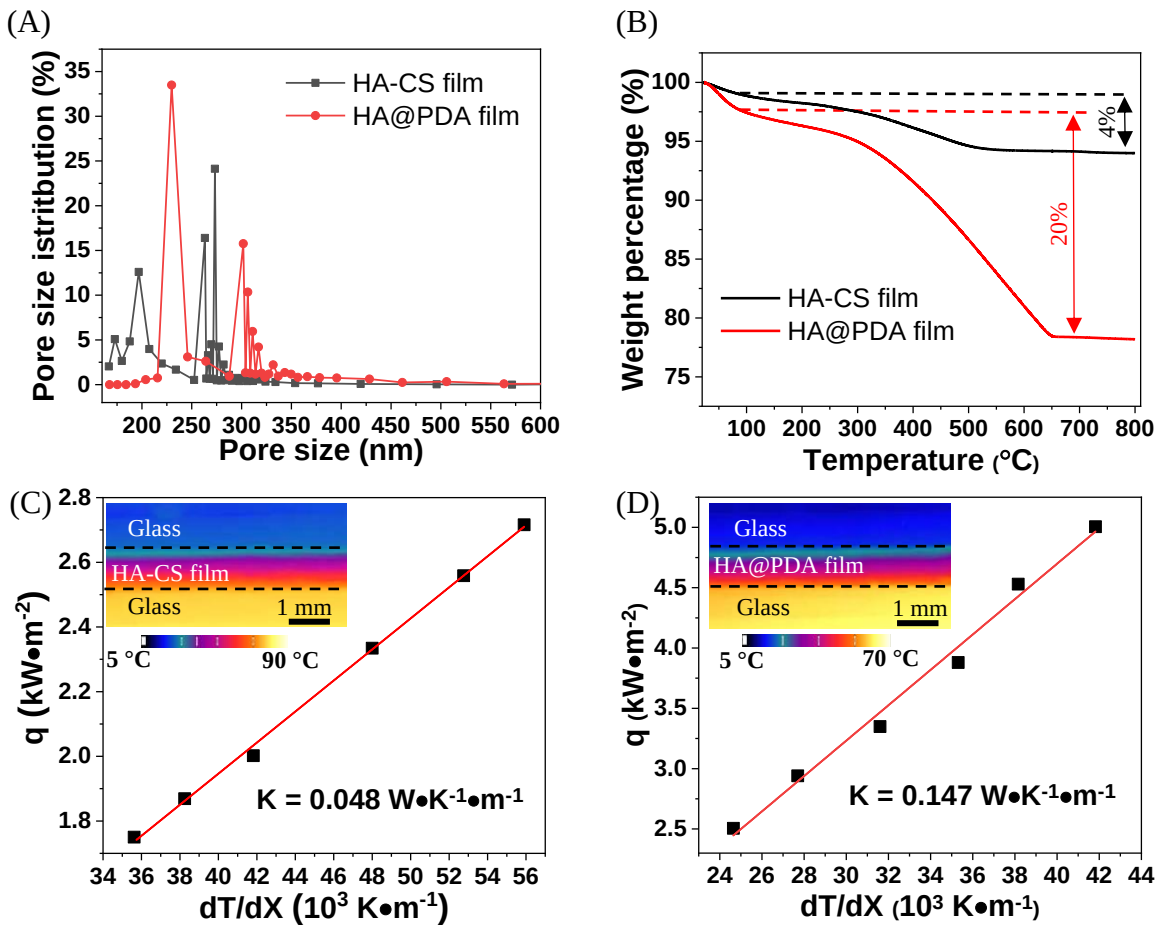

Figure 2.3. Characterization of HA-CS film and HA@PDA film. Pore size distributions (A) and TGA analyses (B) of representative HA-CS film and HA@PDA film. Thermal conductivity of HA-CS film (C) and HA@PDA film (D). Insets: representative IR images showing the temperature gradient along the thickness of the HA-CS film (C) and HA@PDA film (D).

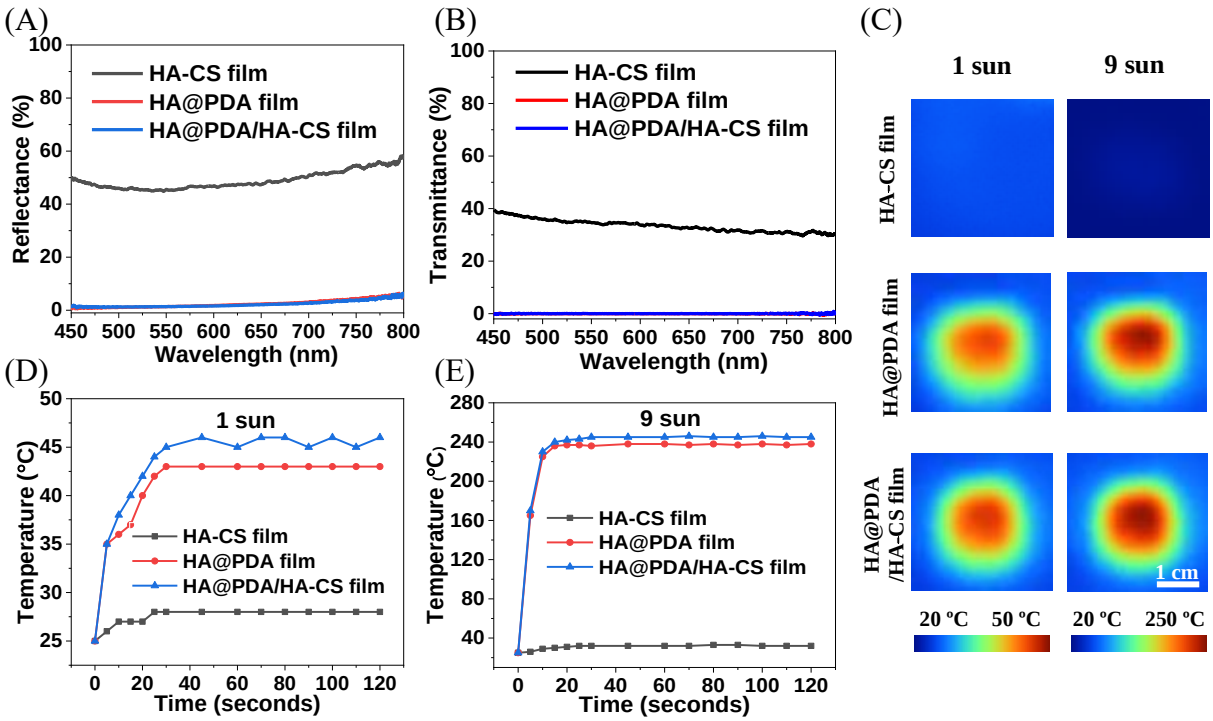

Figure 2.4. Optical and photothermal properties of the membranes. Reflectance (A) and transmittance spectra (B) of the HA-CS film, HA@PDA film, and HA@PDA/HA-CS film. (C) IR images showing the surface temperature of the HA-CS film, HA@PDA film and HA@PDA/HA-CS film under 1-sun and 9-sun illumination in open air after 120 seconds. The plots showing the surface temperature of the HA-CS film, HA@PDA film and HA@PDA/HA-CS film under 1-sun (D) and 9-sun illumination (E) as a function of irradiation time.

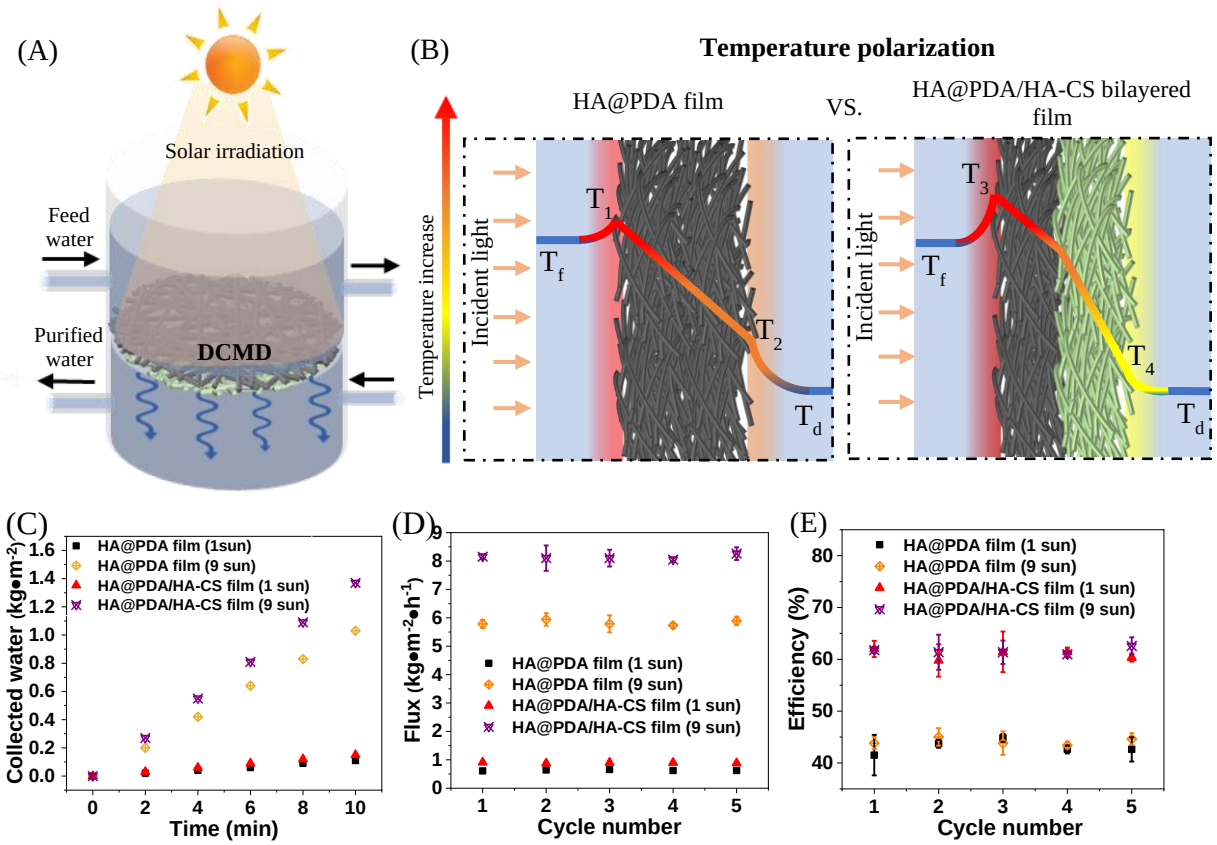

Figure 2.5. PMD performance for the HA@PDA film and HA@PDA/HA-CS film. (A) Schematic illustration of photothermal direct contact membrane distillation (DCMD) using HA@PDA/HA-CS film with thickness of the feed water at 8 mm. (B) Schematic illustration of thermal profile of DCMD using a HA@PDA film (left) and HA@PDA/HA-CS film (right) under solar irradiation. (C) PMD performance of HA@PDA film and HA@PDA/HA-CS film in purifying 0.5 M NaCl saline water under 1-sun and 9-sun illumination. Flux (D) and thermal efficiency (E) of the photothermal DCMD system using the HA@PDA film and HA@PDA/HA-CS film, with 0.5 M NaCl saline water under 1-sun and 9-sun irradiation for 5-cycles testing (each cycle for 1 hour, standard deviation obtained from measurements of 3 samples).

Chapter 3: Investigation of the Photodegradation of Polydopamine under Reactive Oxygen Species Using Plasmonic Transducer

3.1 Abstract

PDA has been widely used as photothermal materials in solar-driven desalination, owing to its excellent photothermal property, easy synthesis and biocompatibility. Reactive oxygen species

(ROS) lead to the degradation of PDA, resulting in compromised photothermal performance. However, the dissolution of PDA in ROS has not been well understood. Here, we utilize the gold-nanorods (AuNRs) as plasmonic nanostransducer to probe the photodegradation of PDA in the ROS. Monitoring the localized surface plasmon resonance (LSPR) shift of PDA-coated AuNRs, the growing and dissolution of PDA in ROS is recorded. The atomic force microscope (AFM) results validate the reliability of probing photodegradation process by LSPR. Owing to the high sensitivity of LSPR wavelength to localized changes in dielectric medium around the AuNRs, small thickness change in the PDA layer can be monitored quickly with smaller stand deviation, offering fast and *in-situ* detection of PDA degradation. Furthermore, the effect of different ROS on the PDA dissolution is also successfully monitored using this plasmonic nanostransducer. This plasmonic nanotransducer probes real-time chemical transformation of PDA during its dissolution and the photodegradation of PDA under different ROS condition, which will be highly important in predicting the fate and transformation of PMD during their solar-driven desalination in aqueous systems.

3.2 Introduction

Inspired by the adhesive protein in mussels, PDA with a structure similar to eumelanin is well-known for its versatile adhesion on almost all substrates *via* self-polymerization of dopamine in alkaline solution.[53, 67] With similar structure to eumelanin, PDA also possesses excellent photothermal property. It can absorb 99% incident photon energy over a broad solar spectrum and rapidly convert it into heat within tens of picoseconds, thus offering protection to living organisms against ultraviolet injury.[79] Compared to most other photothermal materials discussed, the biocompatibility, low toxicity and biodegradable nature of PDA make it an environmentally-benign material, and its versatile adhesion enables it to be potentially deployed on large scales in aqueous environments with minimal effect on the ecosystem.[39, 67] Because of excellent

photothermal property and biocompatibility, PDA has been utilized as photothermal agents in membrane for highly efficient PMD. PDA-coated PVDF membrane after FTCS treatment achieved high thermal efficiency of 45% in PMD. As an alternative to depositing a PDA layer on the substrate, PDA microspheres were synthesized and integrated with bacterial naocellulose (BNC) aerogel. The PDA/BNC bilayer structure after FTCS treatment achieved thermal efficiency of 68% in PMD.[80]

Although photothermal membranes incorporated with PDA have been widely used in solar-driven desalination, their reaction with reactive oxygen species (ROS) is a concern for the long-term stable photothermal performance. Through the photochemical reactions, biological processes, and atmospheric deposition in the natural water system,[81] various ROS are generated.[45] For example, the presence of hydrogen peroxide (H_2O_2) was detected in tens to hundreds of nanomolar concentrations in surface sea waters.[81] Under solar illumination, the photolysis of H_2O_2 results in the formation of hydroxyl radical (•OH), and other ROS generates following the propagation of photochemical reaction.[82, 83] The presence of ROS may result in the degradation of photothermal materials. Yang and co-workers demonstrated the reduced UV-vis-NIR absorbance of PDA nanoparticles in the presence of hydrogen peroxide.[84] The deteriorated light absorption accompanied with color fading rises from the degradation in the ROS. Tseng and co-workers also reported the hydroxyl radicals-induced degradation of PDA nanoparticles, resulting in the formation of 5,6-dihydroxyindole.[85] However, the dissolution kinetics of PDA in ROS is not well understood, and effect of different ROS on the dissolution of PDA is still unknown. To predict the fate and transformation of photothermal materials during their PMD performance in aqueous systems, the chemical stability of photothermal materials under ROS should be fully investigated. Recently, plasmonic nanoparticles have attracted extensive attention for chemical sensing.[86] The time-varying electric field of the electromagnetic radiation causes collective oscillation of

conduction electrons in metal nanoparticles with a resonance frequency, termed localized surface plasmon resonance (LSPR).[87-89] The LSPR wavelength of metal nanostructures is sensitive to numerous factors, including composition, size, and shape of the nanostructures dielectric medium surrounding the nanostructures and proximity to other nanostructures.[90] The extremely high sensitivity of LSPR wavelength to localized changes in dielectric medium around the nanostructures renders it an attractive nanotransducer for chemical and biological sensing.[91] LSPR has been employed to probe the conformational changes of individual biomacromolecules, detecting single biomolecule binding events, monitoring the kinetics of catalytic activity of single nanoparticles and even optically detecting single electrons.[92-95] Gold nanorods (AuNRs) are particularly attractive as plasmonic transducers owing to their facile and large tunability of the LSPR wavelength with aspect ratio and large refractive index sensitivity.[90, 96] AuNRs-based nanotransducer have employed to monitor the thickness change in the deposition and swelling behavior of an ultrathin polymer film.[97] Owing to these merits, AuNRs-based nanotransducer is a highly promising sensor to probe the photochemical reactions of PDA in ROS.

Herein, we report AuNRs as plasmonic transducers to monitor the degradation of PDA in ROS. The shift in the LSPR wavelength of AuNRs are monitored during the polymerization of dopamine or exposure in ROS environment to reveal the growing and degradation kinetics of PDA. AFM is also utilized to analyze the morphology and thickness change in the PDA layer on the AuNRs, validating the reliability of results obtained by LSPR. Furthermore, the degradation of PDA in different ROS environment is investigated and compared. Compared with conventional characterization using AFM or TEM, LSPR using plasmonic nanotransducer is a fast method and offers comprehensive understanding of photodegradation of PDA under ROS, which will be highly important in predicting the fate and transformation of photothermal materials during solar-driven desalination in aqueous systems.

3.3 Experimental Section

Synthesis of AuNRs

AuNRs were synthesized using a seed-mediated approach.[98] Seed solution was prepared by adding 1 ml of an ice-cold solution of 10 mM sodium borohydride into 10 ml of magnetically stirred 0.1 M cetyltrimethylammonium bromide (CTAB, Sigma Aldrich) and $2.5 \cdot 10^{-4}$ M $HAuCl_4$ (Sigma Aldrich) aqueous solution at room temperature. The color of the seed solution changed from yellow to brown. Growth solution was prepared by mixing 95 ml of 0.1 M CTAB, 0.8 ml of 10 mM silver nitrate (Sigma Aldrich), 5 ml of 10 mM $HAuCl_4$, and 0.55 ml of 0.1 M ascorbic acid (Sigma Aldrich) in the same order. The solution was homogenized by gentle stirring. To the resulting colorless solution, 0.12 ml of freshly prepared seed solution was added and set aside in the dark for 14 h. The solution turned from colorless to greenish brown, with most of the color change happening in the first hour. Prior to use, the AuNRs solution was centrifuged at 13 000 rpm for 10 min to remove excess CTAB and redispersed in nanopure water (18.2 M•cm). The centrifugation procedure was repeated twice.

Adsorption of AuNRs on glass surface

The piranha cleaned glass substrates were immersed in 1% (3-mercaptopropyl) triethoxysilane (MPTES) solution in ethanol for 1 h and then rinsed with ethanol. The glass substrates were exposed with AuNRs solution for 3 h to enable uniform absorption of AuNRs on glass substrates. Finally, the substrate was rinsed with water to remove the loosely bound AuNRs, leaving a stably absorbed AuNRs on the surface.

Fabrication of PDA coated AuNRs (AuNRs@PDA) substrates

The AuNRs coated glass substrates were immersed in 10mM tris-buffer solution (pH = 8.5, Sigma Aldrich) and followed by addition of dopamine power (1 mg/ml, Sigma Aldrich) under

continuously shaking condition. Then as-prepared AuNRs@PDA substrates were rinsed with water to remove the loosely bound PDA. Finally, the substrates were blow dried with N_2 gun.

Polyelectrolyte LbL assembly

The substrates adsorbed with AuNRs were immersed in 2% polystyrene sulfonate (PSS, Sigma Aldrich) in 0.1 M NaCl aqueous solution for 15 min followed by rinsing with nanopure water for 30 s and rinsing with 0.1 M NaCl solution for an additional 30 s on each side of the glass slides. Then the substrates were immersed in a solution of 2% polyallylamine hydrochloride (PAH, Sigma Aldrich) in 0.1 M NaCl for 15 min followed by the rinsing procedure described above. Subsequently, the substrates were dried under a stream of N_2 before acquiring extinction spectra with a UV−vis spectrometer. This procedure was repeated 10 times to deposit a total of 10 bilayers. The thickness of each polyelectrolyte bilayer was measured to be ∼2 nm.

Photodegradation of PDA

The AuNRs@PDA glass substrates were immersed in ROS solution under UV light irradiation. After certain time, the substrates were removed from the solution and wash with water. After dried with N_2 stream, the substrates were subject for UV measurement or AFM measurement.

Instrumentation

TEM was recorded on a JEOL JEM-2100F field emission instrument. The sample was prepared by drying a drop of the solution on a carbon-coated grid, which had been previously made hydrophilic by glow discharge. UV–vis extinction spectra were collected in air and water using a Shimadzu UV-1800 UV–vis spectrometer. AFM micrographs were obtained using Bruker Dimension Icon AFM in scanasyst mode. The ultraviolet A (UVA, Black ray B-100A) were used as the light source.

3.4 Results and Discussion

We have synthesized AuNRs with diameters of 16 nm and length of 57 nm, using seed-mediated approach (Figure 3.2A). AuNR were adsorbed on a (3-mercaptopropyl) triethoxysilane (MPTES)-coated glass slide by exposing the glass slide to AuNRs solution, followed by extensive rinsing with water to remove weakly adsorbed AuNRs. The thiol (–SH) groups in MPTMS are known to possess high affinity to gold *via* Au-S covalent bonding, resulting in the strong absorption of AuNRs on MPTES modified glass substrates. AFM images revealed the uniform distribution of AuNRs on the glass substrates with no signs of aggregation or patchiness (Figure S2.2A).

The UV−vis extinction spectra of AuNRs are characterized by two distinct bands corresponding to the transverse and longitudinal oscillation of the conduction electrons with incident electromagnetic (EM) field.[97] Owing to the higher refractive index sensitivity compared to transverse band, the longitudinal band is routinely employed in chemical sensing. To correlate LSPR wavelength shift with the thickness of PDA on AuNRs, the refractive index sensitivity and EM decay length of AuNRs are measured by layer-by-layer (LbL) assembly of polyelectrolyte multilayers (PEM).[99] LbL assembly involves the alternate adsorption of oppositely charged polyelectrolytes, offering fined tunability of the thickness of the PEM down to ∼1 nm.[100] The negatively charged poly(styrene sulfonate) (PSS) and positively charged poly(allyl amine hydrochloride) (PAH) were alternatively absorbed on the AuNRs substrates, leading to a linear increase of PEM film thickness with the number of bilayers.[101] The extinction spectra reveal a progressive increase in the extinction intensity and red shift in the LSPR wavelength with the deposition of each bilayer due to the increase in the refractive index of the medium around the AuNRs (from air to polymer (Figure 3.2B)). The extinction spectrum was deconvoluted by fitting the band with two Gaussian peaks, from which the LSPR wavelength was obtained (Figure S2.1). Owing to the evanescent nature of the EM field at the surface of the plasmonic nanostructures, the

LSPR wavelength shift exhibits a characteristic decay with the increasing distance from the surface of AuNRs (Figure 3.2C), given by[102]

$$R = m\Delta\eta \left(1 - exp\left(-\frac{2d}{l}\right)\right) \quad (2)$$

where R is LSPR shift, m is the refractive index sensitivity of AuNRs, $\Delta\eta$ is the change in the refractive index in refractive index unit (RIU), d is the adsorbate layer thickness (thickness of the PEM in this case), and l is the EM decay length. Assuming the refractive index of the PEM to be 1.56 RIU, the Δη measured in air is 0.56 RIU. Based on equation (2), the refractive index sensitivity (m) and EM decay length (l) of AuNRs are calculated to be 17 nm and 210 nm/RIU, respectively (Figure 3.2C). The thickness of PEM on AuNRs substrates after 10 bilayers deposition was revealed to be ~20 nm (Figure 3.2D), which closely agrees with the value reported previously for the PAH/PSS system.

A thin layer of PDA coating was self-polymerized on AuNRs by exposing the AuNRs substrate to dopamine solution in Tris–HCl buffer solution (pH 8.5) (Figure 3.3A). Here, AuNRs serve as highly sensitive transducers to monitor the changes in the refractive index of the surrounding medium. We employed the refractive index sensitivity and EM decay length of longitudinal AuNRs to probe the thickness of PDA grown on AuNRs surface. The longitudinal LSPR wavelength of the AuNRs exhibited a progressive red shift following the self-polymerization of DA on AuNRs (Figure 3.3B), indicating an increase in the refractive index of medium around the AuNRs. To probe the growing of PDA on AuNRs, the LSPR shift following the polymerization of DA was fitted with equation (2) (Figure 3.3C). The calculated thickness of PDA on AuNRs after polymerizing for 30, 60, 90 and 120 minutes, was 2.9, 6.4, 9.4, and 12.1 nm, respectively. Hence, the thickness of PDA grown on AuNRs with different polymerization time was obtained (Figure 3.3D).

To confirm the thickness of PDA thin layer on AuNRs independently, AFM imaging was performed along the edge of an intentional scratch in AuNRs@PDA layer (Figure S2.2B-E). With increasing time, the surface of AuNRs were rougher and the height of AuNRs also increased, indicating the successful coating of PDA on AuNRs. Averaged cross-sectional height profiles (3 samples, and 50 AuNRs@PDA for each sample) across the scratch reveal the thickness of the AuNRs@PDA. After analyzing the height profile of AFM images with different polymerization time, the height of AuNRs@PDA was obtained (Figure S2.2F). The diameter of pure AuNRs was measured to 16 nm. The height of AuNRs@PDA with polymerization of 30, 60, 90 and 120 minutes, was 21, 24, 26, and 27 nm, respectively. After subtracting the height of AuNRs@PDA from the height of pure AuNRs, we obtained the thickness of PDA. The calculated thickness of PDA with polymerization time of 30, 60, 90 and 120 minutes was 5, 8, 10 and 12 nm. The results measured from AFM are close to the value estimated using the LSPR (Figure S2.2H). Thus, the independent AFM measurements unambiguously and quantitatively confirm the results obtained from the plasmonic nanotransducers and establish the validity of this novel approach.

To study the photodegradation of PDA, AuNRs@PDA was exposed to H_2O_2 solution (0.12 %) under UV irradiation (365 nm) at room temperature for 10 hours. AFM images of AuNRs@PDA after subjecting to ROS for 2, 4, 6, 8 and 10 hours were obtained, showing a progressive decrease in the height and roughness of the AuNRs@PDA (Figure S2.3A-F). The morphology of AuNRs@PDA was found to be essentially identical to the pristine AuNRs (Figure S2.2A) after subjecting them to H_2O_2 and UV irradiation for 10 hours (Figure S2.3F), which reveals the near complete decomposition of PDA on AuNRs. It is worth noting that the size and shape of the nanotransducers are not affected by ROS, which is critical for their successful application in harsh environmental settings.

The photochemical reactions causing the slow degradation and dissolution of the PDA layer results in a change in the refractive index around the AuNRs that can be monitored by continuously measuring the LSPR wavelength of the AuNRs. The AuNRs exhibit a highly distant-dependent refractive index sensitivity. We noted a progressive blue shift in LSPR wavelength of AuNRs@PDA upon exposure to 0.12 % H_2O_2 under UV irradiation (Figure 3.4A). The refractive index sensitivity and EM decay length were also employed to estimate the change in the thickness of PDA undergoing photochemical reaction using the experimentally obtained LSPR shift (Figure 3.4B). We observed an exponential decrease in the thickness of PDA layer (Figure 3.4C). The degradation of PDA in the presence of ROS exhibited a terminal thickness of around 0.8 nm, which can be ascribed to thickness of surfactant layer (hexadecyltrimethylammonium bromide (CTAB)) on AuNRs. The thickness measured from LSPR is consistent with the AFM results (Figure 3.4D), indicating the reliability of probing photodegradation with AuNRs-based nanotransducers. Most importantly, AuNRs-based nanostransducers are readily to probe the photodegradation in nanoscale with smaller standard deviation, and thickness change of PDA after small time interval of reaction can be obtained. Furthermore, it is a fast method. As for AFM, 3 samples are collected for each condition, and 50 AuNRs or AuNRs@PDA are measured for each sample, which are more time consuming than results obtained by LSPR.

To gain further insights into the effect of different ROS on the degradation of PDA, we have exposed the AuNRs@PDA to different condition. Here, we have tested the effect of H_2O_2, •OH, •OOH and O_2^- on the decomposition of PDA. Firstly, the AuNRs@PDA substrates were exposed to 0.12% H_2O_2 solution with UV light irradiation and under dark condition, respectively. Under UV illumination, H_2O_2 will be decomposed, leading to the generation of •OH.[83] With propagation of this photochemical reaction, other ROS generates, such as •OOH and O_2^-. The generation of ROS will be much less in dark compared to the condition with UV light irradiation, resulting in

presence of more H_2O_2. Under 0.12% H_2O_2 solution with UV light irradiation, a PDA layer with thickness of 12.9 nm (100%) was completely decomposed, after 9 hours (Figure 3.5A). However, PDA layer with thickness of around 2.8 nm was degraded after 11 hours under 0.12% H_2O_2 solution without light, accounting for 22% PDA degradation and indicating that H_2O_2 plays small impact on the photodegradation of PDA (Figure 3.5A). Then, we investigated the effect O_2^- on the photochemical reaction of PDA. In 0.12% H_2O_2 solution under UV illumination, the addition of superoxide ion scavenger, superoxide dismutase (SOD), can remove the O_2^-. We found that the thickness of PDA layer reduced by 10.8 nm during the absence of O_2^-, corresponding to 88% PDA decomposition, almost similar with the condition when there are no SOD and indicating that O_2^- affects less on the photodegradation of PDA (Figure 3.5B). Finally, we tested the photodegradation of PDA after addition of both SOD and hydroxyl radical scavenger, tert-butanol (TBA). The PDA thickness was reduced to 4.1 nm and 67% PDA was degraded in the environment that does not contain hydroxyl radicals (Figure 3.5C), revealing that •OH plays a significant role on the photodegradation of PDA.

3.5 Conclusions

In summary, we have demonstrated the novel approach of detecting the photodegradation of PDA using AuNRs-based nanotransducer. This method is fast and offers nanoscale tracking of photodegradation of PDA. The results obtained by AuNRs agreed well with these obtained from AFM, indicating the reliability of this novel approach. By probing the LSPR shift of AuNRs@PDA, we demonstrate that PDA are decomposed under ROS environment. Furthermore, we investigate the effect of different ROS on the photodegradation of PDA using the AuNRs-based nanotransducer. With different ROS scavengers, we found that •OH play a significant role on the photodegradation of PDA, whereas H_2O_2 and O_2^- has less effect on the PDA decomposition.

3.6 Supporting information

Supporting Information for chapter 2 is provided in appendix 2.

3.7 Figures

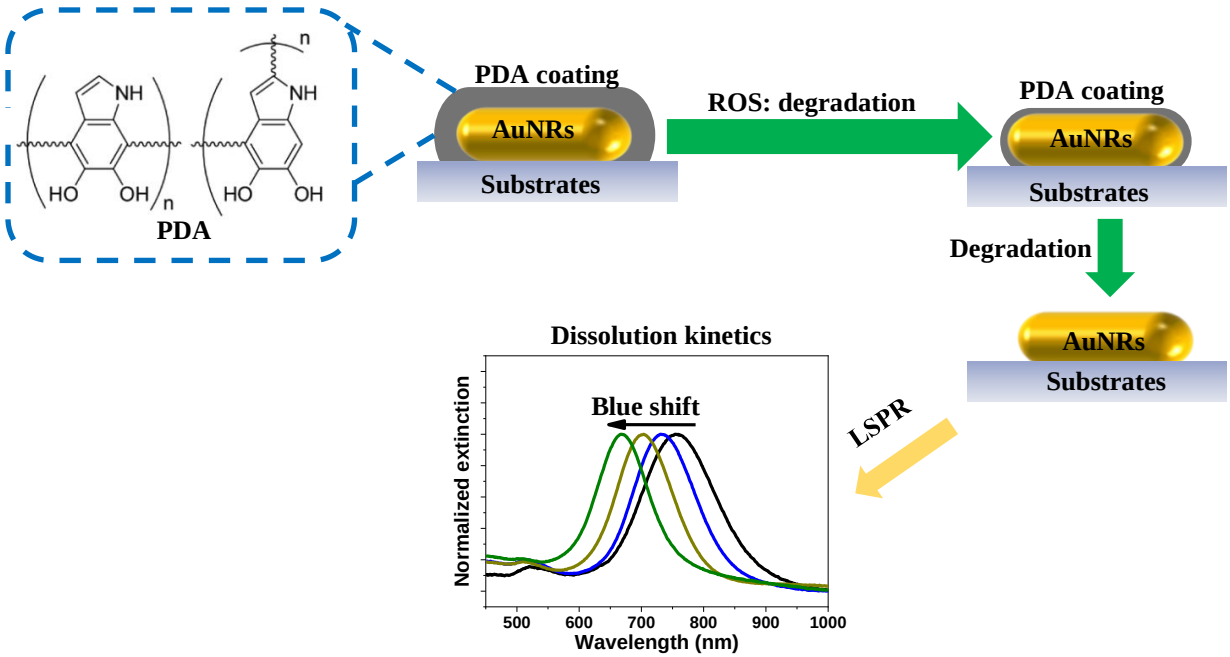

Figure 3.1. Schematic illustration of using AuNRs-based plasmonic nanostransducer to monitor the degradation of PDA in ROS environment.

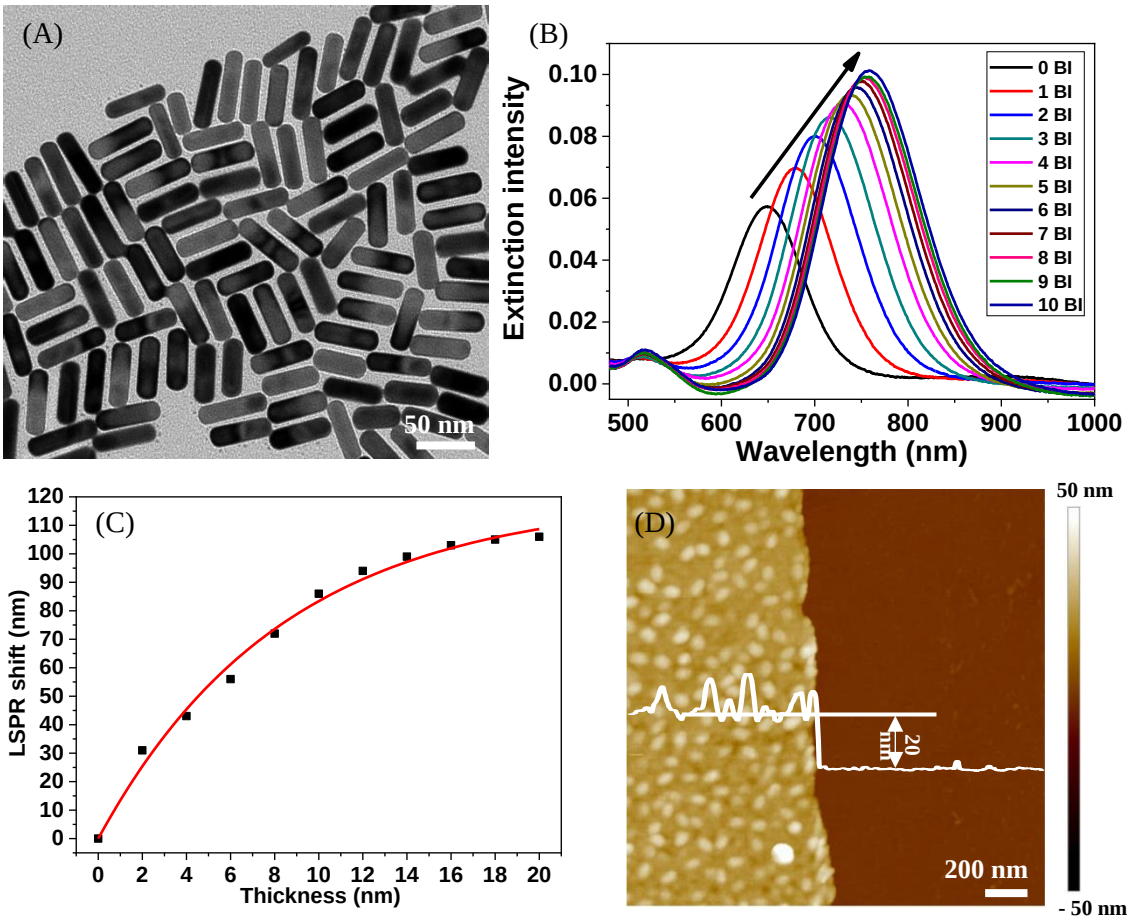

Figure 3.2. (A) TEM images of AuNRs. (B) UV-vis extinction of AuNRs following the deposition of each bi-layer polyelectrolyte showing a progressive red-shift and increase in the intensity of longitudinal plasmon band. (C) Plot of cumulative shift of longitudinal plasmon resonance wavelength with the deposition of polyelectrolyte on AuNRs. (D) AFM image along the edge of an intentional scratch in PEM film comprised of 10 bilayers deposited on AuNRs.

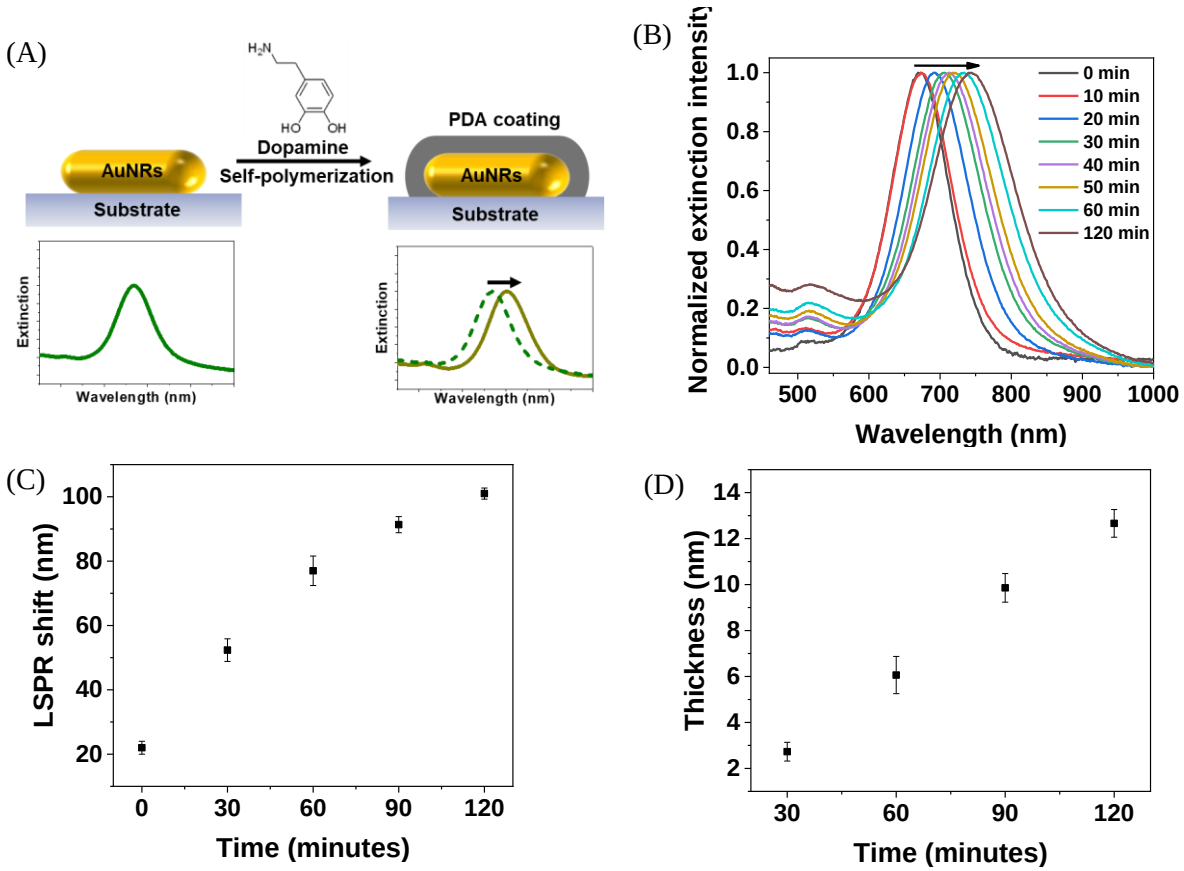

Figure 3.3. (A) Schematic illustration of probing polymerization of DA using LSPR. (B) UV-vis extinction of AuNRs following polymerization of DA showing a progressive red shift. (C) Plot of cumulative shift of longitudinal plasmon resonance wavelength with the polymerization of DA on AuNRs. (D) Plot of cumulative thickness of PDA on AuNRs with different polymerization time, obtained from LSPR shift.

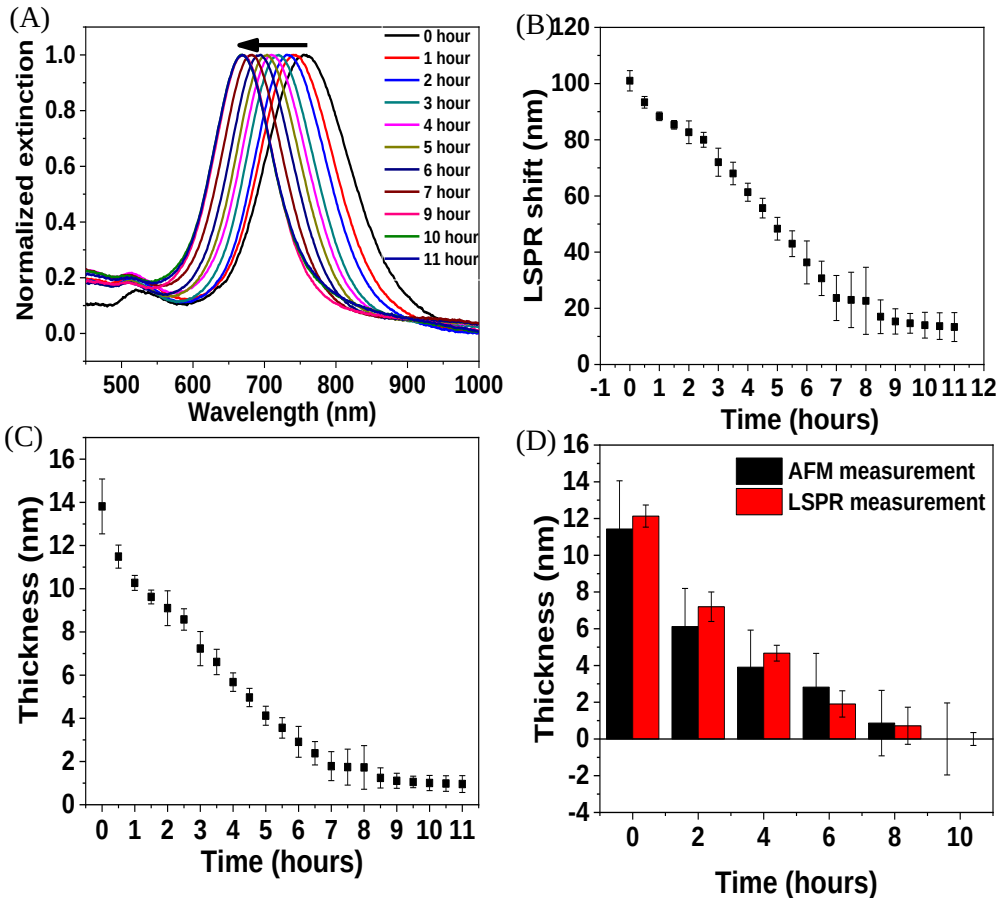

Figure 3.4. (A) UV-vis extinction of AuNRs@PDA following H_2O_2 and UV light showing a progressive blue shift. Plot of cumulative (B) LSPR shift and (C) thickness of PDA on AuNRs after exposure to 0.12% H_2O_2 and UV light. (D) The thickness of PDA on AuNRs after exposure to 0.12% H_2O_2 and UV light measured by AFM and LSPR.

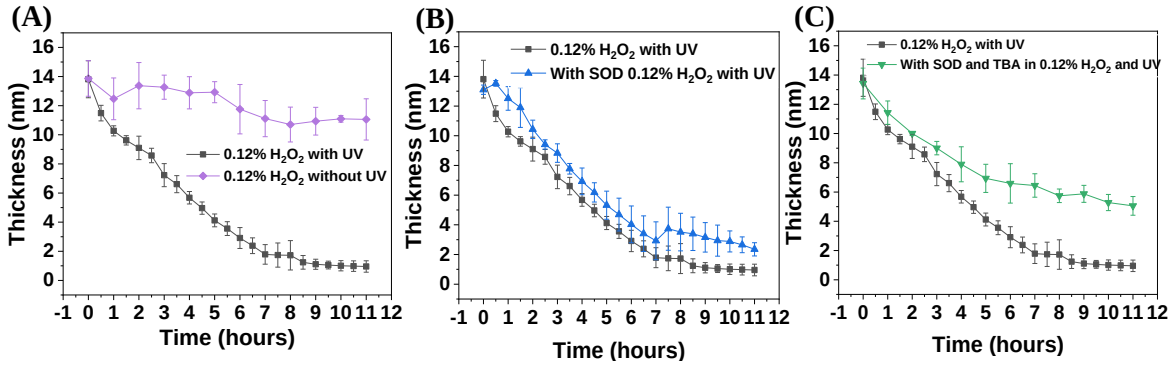

Figure 3.5. (A) The thickness of PDA on AuNRs after exposure to 0.12% H_2O_2 under UV light and dark condition. (B) The thickness of PDA on AuNRs after exposure to 0.12% H_2O_2 under UV light with and without SOD. (C) The thickness of PDA on AuNRs after exposure to 0.12% H_2O_2 with and without SOD and TBA.

Chapter 4: MXene Aerogel for Efficient Photothermal Driven Membrane Distillation with Dual-Mode Antimicrobial Capability

4.1 Abstract

Solar-driven desalination, which involves the conversion of solar energy to heat for freshwater generation, has been recognized as an attractive and sustainable desalination technology to alleviate freshwater shortage. In particular, photothermal driven membrane distillation (PMD) is a highly promising solar-driven desalination technology, especially in remote regions and disaster-struck communities, where no power infrastructure or waste heat from industrial plants is available. MXene, more specifically $Ti_3C_2T_x$, with excellent photothermal properties, easy processability, and electrical conductivity offers a great opportunity for realizing highly efficient, stable and multifunctional PMD membranes. Herein, we realize a MXene composite aerogel comprised of hydroxyapatite nanowires and poly(vinyl alcohol) with high thermal efficiency (61%) and water flux (0.72 $kg•m^{-2}•h^{-1}$) under 0.8 sun irradiation (0.8 $kW•m^{-2}$), representing the first validation of highly efficient MXene-based PMD systems in treating ambient saline water. Owing to the strong interfacial interaction (*i.e.*, hydrogen bonding) between the building blocks, the MXene composite aerogel with high porosity (up to 91%) exhibited excellent mechanical stability. This highly interconnected porous network offers low resistance to vapor transport and low thermal conductivity, which minimizes conductive heat transfer across the aerogel, thus maximizing the thermal efficiency. Furthermore, the outstanding bactericidal activity induced by solar irradiation or electric potential makes the MXene composite aerogel a highly attractive candidate for PMD in the real world.

4.2 Introduction

To overcome the limited freshwater availability, increasing water demand and pollution caused by human activity, various desalination technologies have been developed to relieve the water scarcity, including reverse osmosis and thermal distillation.[10, 54] However, they still have challenges to address freshwater shortage because of high energy consumption and high carbon footprint, especially for developing countries or rural areas where large power plants are not available.[103] To minimize the non-renewable energy consumption and reduce the possible adversary impacts on the environment during freshwater generation, emerging technologies, such as solar steam generation, are highly promising.[1, 104, 105] For solar stream generation, the advances in materials and the design of interfacial evaporators have prompted the thermal efficiency up to 90%, but the difficulty associated with freshwater collection from the generated vapor has still hindered their application in the real world.[106] For instance, the reported thermal efficiency decreases by 60–70% after integrating a solar steam generator with water collection system.[107, 108] To address this challenge, another solar-driven desalination technology, photothermally-driven membrane distillation (PMD), has been proposed, which integrates membrane distillation with photothermal membrane.[19, 21, 67, 109] Upon solar irradiation, the surface heating is achieved on the photothermal membrane, and the vapor is generated at the interface between the feed water and the hydrophobic photothermal membrane. Driven by the vapor pressure caused by the temperature difference across the photothermal membrane, the vapor transports from the hot feed side to the cold permeate side of the photothermal membrane, where the vapor condenses for freshwater generation.

As a new series of 2D materials, the MXene family is composed of early transition metal carbides and/or carbonitrides, with a general formula of $M_{n+1}X_n$, where M represents transition metal (*e. g.*, Sc, Ti, Zr, Hf, V, Nb, Ta, Cr and Mo) and X is carbon and/or nitrogen.[110] Synthesized by wet-

chemical etching using hydrofluoric (HF) acid or HF-containing or HF-forming etchants, the functional groups (*e.g.,* -OH, -O and -F) are introduced on the surface of MXene,[111] and as-synthesized MXene is represented by $M_n+1X_nT_x$, where T_x refers terminal functional groups.[112] Recently, MXene has been utilized in solar-driven desalination.[113] MXene exhibits broadband light absorption and an outstanding (100%) internal light-to-heat conversion efficiency, enabling excellent photothermal performance.[114] For instance, a MXene aerogel exhibited up to 96% light absorption.[115] Another attractive property of MXene is the high hydrophilicity due to the presence of hydroxyl groups, which precludes the need to use organic solvents during the membrane fabrication. In addition, the abundant hydroxyl groups favor the interaction with other materials *via* hydrogen bonding to achieve desired structure and enhanced mechanical properties.[116-118] Owing to these appealing properties, MXene has been processed into various forms, such as compact/porous film,[114, 119-121] microspheres[122] and 3D aerogels,[116, 123, 124] and has been integrated with different materials to achieve high-performance solar evaporation.[119, 125] Wang and co-workers have reported a compact MXene film integrated with a thermal insulator exhibited a thermal efficiency of 84% under 1 $kW•m^{-2}$ (1 sun).[114] MXene aerogel with tunable pore shape and size has been demonstrated for efficient solar evaporation with thermal efficiency of 87% under 1 sun.[115] Although MXene-based solar evaporators exhibit high evaporation efficiency, freshwater generation efficiency significantly drops after integrating water collector. Thus, utilizing MXene in PMD membranes would unlock the full capability of MXene for more efficient resource use and effective clean water generation.

Chew and co-workers provided the first proof-of-concept of MXene in PMD and demonstrated that the flux of MXene-coated polyvinylidene fluoride (PVDF) membrane was 10% higher under solar irradiation than that in the absence of solar light, when treating preheated saline water (65°C).[35] However, MXene-coated PVDF membrane exhibited lower flux compared to pristine

PVDF membrane even under 5.8 sun light illumination. Such compromised performance in the presence of MXene results from the compact stacking structures of MXene, which greatly increases vapor transfer resistance. In addition, the compact MXene film possesses high thermal conductivity,[126, 127] which leads to large conductive heat loss across the membrane during membrane distillation, consequently lowing its thermal efficiency. These issues highlight the need for optimizing the MXene architecture for an enhanced membrane distillation performance. The PMD performance of MXene in treating saline water at ambient temperature (*i.e.*, non-preheated) has not been investigated yet. The ability to implement PMD using non-preheated saline water is critical in remote regions and disaster-struck communities, where hot feed water is not readily available.[29] Yet another consideration in the utilization of MXene as a photothermal material is that MXene can be easily oxidized in the presence of water and oxygen.[128] Most of the previous reports indicate that MXene-based photothermal membranes can achieve stable evaporation performance, [129-131] but a recent report indicates the partial oxidation of MXene after solar steam generation.[124] Considering that the oxidation of MXene can lead disintegration of the structures and deterioration of its photothermal performance, chemical stability of MXene membranes is highly important for its long-term stable desalination performance.

Accounting for more than 45% of all membrane fouling, biofouling is responsible for a significant decline in water flux in various membrane distillation processes.[50, 132, 133] The addition of disinfectants and biocides has been suggested to overcome biofouling, but some of these chemical agents are toxic and induce negative effects on the environment. Physical cleaning, such as ultrasonication cleaning and back flushing, increases operational costs and may cause damage to the membrane. Recently, photothermal effect and electric field have been proven as efficient and environment friendly methods to kill bacteria.[50, 80, 134-137] The photothermal membrane can kill bacteria effectively under sunlight irradiation owing to the photothermal effect, but it is not ideal

when solar light is weak. As an alternative disinfection method, the electric-field potential-driven disinfection can be achieved on the membrane possessing electric conductivity. Therefore, the membrane with excellent photothermal effect and electric conductivity is highly appealing to achieve versatile bactericide capability.

Herein, we introduce a highly efficient and chemically stable MXene composite aerogel for PMD with dual-mode anti-biofouling capability. In the MXene composite aerogel, polyvinyl alcohol (PVA) is used as a binder material to improve the structural stability, and hydroxyapatite (HA) nanowires are added to lower the thermal conductivity of the aerogel, which in turn reduces the conductive heat loss.[29, 60, 138] MXene composite aerogel, fabricated using ice-template assisted self-assembly, exhibits highly interconnected porous network, allowing low resistance for vapor transfer. The high porosity (up to 91%) and low thermal conductivity (0.12 $W \bullet m^{-1} \bullet K^{-1}$) of the composite aerogel enable high thermal efficiency, up to 61%, in treating ambient temperature saline feedwater under 0.8 sun illumination (0.8 $kW \bullet m^{-2}$). We also demonstrate the outstanding bactericidal activity of the MXene composite aerogel both under solar irradiation and under external electric potential, thus obviating the need for harsh chemical/physical treatments for bacterial lysis. This work sheds light on a great potential of MXene in realizing a highly efficient, stable and biofouling-resistant photothermal membrane for high-performance PMD systems.

4.3 Experimental Section

Synthesis of $Ti_3C_2T_x$ MXene flakes

$Ti_3C_2T_x$ MXene flakes were synthesized by selectively etching the Al layer of Ti_3AlC_2 using LiF/HCl as previously reported.[112] Specifically, LiF (2 g, Alfa Aesar) was added to the HCl (9M, 40 ml, Millipore Sigma) solution under stirring in a Teflon vessel to obtain homogeneous solution. Then, Ti_3AlC_2 powder (1 g, Shanghai Chenyue Metal Co., Ltd, China) was slowly added to the LiF/HCl solution, and the mixture was transferred to an oil bath at 35 °C and left under stirring for

24 hours. The resultant suspension was centrifuged at 3500 rpm for 5 minutes. After decanting the supernatant, the collected product was dispersed in water. This wash step was repeated until the pH of suspension was ~6. Finally, the suspension was subjected to sonication for 1 hour to delaminate the multilayer $Ti_3C_2T_x$ under Ar flow. After centrifuging at 3500 rpm for 1 hour, the $Ti_3C_2T_x$ flakes colloid was obtained by collecting the supernatant. After bubbling Ar for 20 minutes, the collected $Ti_3C_2T_x$ colloid was stored at 4 °C in a sealed vial.

Fabrication of MXene/PVA/HA aerogel and PVA/HA aerogel

HA nanowires were synthesized by the calcium oleate precursor *via* solvothermal reaction reported previously.[29] After dispersing the PVA powder (Mw 8,000~10,000, Millipore Sigma) in water, the mixture was kept in an oil bath at 60 °C for 2 hours under stirring to obtain a homogeneous solution. PVA solution (50 mg/ml, 0.5 ml) was added to $Ti_3C_2T_x$ colloid (17 mg/ml, 0.5 ml). Then, HA nanowires suspension (5 mg/ml, 1 ml) was added the homogenous mixture of $Ti_3C_2T_x$ and PVA. To fabricate PVA/HA aerogel, HA nanowires suspension (1 ml), the PVA solution (0.5 ml) and water (0.5 ml) were mixed homogeneously. To fabricate aerogel, the mixture was transferred to a petri dish with a diameter of 5.5 cm. After complete freezing at -20 °C, the mixture was freeze dried for 24 hours at -80 °C to obtain the aerogel.

Hydrophobic treatment

To convert the hydrophilic aerogel to hydrophobic aerogel, the MXene/PVA/HA aerogel was treated with (tridecafluoro-1,1,2,2-tetrahydrooctyl) trichlorosilane (FTCS, Millipore Sigma) vapor in a sealed container at 70 °C for 24 hours. Water contact angle of the aerogel was measured using a contact angle analyzer (Phoenix 300, Surface Electro Optics Co. Ltd) to confirm the hydrophobicity after FTCS treatment.

Optical properties and photothermal performance

Reflectance and transmittance spectra of aerogels were measured using a CRAIC micro spectrophotometer (QDI 302) coupled to a Leica optical microscope (DM 4000M) with a 20× objective in the range of 450–800 nm with 10 accumulations and 100 milliseconds exposure time in reflection and transmission mode, respectively. The surface temperature of aerogel with a size of 1 cm × 1 cm was monitored using an IR camera (FLIR E8-XT) under light illumination using a solar simulator (Newport 66921 Arc Lamp) with light intensity of 0.8 $kW \cdot m^{-2}$, as measured by a spectroradiometer (SpectriLight ILT 950).

Thermal conductivity measurement

The thermal conductivities of the MXene/PVA/HA aerogel were measured by monitoring the temperature distribution across the thickness of aerogel that were sandwiched between two glass microscope slides. The bottom glass slide was in contact with a hot plate and the top glass slide was in contact with ice. The temperature of the hot plate was increased from 70 °C to 120 °C, in steps of 10 °C. The vertical temperature distribution for the sandwich was monitored using a high-speed IR camera (Telops FAST M3k). The emissivity coefficient of a glass slide and a sample was assumed to be 0.9 to obtain the temperature distribution.[139] The Fourier equation was used to calculate the thermal conductivity of the aerogel:

$$q' = K\frac{\Delta T}{\Delta X}$$

The heat flux (q′) was calculated by assuming the thermal conductivity (K) of 1.05 $W \cdot m^{-1} \cdot K^{-1}$ for glass slides. Because the glass slide and samples experience the same heat flux, the heat flux value obtained for the glass slide was used to measure the thermal conductivity of the MXene/PVA/HA aerogel.

Nano- and micro-structure characterization

Scanning electron microscope (SEM) images of the surface and the cross-section of the aerogel and the nanowires were obtained after sputter coating the samples with gold. A FEI Nova 2300 field-emission SEM was used at an acceleration voltage of 10.5 kV. Atomic force microscopy (AFM) image was obtained using Dimension 3000 (Bruker) in light tapping mode. V-shaped silicon cantilever (Micromash) with a nominal tip radius of 8 nm were used for the imaging. The porosity was measured using isopropanol *via* previous reported solvent replacement method.[80]

Chemical stability measurement

X-ray photoelectron spectroscopy (XPS, PHI 5000 VersaProbe II, Ulvac-PHI with monochromatic Al Kα radiation) was utilized to measure the O 1s spectra of MXene to understand chemical nature and changes in the chemical functionality of MXene. The contact angle and XPS of FTCS-treated MXene/PVA/HA aerogel was monitored after 5-cycles PMD test. To investigate the effect of hydrophobic treatment on the long-term stability, pristine MXene/PVA/HA aerogel and FTCS-treated MXene/PVA/HA aerogel were immersed in 0.5 M NaCl solution for 1 week, respectively, and their chemical functionality was monitored and compared using XPS.

Photothermally-driven membrane distillation performance measurement

The PMD performance was evaluated using an air gap membrane distillation (AMD) module. The PMD cell was constructed using acrylonitrile butadiene styrene (ABS) plastic by 3D printing. The diameter of the membrane distillation cell was 3 cm, while the diameter of the membrane surface that was exposed to sunlight was measured to be 2.8 cm. The light illumination to AMD was achieved using a solar simulator under 0.8 sun illumination. NaCl aqueous solution (0.5 M) was employed as the feed water. The ambient feed water was continuously pumped using a peristaltic pump (model WPX1-F1/8S4−C, Welco Co. Ltd., Tokyo), with a flow rate of 1.57 ml•min^{-1}, 1.06 ml•min^{-1} and 0.62 ml•min^{-1} to achieve water retention time of 2 minutes, 3 minutes and 5 minutes, respectively. The thickness of the feed water was maintained at 5 mm. Aluminum foil was used as

the condensation surface on the permeate side with a 2 mm air gap. The amount of collected water was recorded using a weight scale (Sartorius ELT402).

Antibiofouling test

To test the bactericidal activity, the *E. coli* (pC013, Addgene) were cultured in Luria-Bertani (LB) liquid broth at 37 °C. All cultures were in 500 ml sterilized shake flasks (100 ml working volume, shaking at 250 rpm). After 12-hours culture, *E. coli* (~$6.4x10^8$ live cells/ml) were harvested. A layer of *E. coli* biofilm was formed on the surface of FTCS-treated MXene/PVA/HA aerogel by exposing it to the feed solution comprised of LB medium with *E. coli* for 30 minutes. To test the photothermal disinfection ability, the feed solution was removed from the aerogel and followed by 10-minutes sunlight irradiation with a light intensity of 0.8 $kW•m^{-2}$. To evaluate the bactericidal activity under electric potential, a two-electrode system consisting of a compact MXene film (~ 4 μm) and a polypropylene membrane as a spacer (3501 Coated PP, Celgard LLC) was employed. MXene film was fabricated by vacuum filtration of MXene colloids. The conductivity of MXene composite aerogel was measured using a four-point conductivity cell (BT-110, Scribner Associates). Negative potential (- 3.0 V) was applied on the aerogel for 30 minutes. The electrical potential was applied with a DC power supplier (Dr. Meter DC Power Supply HY3005D). The biofilm on the composite aerogel was monitored using fluorescent dyes (Molecular Probes Live/Dead Bacterial cell viability kit, Thermo Fisher Scientific), and the fluorescence images were collected using confocal laser scanning microscope (20× objective, Zeiss LSM 880 Laser Scanning Confocal Microscope) to identify the live bacteria and dead bacteria.

4.4 Results and Discussion

MXene composite aerogel was fabricated by integrating MXene flakes with PVA and HA nanowires (Figure 4.1). $Ti_3C_2T_x$ MXene flakes were synthesized by selectively etching the Al layer from Ti_3AlC_2 precursor using HCl/LiF and followed by sonication to delaminate the multilayer

$Ti_3C_2T_x$ MXene. The MXene flakes can be stably suspended in water, and the solution appeared dark-green in color (Figure 4.1). Scanning electron microscope (SEM) image revealed well-exfoliated $Ti_3C_2T_x$ sheets (Figure 4.2A), and the thickness measured by atomic force microscope (AFM) was 2.7 nm (Figure 4.2B). The successful preparation of $Ti_3C_2T_x$ was also confirmed by X-ray diffraction (XRD) analysis, showing the shift of the (002) peak to a lower 2θ angle, from the 9.5° in Ti_3AlC_2 to 7.1° in $Ti_3C_2T_x$, which corresponded to *d-spacing* shift from 9.2 Å to 12.4 Å (Figure 4.2C).[112, 140] The larger *d-spacing* in $Ti_3C_2T_x$ is ascribed to the introduction of terminal functional groups (*e.g.* -OH, -O and -F) and incorporation of water molecules.[141] To fabricate MXene composite aerogel, the Ti_3C_2Tx colloids, PVA solution (binder) and HA nanowires suspension were mixed. HA nanowires with outstanding flexibility were synthesized (Figure S3.1), by the previously report using calcium oleate precursor *via* a hydrothermal method.[29] PVA and HA nanowires spontaneously absorb on the MXene flakes owing to the abundant hydroxyl groups on each of these components, which facilitates by hydrogen bonding. The PVA/HA-wrapped MXene flakes were assembled into a 3D porous aerogel structure by freezing-induced ice crystal templating (-20 °C) and subsequent freeze drying (Figure 4.1).

The as-prepared black MXene/PVA/HA aerogel with a thickness of 400 μm (Figure 4.2H) exhibited superior mechanical flexibility (Figure 4.2D, 4.2G). SEM images (Figure 4.2E, 4.2H, 4.2I) revealed a 3D interconnected microporous structure, and the porosity was measured to be 91%. Such high porosity offers low resistance for water transport during PMD and contributes to high thermal efficiency. Another important factor determining the thermal efficiency of a PMD membrane is its thermal conductivity. High thermal conductivity results in conductive heat transfer across the membrane and reduces the temperature difference across the photothermal membrane, leading to high resistance for vapor transport and thus low thermal efficiency. The $Ti_3C_2T_x$ has been reported to exhibit relatively high thermal conductivity of 55.2 ± 1.7 $W•m^{-1}•K^{-1}$.[126] After

incorporating HA nanowires with low thermal conductivity and realizing stable aerogel structure with high porosity, the resultant composite aerogel exhibited low thermal conductivity, 0.12 $W \bullet m^{-1} \bullet K^{-1}$ (Figure 4.3A, 4.3B). This low thermal conductivity enables efficient thermal insulation and high temperature difference across the aerogel during PMD, leading to high driving force for vapor transport.[37]

To realize efficient desalination during PMD, the photothermal membrane needs to be hydrophobic in order to prevent liquid phase transport and to ensure that only vapor can diffuse across the membrane. Owing to the abundant hydroxyl groups, the composite aerogel was completely hydrophilic with a water contact angle of 0°. After silanization using tridecafluoro-1,1,2,2-tetrahydrooctyl)-trichlorosilane (FTCS), the contact angle of MXene/PVA/HA aerogel increased to 138° (Figure 4.3C), indicating the successful surface hydrophobic functionalization. The SEM images indicated that the highly porous network remained after this hydrophobic modification (Figure S3.2A, S3.2B).

Considering that the light absorption is critical for efficient photothermal performance, we investigated the light transmittance and reflectance of composite aerogel (Figure 4.3D, 4.3E). PVA/HA aerogel (without MXene) exhibited high transmittance (~42%) and reflectance (~39%) in the visible region, implying relatively small light extinction (~19%). On the other hand, the MXene/PVA/HA showed extremely low light transmittance (~2%) and reflectance (~1%), indicating a large light extinction (~97%). The large difference in the optical properties between PVA/HA aerogel and MXene aerogel stems from the broadband light absorption of MXene.[119] In addition, the highly porous structure of the aerogel can result in the multiple reflection when light travels through these pores and allows efficient light absorption.[75, 125] Without porous structure, a compact MXene film exhibited much higher light reflectance (~8%) (Figure S3.3A, S3.3B).

Next, we examined the photothermal performance of MXene/PVA/HA aerogel and compared it with that of PVA/HA aerogel. The surface temperature of these two aerogels in open air was monitored using an infrared camera, under simulated solar light illumination at a power density of 0.8 sun (Figure 4.3F). After light irradiation for 180 seconds, the surface temperature of the PVA/HA aerogel increased from ~25 °C to ~32 °C (Figure 4.3G), whereas the temperature of MXene/PVA/HA aerogel increased to ~62 °C under identical irradiation condition (Figure 4.3H). The higher surface temperature realized on the MXene/PVA/HA aerogel, compared to PVA/HA aerogel, highlights the outstanding light absorption and light-to-heat conversion enabled by MXene and its great potential in highly efficient PMD.

The PMD performance of MXene/PVA/HA was tested using air gap membrane distillation (AMD) module (Figure S3.4A, S3.4B). The feed water was maintained to be the same as our reported test conditions, 0.5 M NaCl solution at ambient temperature (20°C).[28, 29, 53] The feed water retention time can affect the PMD efficiency because of its effect on the heat transfer and temperature polarization on the photothermal membrane.[53, 109] Hence, different water retention times were tested (2 minutes, 3 minutes, and 5 minutes). After transporting through the photothermal membrane and air gap, the generated vapor finally condenses on a cold aluminum foil surface (Figure 4.4A). The collected freshwater is quantified by measuring the weight increase of the distillate as a function of irradiation time (Figure 4.4B). To evaluate the stability of PMD performance, the MXene composite aerogel was tested for over 5 cycles (each cycle for 1 hour). Under 0.8 sun illumination, the average water flux of the MXene/PVA/HA aerogel was 0.56 $kg•m^{-2}•h^{-1}$, 0.63 $kg•m^{-2}•h^{-1}$ and 0.72 $kg•m^{-2}•h^{-1}$ with water retention time of 2 minutes, 3 minutes, and 5 minutes, respectively (Figure 4.4C), and the variation in the flux within the same water retention time was less than 2%. The corresponding thermal efficiency of the MXene composite aerogel was calculated to be 48%, 54% and 61% for feed water retention time with 2 minutes, 3

minutes and 5 minutes, respectively (Figure 4.4D). The longer water retention time resulted in higher water flux and thermal efficiency. Under the same incident light, the longer retention time of feed water reduces the heat loss from the photothermal membrane to feed flow for more vapor generation,[109] and a larger temperature difference can also be achieved across the membrane for faster vapor transfer. However, increasing the water retention time can also lead to a decline in water flux as the slow feed rate increases the salt fouling propensity, eventually blocking vapor transport channels.[10, 142] Within the tested range of water retention time, high water flux can be obtained without salt accumulation on the composite aerogel when the water retention time of feed water is 5 minutes. However, further investigation needs to be conducted to determine optimal water retention time.

The thermal efficiencies (48%–61%) achieved on this MXene/PVA/HA aerogel is much higher than the previously reported PMD thermal efficiency realized by PVDF-supported photothermal membrane in treating ambient saline water, including carbon black nanoparticle-coated PVDF membrane (~22%)[109] and polydopamine (PDA)-coated PVDF membrane (~45%)[53]. In addition, FTCS-MXene/PVA/HA aerogel is comparable to the highly efficient photothermal membranes reported in PMD recently (Table S3.1). The superior PMD performance stems from the high porosity of the composite aerogel. Because high porosity is critical for ensuring unimpeded vapor transfer,[37] the higher porosity of MXene composite aerogel compared to previous PMD membranes enables the same. Specifically, the porosity of carbon black nanoparticle-coated and PDA-coated PVDF membrane was 65% and 75%, respectively, which are much lower than the porosity of the MXene composite aerogel (91%). Apart from low vapor transfer resistance, this MXene composite aerogel also exhibits optimal thermal management owing to its low thermal conductivity, which makes its overall thermal efficiency comparable to the recently reported high-performance bilayered photothermal membrane.[29, 80] Furthermore, incorporation of materials with

low thermal conductivity (*i.e.,* PVA and HA nanowires) suppresses the conductive heat transfer during PMD, facilitating larger temperature difference across the aerogel and leading to a stronger driving force for fast vapor transport.

FTCS-MXene/PVA/HA aerogel exhibited stable performance for over 5-cycles PMD test. The variations in the thermal efficiency were less than 2% (Figure 4.4D), and the salt rejection was around 99.9%. Even after vigorous mechanical agitation to for 2 weeks, the FTCS-MXene/PVA/HA aerogel did not display any signs of disintegration (Figure S3.5A), and no change in morphology was observed (Figure S3.5B), highlighting the potential for long-term stability for PMD application. We then evaluated the chemical stability of composite aerogel. The contact angle of FTCS-treated MXene/PVA/HA was 138°±1° and 135°±1° before and after 5-cycles PMD test, respectively (Figure 4.4E). The negligible change (variation less than 5%) in the contact angle of the aerogel indicated the robust surface modification and durable hydrophobicity for stable desalination. The chemical stability of MXene is important for long-term PMD performance. Based on previous studies, MXene can be easily oxidized into TiO_2 in the presence of oxygen and water,[129, 143] resulting in the deterioration in photothermal performance. While MXene-based solar evaporators have been extensively investigated,[114, 115, 119, 144] chemical instability of MXene is still of significant concern in their translation to real-world applications. Thus, the chemical composition of FTCS-treated MXene before and after PMD performance was probed using XPS. The O 1s region revealed that the peak attributed to TiO_2 at a binding energy of 529.9 eV[145] was virtually absent before and after 5-cycles PMD test, indicating the stable chemical structure of MXene over the multiple cycles (Figure 4.5E). Considering the easy oxidation of $Ti_3C_2T_x$ in the presence of water and air, we posit that the stability of $Ti_3C_2T_x$ stems from the FTCS treatment, which can prevent the direct contacting of water with $Ti_3C_2T_x$. To validate this hypothesis, using O1s peak in XPS, we monitored and compared the chemical

composition of MXene/PVA/HA and FTCS-treated MXene/PVA/HA aerogel after subjecting them to 0.5 M NaCl for 1 week (Figure 4.4F). For the composite aerogel without FTCS, the oxygen peak associated with TiO_2 was discernable (with 7% area under the peak attributed to TiO_2), whereas no discernable TiO_2-associate oxygen peak was observed in the FTCS-treated aerogel. The excellent chemical stability of FTCS-treated MXene/PVA/HA aerogel suggests that hydrophobic treatment is an effective method to prevent the oxidation of $Ti_3C_2T_x$. Current approaches to avoid the oxidation of $Ti_3C_2T_x$ involves freeze drying or the storage of $Ti_3C_2T_x$ colloids at low temperature (*e.g.*, aqueous solution at 4°C) in inert atmospheres to slow down the oxidation process. However, these approaches are not applicable for MXene-based solar evaporators. For the first time, our work first demonstrates the feasibility of realizing MXene-based 3D architectures with high chemical stability for long-term stable solar-driven desalination. To test the bactericidal ability, FTCS-treated MXene aerogel was exposed to *E. coli* in the culture medium to induce the formation of biofilm (Figure 4.5A1). We have employed live/dead cell staining assay to quantify the bactericidal activity of the aerogel. After 30-minutes growth without light illumination, substantial green fluorescence was observed on the MXene composite aerogel (Figure 4.5A2), suggesting the accumulation of live *E. coli* on the aerogel, and no signal of red fluorescence was noted (Figure 4.5A3), indicating the absence of dead bacteria.

To test the anti-biofouling performance, the *E. coli* adhered MXene composite aerogel was either irradiated with solar light or subjected to electric potential. First, for testing photothermally driven anti-biofouling, we drained the *E. coli* culture medium, and the composite aerogel was irradiated with solar light with 0.8 sun (Figure 4.5B1). Only red fluorescence was observed, while the green fluorescence disappeared, revealing that the solar irradiation was highly effective in killing the bacteria. It is known that bacteria become inactivated at temperature above 55°C after about five minutes.[146] Under sunlight irradiation, the surface temperature of MXene composite aerogel

reached up to 62 °C because of the photothermal effect, leading to effective disinfection by local surface heating.

To test the electric field-induced anti-biofouling, the MXene composite aerogel was integrated with a spacer and an electrode, as indicated in Figure 4.5C1. Then, negative voltage (- 3.0 V) was applied on the MXene composite aerogel covered with *E. coli* culture medium for 30 minutes to test the *in-situ* antibiofouling performance. Following the application of the voltage, we noted that a relatively small fraction (< 1%) of the bacteria exhibited green fluorescence (Figure 4.5C2), indicating live bacteria, while most of the bacteria exhibited red fluorescence (Figure 4.5C3), corresponding to the dead bacteria. These fluorescence images of MXene composite aerogel indicate that bacteria can be effectively killed when the composite aerogel is subjected to electric potential. MXene exhibits good conductivity,[147, 148] and the electrical conductivity of FTCS-treated MXene composite aerogel was measured to be 7.8 μS/cm. Considering the charged surface can damage the cell membrane structure directly,[134, 149] the MXene composite aerogel offers effective disinfection after being polarized with external electric potential. This capability is particularly important because sunlight can be intermittent. Moderate voltages required for effective bactericidal activity can be easily achieved by solar powered batteries, avoiding the need for additional energy sources. This electric field-induced antibiofouling performance serves as alternative method for cost-effective disinfection when solar light is not adequate. Therefore, based on excellent photothermal effect and electric conductivity, this MXene composite aerogel shows versatile bactericide capability under solar irradiation or electric potential. Compared with chemical treatment or physical cleaning, the built-in anti-biofouling property of the MXene composite aerogel obviates the need for toxic chemicals or physical processes damaging the membrane, making MXene aerogel highly appealing for treating bacteria-contaminated water.

4.5 Conclusions

In summary, we have successfully designed and fabricated an efficient and anti-biofouling MXene composite aerogel for highly efficient and stable PMD. The photothermal efficiency of the MXene/PVA/HA aerogel reached 61% under 0.8 sun illumination. This performance is superior to previously reported PVDF-supported photothermal membrane and comparable to recently reported thermally-engineered photothermal membrane, in treating the saline water at room temperature without any auxiliary heating system or heat recovery system. The as-prepared MXene/PVA/HA aerogel exhibited excellent photothermal performance owing to the broadband light absorption and high light-to-heat conversion efficiency of MXene. The high porosity and interconnected porous network created by an ice-templating method resulted in a low resistance to vapor transfer. Simultaneously, the composite aerogel exhibited low thermal conductivity, significantly reducing the conductive heat transfer from the evaporative surface to the cold permeate side and facilitating fast vapor transfer. FTCS-treatment minimized oxidation of MXene, providing excellent chemical stability to MXene/PVA/HA aerogel even under prolonged exposure to saline water. Furthermore, due to the inherent photothermal properties and electrical conductivity, MXene composite aerogel exhibited bactericidal activity under both solar irradiation and external electric potential. Owing to high thermal efficiency, chemical stability and versatile bactericidal activity, MXene composite aerogel is highly attractive in treating ambient saline water by utilizing the abundant sunlight, which is highly appealing for the freshwater generation in the remote regions and disaster-struck communities.

4.6 Supporting information

Supporting Information for chapter 4 is provided in appendix 3.

4.7 Figures

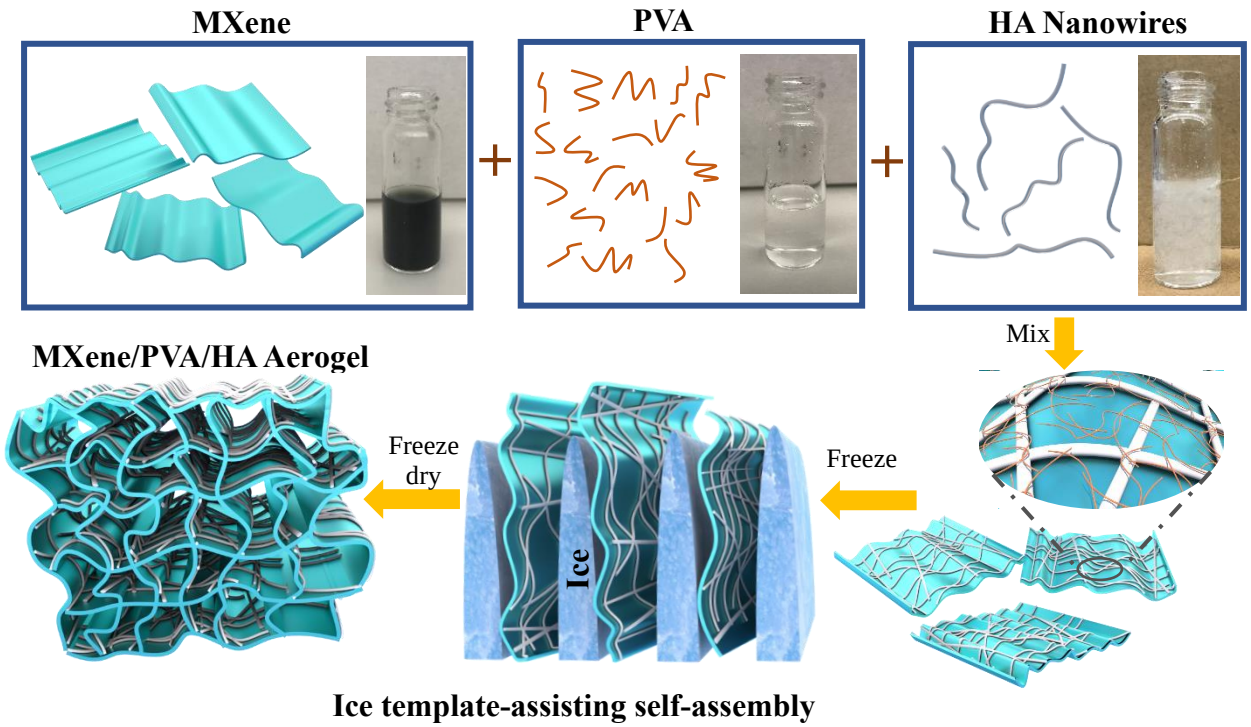

Figure 4.1. Schematic illustration showing the fabrication of MXene/PVA/HA aerogel using ice template-mediated self-assembly method. Upon mixing with MXene flakes, PVA and HA nanowires spontaneously wrap around the surface of MXene flakes. After freezing drying, the highly porous MXene composite aerogel is obtained.

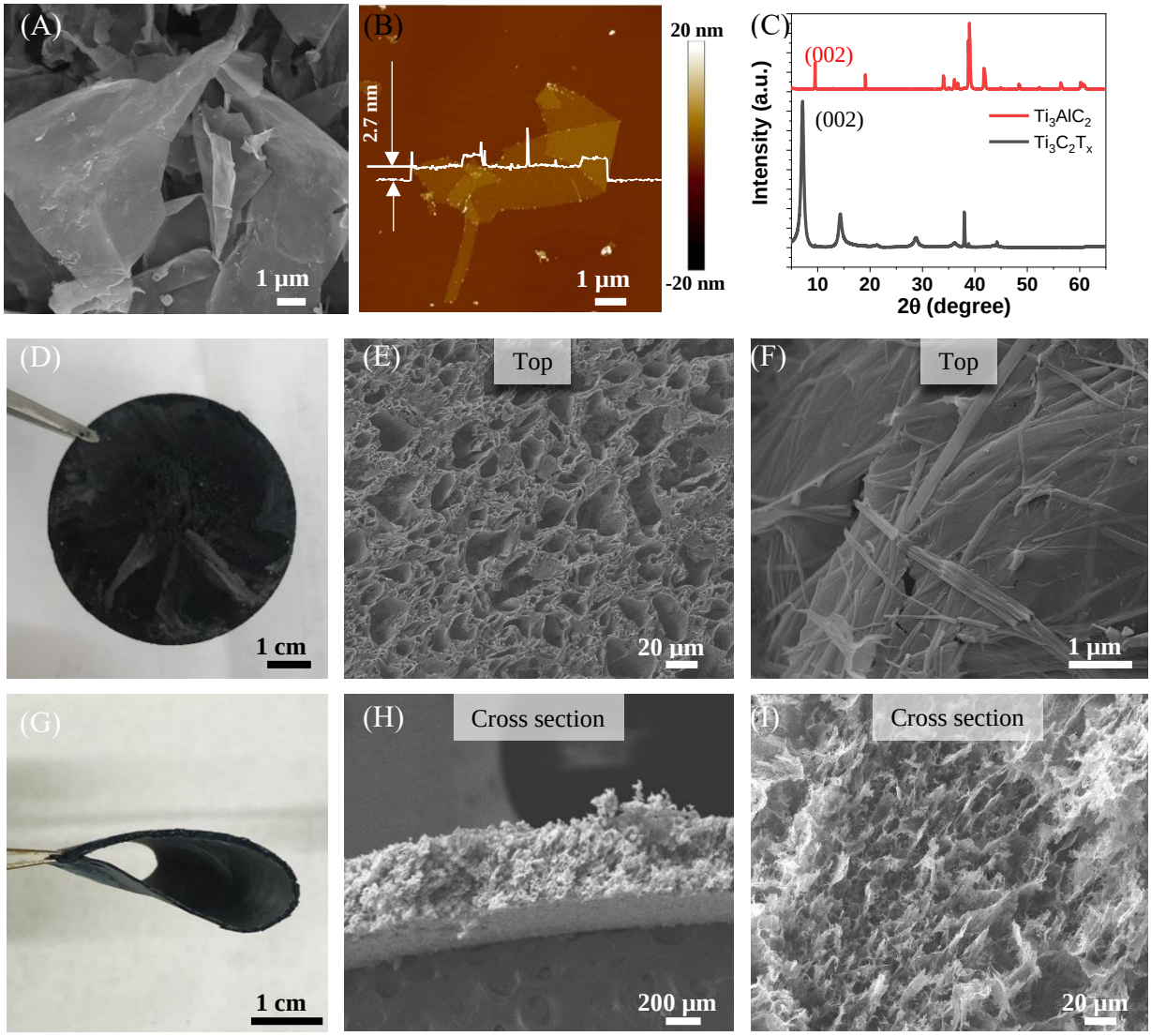

Figure 4.2. (A) SEM and (B) AFM image of MXene flakes. (C) Comparison of XRD patterns of Ti_3AlC_2 and Ti_3C_2Tx. Photograph of (D) as-prepared MXene/PVA/HA aerogel and (G) the deformed MXene composite aerogel. SEM images of the top surface of MXene composite aerogel in (E) low magnification and (F) high magnification. Cross-section SEM images of MXene composite aerogel in (H) low magnification and (I) high magnification.

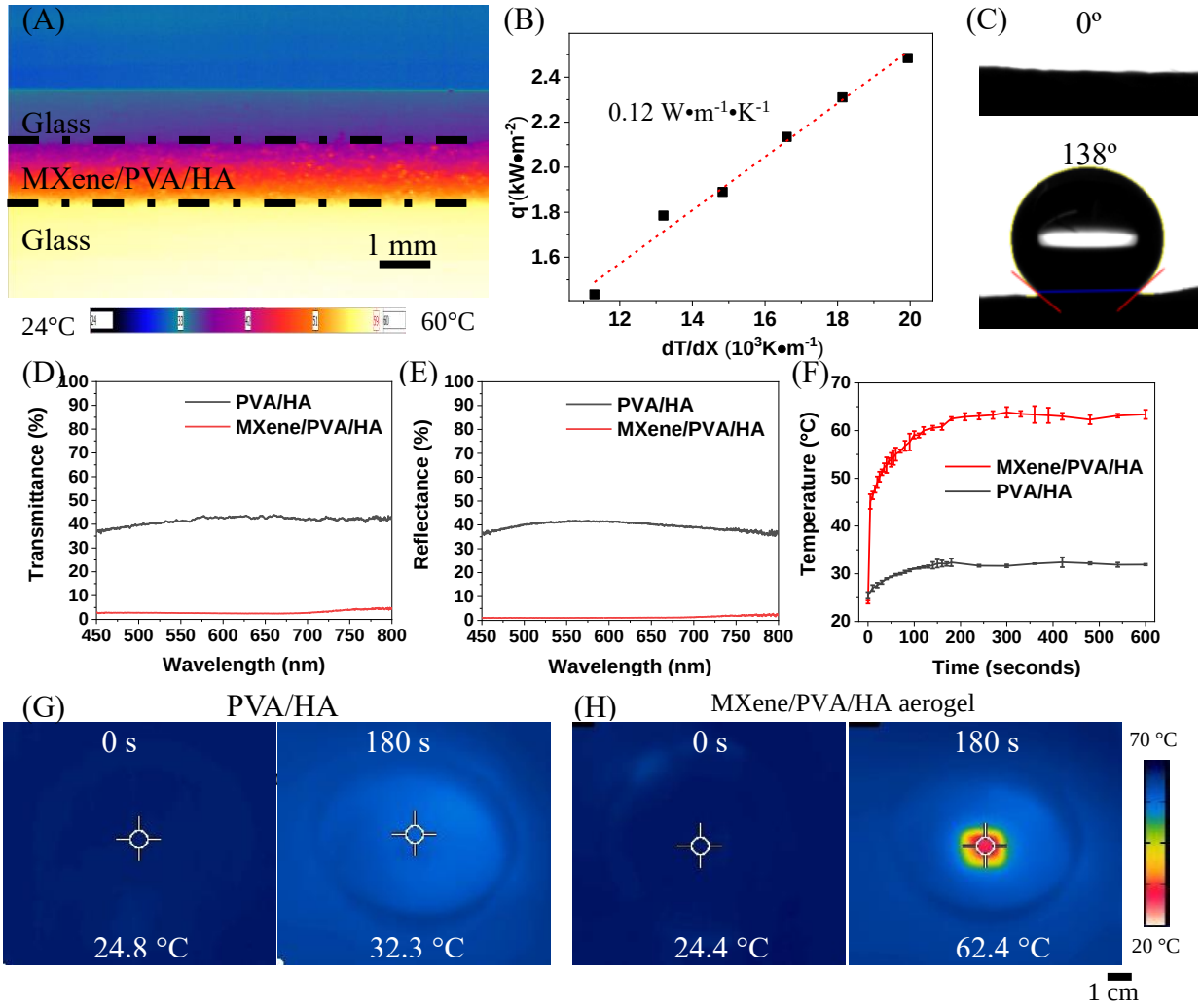

Figure 4.3. (A) Infrared image showing the temperature gradient along the thickness of the composite aerogel. (B) Thermal conductivity of MXene/PVA/HA aerogel. (C) Photograph showing the contact angle of MXene/PVA/HA aerogel (top) and FTCS-MXene/PVA/HA aerogel (bottom). (D) Reflectance and (E) transmittance spectra of the PVA/HA aerogel and MXene/PVA/HA aerogel. (F) Plots showing the surface temperature of the PVA/HA aerogel and MXene/PVA/HA aerogel under simulated sunlight irradiation with a power density of 0.8 $kW•m^{-2}$ as a function of irradiation time. Infrared images showing the surface temperature of (G) the PVA/HA aerogel and (H) MXene/PVA/HA aerogel under simulated sunlight illumination with a power density of 0.8 $kW•m^{-2}$ in open air after 180 seconds.

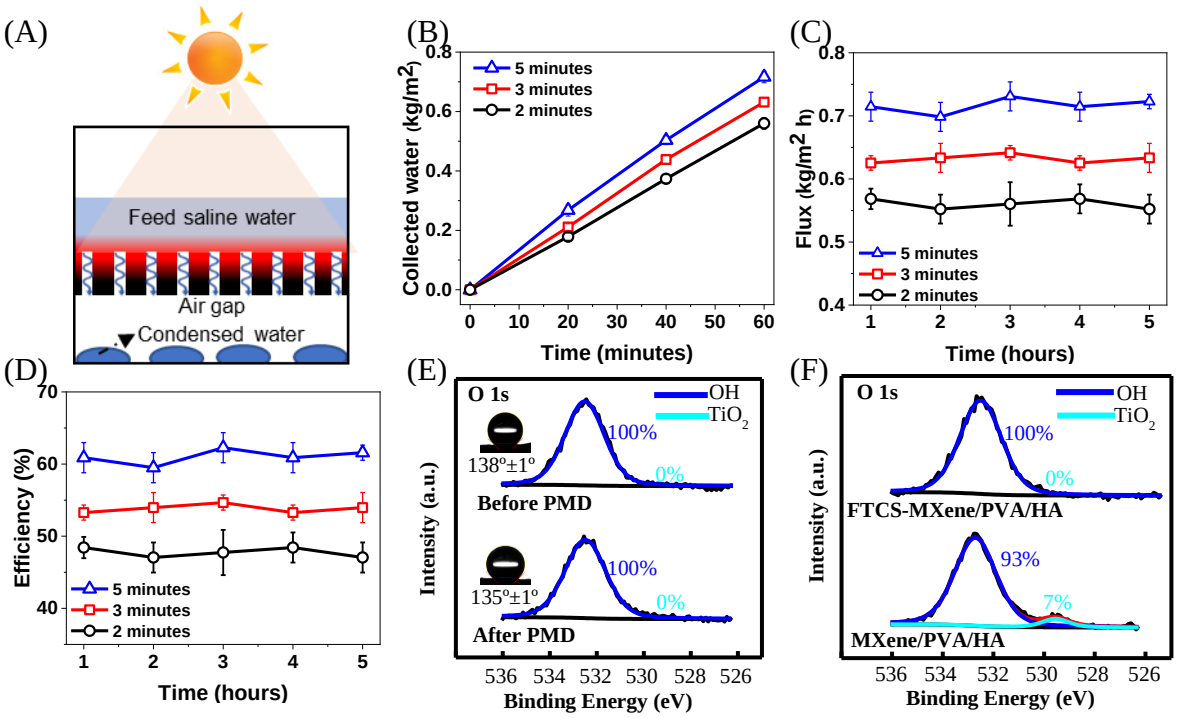

Figure 4.4. (A) Schematic illustration of AMD using FTCS-MXene/PVA/HA aerogel. (B) Collected water, (C) flux and (D) thermal efficiency of the PMD system using the FTCS-MXene/PVA/HA aerogel with varying feed water retention time, in purifying 0.5 M NaCl saline water under 0.8 sun irradiation over five consecutive cycles (each cycle for 1 hour, standard deviation obtained from measurements of 3 samples, error bars in (B) are smaller than the symbol size). (E) XPS of FTCS-MXene/PVA/HA aerogel before and after PMD test, insets show the contact angles of the aerogel before and after PMD test. (F) Comparison of XPS of FTCS-MXene/PVA/HA and MXene/PVA/HA aerogel after subjecting to 0.5 M NaCl solution for 1 week.

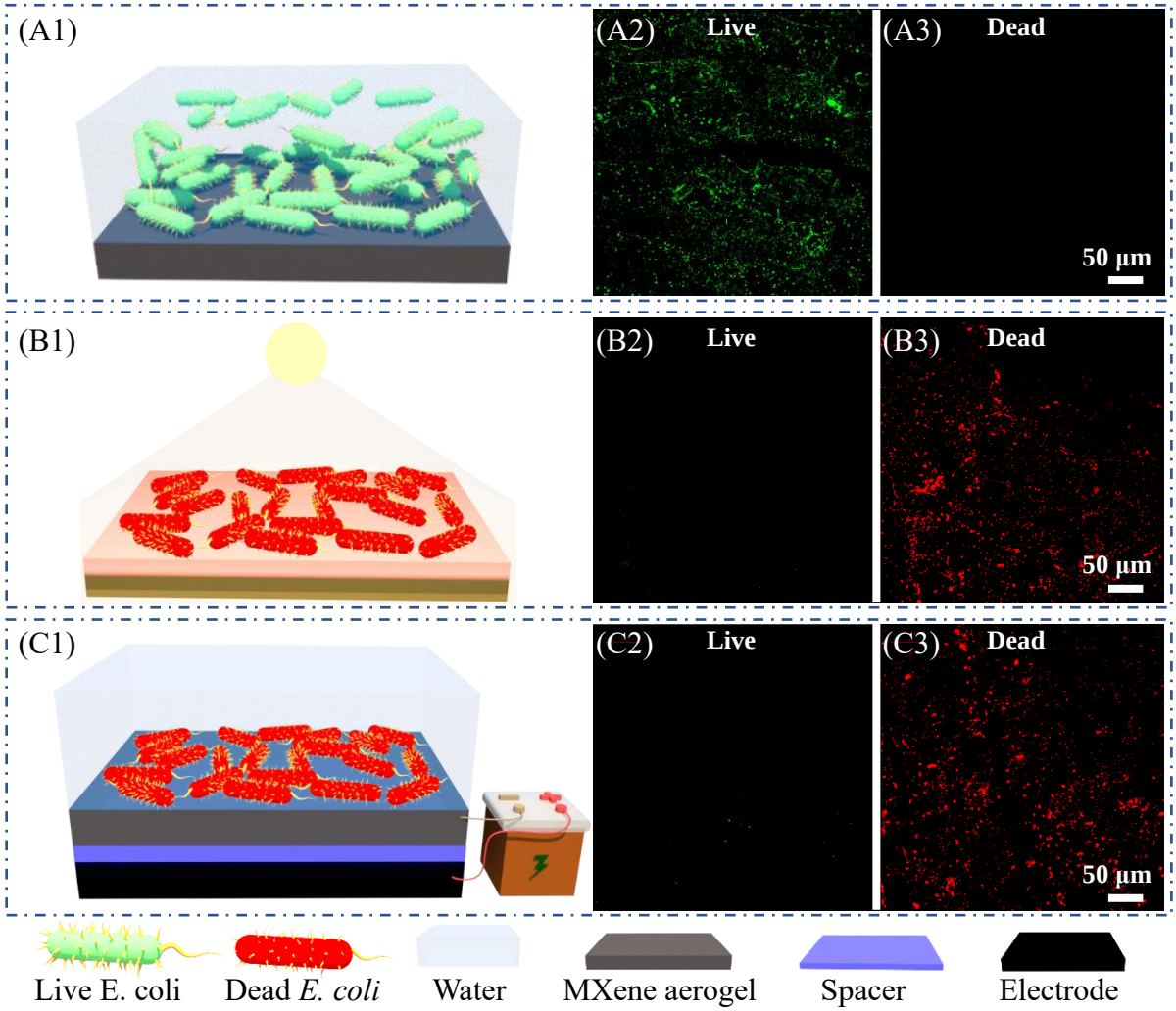

Figure 4.5. (A1) Schematic illustration showing the accumulation of *E. coli* on the surface FTCS-MXene/PVA/HA aerogel after exposure to the culture medium contaminated with *E. coli* for 30 minutes. Schematic illustration of antibiofouling performance enabled by FTCS-MXene/PVA/HA aerogel (B1) under solar irradiation in open air and (C1) after polarized with negative potential with a water thickness of 5 mm. Fluorescence images of *E. coli* on the surface of FTCS-MXene/PVA/HA aerogel (A2-A3) in pristine condition, (B2-B3) under solar irradiation in open air for 10 minutes and (C2-C3) after polarized with electric potential for 30 minutes.

Chapter 5: *In-Situ* Polymerization of Pyrrole as Universal Coating for Efficient Photothermal Driven Membrane Distillation

5.1 Abstract

Among current desalination technologies, photothermal driven membrane distillation (PMD) has been recognized as a highly promising and sustainable technology for freshwater generation. Polypyrrole (PPy) with easy synthesis and high stability is a highly promising photothermal material for PMD. Herein, we demonstrated the facile and universal PPy coating on commercial polymer membranes (hydrophilic polyvinylidene fluoride, hydrophobic polypropylene and hydrophobic polytetrafluoroethylene) for highly efficient PMD performance. Utilizing the ethanol as solvent, all polymer membranes could be coated with oxidizer, which initiated the growing of PPy *via* chemical vapor polymerization. The time of depositing PPy was much shorter compared with the time of loading polydopamine on membranes for high light absorption. In contrast with the poor affinity of existing photothermal materials to the substrates, this PPy coating on all membranes exhibited extraordinary robustness over vigorous mechanical agitation. Combined with preserved interconnected porous network after PPy deposition, all PPy-coated membranes achieved high thermal efficiency in PMD. Especially, the PPy-coated polyvinylidene fluoride membrane after hydrophobic treatment achieved a water flux of 2.53 $kg \bullet m^{-2} \bullet h^{-1}$ with a thermal efficiency of 72% under sunlight illumination with a power density of 2.4 $kW \bullet m^{-2}$, representing the highest thermal efficiency reported in treating ambient saline water in PMD. In this work, we first demonstrated that the universal PPy coating could be easily and quickly realized on various substrates, regardless of surface energy and curvature, to achieve high thermal efficiency in PMD.

This work sheds light on the great potential of PPy coating on other supporting substrates for high-performance PMD in treating saline water.

5.2 Introduction

More than 97% of water on earth is salt water, and freshwater is less than 2.5%.[54, 106] Combined with the exacerbated freshwater shortage by human activity, various desalination technologies have been developed to meet this challenge.[103, 104] Converting the sunlight to heat for water evaporation has been proposed as a sustainable desalination technology for freshwater generation.[50, 80, 150] Owing to the easy water collection and improved thermal efficiency, photothermal driven membrane distillation (PMD) is a highly promising solar-driven desalination technology, where membrane distillation is integrated with photothermal materials.[5, 44] In PMD, the feed saline water and cold permeate side locate at the opposite side of photothermal membrane. Due to the photothermal effect, the membrane surface is heated under incidental solar light, then vapor is generated at the interface of feed saline water and hydrophobic photothermal membrane.[19, 151] The vapor will transport from the top hot side to the cold permeate side, driven by the pressure gradient resulting from the temperature difference across the membrane.[80] Because of low temperature, the vapor condenses on the permeate side for freshwater generation.

To construct photothermal membranes for PMD, commercial polymer membranes have been widely employed as supporting substrates to load photothermal materials.[24, 32, 35, 44, 53, 76, 152-155] This is due to their low price, mechanical stability, scalability and low thermal conductivity.[106] However, it's difficult to directly deposit photothermal materials on these synthetic polymeric membranes, because of inert surface of polymer substrate.[29, 104] The binder materials are added to achieve stable deposition of the photothermal materials on the polymer substrates, [24, 44, 152, 153] which complicates the fabrication process. Apart from poor adhesion, the non-conformal and thick coating of photothermal materials on the curved surface blocks the pores of substrates,[24, 35, 44, 76,

[156] resulting the deteriorated the vapor transport. Porosity of photothermal membrane is critical for the thermal efficiency, as low porosity increases the resistance for the vapor transport.[5, 10] These problems highlight the need to develop photothermal materials allow easy synthesis, thin and conformal deposition, and high adhesion on substrates with different wettability for high performance photothermal membranes in PMD.

Polypyrrole (PPy) has been validated as one of promising photothermal materials, owing to its excellent photothermal property, easy synthesis, facile deposition, and high stability.[157, 158] The PPy possesses high light-to-heat conversion efficiency and offers broadband light absorption.[159] Owing to the distinctive flexibility, thin layer of PPy with controlled nanostructure can be directly deposited on the various substrates with curved structure, ranging from 2D substrates (*e.g.*, cotton fabric,[160] polypropylene (PP) mesh[158] and stainless-steel mesh[161]) to 3D substrates (*e.g.*, latex foam,[162] wood,[163, 164] sugarcane[165] and Setaria viridis spike[166]). The PPy coating can be facilely deposited *via* chemical vapor polymerization,[167] solution-phase polymerization,[158] and electrochemical polymerization.[168] Within 12-hours polymerization, efficient loading of PPy can be achieved to substrate for excellent photothermal performance.[158] The PPy exhibits high adhesion on the substrate with outstanding mechanical stability. No detachment of PPy from cotton fabric was observed using a tape test.[160] And the PPy-coated photothermal membrane can be bent and folded without any detachment.[169, 170] Although PPy has been extensively demonstrated as an excellent photothermal materials, developing simple and universal strategy for PPy deposition on the commercial polymeric membranes with different surface energy for PMD has not been studied yet.

Here, we demonstrate, for the first time, the simple and universal PPy coating on various polymeric membranes with different wettability for highly efficient PMD. Instead of water, ethanol is utilized as the solvent to dissolve $FeCl_3$, which allows efficient coating of oxidizer on the polymer

membranes with hydrophobic surface (PP and polytetrafluoroethylene (PTFE) membranes) as well as hydrophilic surface (polyvinylidene fluoride (PVDF) membrane). After exposing to the pyrrole vapor at moderate temperature for short time, efficient coating of PPy is realized on all polymer membranes. *Via* this two-step chemical vapor polymerization, all PPy-coated membranes possess excellent photothermal properties. Beside easy and fast deposition, the interconnected porous structure of polymer membranes is not affected, which allows efficient vapor transport in PMD. Owing to the excellent photothermal properties and preserved interconnected porous network, the PPy-coated polymer membranes after hydrophobic treatment achieve highly efficient PMD performance. The PPy-coated PVDF membrane achieves a water flux of 2.53 $kg \bullet m^{-2} \bullet h^{-1}$ with high thermal efficiency of 72% under 2.4 sun irradiation (1 sun = 1 $kW \bullet m^{-2}$), which represents the highest thermal efficiency reported in PMD system in treating ambient saline water. In addition, after subjection to vigorous mechanical agitation, no detachment of PPy from membrane is observed, which allows long-term stable PMD operation. We first demonstrate that the universal PPy coating can be easily and quickly deposited on various substrates, regardless of surface energy and curvature, to achieve high thermal efficiency in PMD.

5.3 Experimental Section

Preparation of FTCS-treated PPy-coated membranes.

Three kinds of commercial polymeric membranes were employed as supporting substrates for polypyrrole (PPy) coating: (1) hydrophilic polyvinylidene fluoride (PVDF) (0.45 μm pore size, 100 μm thickness, MilliporeSigma); (2) hydrophobic polypropylene (PP) (0.45 μm pore size, 240 μm thickness, Cole-Parmer); (3) hydrophobic polytetrafluoroethylene (PTFE) (3 μm pore size, 150 μm thickness, TISCH).The PPy coating on commercial polymeric membranes was achieved by chemical vapor polymerization of pyrrole (Sigma Aldrich). 0.5 M $FeCl_3$ solution was obtained by dissolving $FeCl_3$ (Sigma Aldrich) in ethanol (95%, Sigma Aldrich). The polymeric membranes

were immersed in $FeCl_3$ solution for 10 minutes. After drying at room temperature, the $FeCl_3$-coated membranes were exposed to pyrrole vapor in a sealed container at 60°C for 6 hours. The PPy-coated membranes were subjected to ethanol solution overnight to remove the excessive $FeCl_3$. After drying at 60°C for 10 minutes, the PPy-coated membranes were exposed to (tridecafluoro-1,1,2,2-tetrahydrooctyl)-trichlorosilane (FTCS) (Sigma Aldrich) vapor in a sealed container at 70 °C for 24 hours, to achieve hydrophobic treatment. Water contact angle of the membranes was measured using a contact angle analyzer (Phoenix 300, Surface Electro Optics Co. Ltd) to confirm the hydrophobicity after FTCS treatment.

Preparation of PDA-coated membranes

2 $mg \bullet ml^{-1}$ dopamine solution was obtained by dissolving dopamine (Sigma Aldrich) in 10 mM Tris-HCl buffer (pH = 8.5). Commercial polymeric membranes (PVDF, PP, PTFE) were immersed in in the mixture to allow the coating of polydopamine (PDA). After shaking for 24 hours (VWR Orbital Shaker, Model 3500), the PDA-coated membrane was washed with H_2O (18.2 MΩ-cm, Barnstead Ultrapure water systems) and followed by drying at 60°C for 10 minutes. This self-polymerization process was repeated for 5 days.

Membrane characterization

Scanning electron microscope (SEM) images of the surface and the cross-section of membranes were obtained after sputter coating the samples with gold. A FEI Nova 2300 field-emission SEM was used at an acceleration voltage of 10.5 kV. The chemical composition of PPy and FTCS on the PVDF were identified using X-ray photoelectron spectroscopy (XPS, PHI 5000 VersaProbe II, Ulvac-PHI. For XPS measurements, Al Kα monochromator radiation was used to measure the C 1s, N 1s, and Si 2p spectra of pure PVDF, PVDF@PPy, and FTCS-PVDF@PPy membranes.

Optical properties and photothermal performance measurement

Reflectance and transmittance spectra of membranes were obtained using a CRAIC micro spectrophotometer (QDI 302) coupled to a Leica optical microscope (DM 4000M) with a 20× objective in the range of 450–800 nm with 10 accumulations and 100 ms exposure time in reflection and transmission mode, respectively. The surface temperature of films was monitored using an IR camera (FLIR E8-XT) under light illumination using a solar simulator (Newport 66921 Arc Lamp) under both unfocused irradiation (1 sun) and focused irradiation (2.4 sun), as measured by a spectroradiometer (SpectriLight ILT 950).

Photothermal driven membrane distillation performance measurement

PMD was carried out in a customized membrane distillation module. All components of the module were 3D-printed (Prusa I3 MK3). Module was composed of a chamber for feed saline water with a dimension of 8 cm × 5.5 cm × 3 mm (L × W × H) and a chamber for permeate vapor with a dimension of 8.5 cm × 5.5 cm × 3 mm (L × W × H). A transparent polyethylene terephthalate (PET) film was glued on the top of the feed chamber. The bottom of feed chamber and top of permeate chamber located at the opposite sides of the PPy-coated membrane, and the connection was achieved using glue. The bottom of permeate chamber was glued with a thin aluminum plate. Underneath the aluminum plate, the coolant chamber with a dimension of 8.5 cm × 5.5 cm × 1.3 cm (L × W × H) was filled with circulated ambient water, so the vapor transported to the permeate chamber could condense on the aluminum plate. To collect the condensed water from the aluminum plate to a beaker, the water collector, by capillary action, a Kimwipe tissue was added on the aluminum plate.

During the PMD test, a light from a solar simulator (Newport 66921 Arc Lamp, power density: 2.4 sun) was shined onto the membrane in the vertically aligned PMD module. As feed water and coolant water, a 0.5 M NaCl solution at ambient temperature (~22ºC) was supplied to the feed chamber and coolant chamber using DC pumps. To reduce the heat loss from the photothermal

membrane to the feed water, the feed water in the photothermal layer was stagnant. To cool the aluminum plate efficiently, the water in the coolant chamber was circulated at a flow rate of 13 ml•min^{-1}. The collected water in the beaker was continuously weighted by a balance (Sartorius ELT402).

To evaluate salt rejection rate, the sodium concentration of the feed water and the permeate were determined by inductively coupled plasma mass spectrometry (ICP-MS), and then we calculated the rejection rate by using the following equation:

$$R(\%) = \frac{C_{Na,f} - C_{Na,d}}{C_{Na,f}} \times 100$$

where $C_{Na,f}$ and $C_{Na,f}$are the concentrations of sodium ions in the feed water and the permeate, respectively.

The thermal efficiency of the photothermal membrane was determined by the ratio of heat flux required to generate distillate flux to the total irradiated solar flux,

$$\eta = \frac{\dot{m} h_{vap}}{I}$$

where $\dot{m}$ represents the distillate flux of water, h_{vap} refers to the total evaporation enthalpy change, and I is the total incident solar flux. Given the water evaporation enthalpy of 2454 kJ•kg^{-1} (~0.68 kW•kg^{-1}•h^{-1}), the thermal efficiency was calculated based on the input solar flux and distillate flux.

Mechanical agitation

The membranes (1 cm × 1 cm) were placed in a 50 mL test tube filled with water, then it was subjected to sonication (Cole Parmer 8892 Ultrasonic Cleaner) for 1 hour.

5.4. Results and Discussion

PPy was coated on polymeric membranes *via* two-step chemical vapor polymerization (Figure 5.1). In this work, three widely used commercial polymer membranes with were tested: hydrophilic

PVDF, hydrophobic PP and hydrophobic PTFE membranes (Figure S4.1A-C). The porous membranes with different wettability are chosen to validate the universal coating of PPy for constructing photothermal membranes. The thickness for those three porous membranes is measured to be 100 nm for PVDF, 240 nm for PP and 150 nm for PTFE, respectively (Figure S4.2). The membranes were coated with $FeCl_3$, which was utilized as an oxidizer to induce the polymerization of pyrrole monomers. When using water as solvent, $FeCl_3$ can only be coated on the hydrophilic membranes, because hydrophobic membrane cannot be wetted by aqueous solution. UV/O_2 plasma treatment or grafting hydrophilic groups are required to covert the hydrophobic surface to be hydrophilic to anchor $FeCl_3$.[171-173] However, this complicates the process, and it may be costly and energy intensive. To allow efficient coating of $FeCl_3$ on substrates with different wettability, $FeCl_3$ was dissolved in the ethanol, because ethanol can wet hydrophilic/hydrophobic membranes. After immersing in the $FeCl_3$/ethanol solution and subsequently drying naturally, the color of all membranes changed from white from yellow (Figure S4.3), which indicated the immobilization of $FeCl_3$ on the membranes. Utilizing the ethanol as solvent obviates the need of pretreatment on membranes to load $FeCl_3$.

After exposing the $FeCl_3$-coated membranes to the pyrrole vapor at 60°C, the color of membranes quickly turned to black (Figure 5.2B, 5.2D, 5.2F), which corresponded to growth of PPy on the membrane. Owing to the high vapor pressure, pyrrole monomers can easily transit from liquid phase to vapor phase at moderate heating.[174, 175] After contacting $FeCl_3$, the polymerization of pyrrole quickly proceeds. Through the chemical vapor polymerization, PPy can stably grow on the membrane surface. Although PPy can be synthesized by other polymerization methods, the electrochemical polymerization is limited to electric conductive substrates, and solution-phase polymerization leads to the excess generation and waste of PPy.[158, 161] Thus, chemical vapor polymerization is highly appealing method to deposit PPy on the membranes. The XPS was conducted on the PVDF and PVDF@PPy membranes to indicate the successful loading of PPy. The newly appeared C 1s peaks at 286.3 eV corresponded to the N-C bond (Figure S4.4A), and the N 1s peak at 339.8 eV indicated the -NH group of PPy (Figure S4.4B), respectively.[176-178] SEM images revealed a smooth surface of the pristine polymer membranes (Figure 5.2A, 5.2C, 5.2E). Upon growing of PPy, a dense distribution of clusters and granules formed on polymer surface (Figure 5.2B, 5.2D, 5.2F). Most importantly, the interconnected porous network still remains, and PPy coating doesn't block the pores of polymer membranes (Figure 5.2A-F). This is because of

the thin and conformal deposition of PPy on the polymer fiber achieved by chemical vapor polymerization. After the evaporation of ethanol, $FeCl_3$ is coated on the polymer fiber surface, and PPy only grows on the regions where the oxidative agent is available during the chemical vapor polymerization process. Pores serve pathways for vapor transport in PMD, and the porous network of photothermal membrane allows low resistance to vapor transport.[5, 74] The conformal *in-situ* polymerization without deteriorating the porous network of membranes ensures the high thermal efficiency in PMD.

To investigate the light absorption of PPy-coated membranes, the optical transmittance and reflectance of pristine membranes and PPy-coated membranes are measured and compared. For the pristine PVDF membranes, the reflectance and transmittance were 61% and 5%, respectively, corresponding to light extinction of 34% (Figure 5.4A-B). The reflectance and transmittance of pristine PP membrane were 40% and 14%, respectively, corresponding to light extinction of 46% (Figure 5.4D-E). The reflectance and transmittance of pristine PTFE membrane were 40% and 29%, respectively, corresponding to light extinction of 31% (Figure 5.4G-H). After coating with PPy, all membranes exhibited very small reflectance (~2%) and no transmittance (Figure S4.6), which translated to a high light extinction (~98%). The difference in the optical properties is associated with presence of PPy, which is known to exhibit broadband light absorption. In addition, the interconnected porous structure of membranes causes the multiple reflection within the membrane, further enhancing the light absorption.[75]

In this work, it takes only 6 hours to grow sufficient PPy on the membranes, and this process is much faster compared with growing polydopamine (PDA) on membranes to achieve high light absorption.[53] As a well-known photothermal polymer, PDA is formed *via* oxidative self-polymerization of dopamine and exhibits high affinity to various surface, regardless of the initial surface energy.[67, 79] However, it requires long time to grow on substrates for high light absorption.[53] Immersing in 2 $mg \cdot ml^{-1}$ dopamine in Tris-HCl solution (pH = 8.5), the surface of membranes changed from white to dark brown after the polymerization process was repeated for 5 days (Figure S4.5A-C). Longer time polymerization of PDA resulted in smaller transmittance and reflectance. For the hydrophilic PVDF membranes, the transmittance of PDA-coated PVDF (PVDF@PDA) membranes exhibited no light transmittance after 1-day polymerization (Figure S4.6A), but the reflectance of PVDF@PDA was higher than PVDF@PPy membranes, even after 5-days polymerization (Figure S4.6B). For the hydrophobic PP and PTFE membranes, the

transmittance of PP@PDA and PTFE@PDA membranes were 4% and 8% after 1-day polymerization (Figure S4.6C, S4.6E), and the reflectance of PP@PDA and PTFE@PDA membranes were higher than PP@PPy and PTFE@PPy membranes, even after 5-days polymerization of dopamine (Figure S4.6D, S4.6F). Although PDA can be easily coated on various substrate, the PDA-coated membranes by 5-days polymerization exhibits lower light absorption than the PPy-coated membranes by 6-hours polymerization, which highlights the highly efficient loading of PPy on substrates to fabricated high-performance photothermal membrane.

To ensure the desalination in membrane distillation, the membrane surface is hydrophobic to allow only vapor transport and prevent liquid water transport.[5] The PVDF@PPy membrane was hydrophilic with a contact angle of 0° (Figure 5.3A). To achieve hydrophobic surface, the PVDF@PPy membrane was grafted with fluoro- functional groups using (tridecafluoro-1,1,2,2-tetrahydrooctyl)-trichlorosilane (FTCS). Compared with pristine PVDF and PVDF@PPy membrane, the newly appeared peak at 293.6 eV corresponding to the -CF_3 group and the peak at 104 eV corresponding to Si suggested the successful grafting of FTCS on the PVDF@PPy membrane (Figure S4.4A, S4.4C).[80, 179] The contact angle of FTCS-treat PVDF@PPy (FTCS-PVDF@PPy) membrane increased to 128° (Figure 5.3A), which indicated the successful hydrophobic modification. After FTCS treatment, the contact angle of PP@PPy membrane increased from 82° to 118° (Figure 5.3C). To precludes the effect of FTCS treatment, the PTFE@PPy membrane was also subjected to FTCS treatment, it possessed hydrophobic surface, though. The contact angle of PTFE@PPy membrane increased from 111° to 123° (Figure5. 3E). SEM images confirmed that the porous network of PPy-coated membranes was not affected by FTCS treatment (Figure 5.3B, 5.3D, 5.3F). The optical properties of PPy-coated membranes were also not affected by FTCS treatment. Similar with optical property of PPy-coated membranes, the FTCS-treated PPy-coated membranes also exhibited no transmittance (Figure 5.4A, 5.4D, 5.4G) and very small reflectance (~2%) (Figure 5.4B, 5.4E, 5.4H), translating into a high light extinction (~98%).

To achieve good photothermal performance, the amount of PPy grew on substrates has been investigated. The PVDF membrane is chosen as the substrate to reveal the effect of polymerization time on the loading amount of PPy. Longer time of polymerization results in higher loading amount of PPy. The amount of PPy loaded on the PVDF substrate was 2.8%, 4.2%, 6.9%, 8.1%, and 10% with polymerization time of 0.5 hour (PVDF_0.5h PPy), 1 hour (PVDF_1h PPy), 3 hours

(PVDF_3h PPy), 6 hours (PVDF_6h PPy) and 20 hours (PVDF_20h PPy) (Figure 5.5A), respectively. After irradiated with simulated sunlight, the surface temperature of PVDF membrane loaded with different amount of PPy has been recorded and compared. After irradiated for 360 seconds under 1 sun, the surface temperature of PVDF_0.5h PPy, PVDF_1h PPy, PVDF_3h PPy, PVDF_6h PPy and PVDF_20h PPy membranes increased to 60°C, 62°C, 64°C, 65°C and 66°C, respectively (Figure 5.5B). After irradiated for 360 seconds under 2.4 sun, the surface temperature of PVDF_0.5h PPy, PVDF_1h PPy, PVDF_3h PPy, PVDF_6h PPy and PVDF_20h PPy membranes increased to 152°C, 157°C, 154°C, 172°C and 177°C, respectively (Figure 5.5C). On the other hand, the surface temperatures of pristine PVDF membrane were 31°C and 35°C under 1 sun and 2.4 sun illumination for 360 seconds, respectively (Figure 5.5B-C). The much higher surface temperature achieved on the PVDF@PPy membranes is attributed to the excellent photothermal performance of PPy. Among the PVDF@PPy membranes, the higher loading of PPy on PVDF membranes resulted in higher surface temperature under solar light irradiation. However, the surface temperature of PVDF membranes after 6-hours reaction is only slightly lower than the membranes with 20-hours polymerization, but the reaction time is much shorter. Considering the reaction time and photothermal performance, the PVDF membrane with 6-hours polymerization of pyrrole is chosen for PMD test.

Next, we turn our attention to the PMD performance using the PPy-coated membranes. For all membranes, the polymerization time of pyrrole is 6 hours. The PMD performance of PPy-coated membranes were tested using air gap membrane distillation (AMD) module (Figure 5.1). Simulated seawater, 0.5 M NaCl solution with a thickness of 3 mm at ambient temperature (22°C), was used as the feed water. The air gap in the permeate side was 3 mm. After transporting through the photothermal membrane and air gap, the generated vapor finally condenses on a cold aluminum plate surface. The collected freshwater is quantified by measuring the weight increase of the distillate as a function of irradiation time. Under 2.4 sun irradiation, the water flux for FTCS-PVDF@PPy membranes was 2.65 $kg \cdot m^{-2} \cdot h^{-1}$ with a thermal efficiency of 75% (Figure 5.4C). Under identical test condition, the FTCS-PP@PPy membrane achieved a water flux of 2.01 $kg \cdot m^{-2} \cdot h^{-1}$ with a thermal efficiency of 57% (Figure 5.4I), and FTCS-PTFE@PPy membrane achieved a water flux of 2.15 $kg \cdot m^{-2} \cdot h^{-1}$ with a thermal efficiency of 61% (Figure 5.4F). The variation of thermal efficiency for the PPy-coated membranes is attributed to the properties of membrane, such as the thickness, porosity and thermal conductivity.[5, 29, 77]

The thermal efficiencies achieved with the FTCS-PP@PPy and FTCS-PTFE@PPy membranes are comparable to that of the recently reported highly efficient photothermal membranes using synthetic polymer as supporting substrate (45%~64%), treating the ambient saline water without heat recovery system in PMD.[32, 53, 152-154] For the FTCS-PVDF@PPy membrane, it achieves highest thermal efficiency reported in PMD in treating ambient saline water, which is much higher than that of the FTCS treated PDA/bacterial nanocellulose aerogel (~68%).[80] The is first study demonstrating that the universal PPy coating on various membranes, regardless of wettability and surface curvature, can achieve highly efficient PMD performance. The superior performance is closely related to the excellent photothermal property of PPy coating and the preserved porous network of the membranes. The broadband light absorption and high light-to-heat conversion efficiency achieved by the PPy coating on membranes result in high thermal energy output under light irradiation. Furthermore, the interconnected porous structure is preserved after the conformal and thin PPy deposition, which leads to a low resistance for vapor transport.

To evaluate the long-term PMD performance, the FTCS-PVDF@PPy membrane were tested over 30 consecutive cycles (each cycle for 20 minutes). Over cyclic test, the salt rejection rate was larger than 99.9% (Figure 5.5D), indicating the stable desalination performance achieved by the FTCS-PVDF@PPy membrane in PMD test. The high salt rejection rate rises from the excellent hydrophobicity of FTCS-PVDF@PPy membrane. The average water flux was 2.53 $kg \bullet m^{-2} \bullet h^{-1}$ (Figure 5.5E) and average thermal efficiency was 72% (Figure 5.5F) under 2.4 sun irradiation. The variation in the flux and thermal efficiency was around 1%, suggesting the long-term stable PMD performance achieved by the FTCS-PVDF@PPy membrane.

The mechanical stability of PPy-coated membranes was investigated by subjecting the membranes in ultrasonication for 1 hour. There was no discernible detachment of PPy from the membranes after the mechanical agitation (Figure S4.7A-C). Such excellent robustness is attributed to the high adhesion of PPy on the substrate achieved by *in-situ* polymerization, regardless of surface energy and curvature. On the other hand, most photothermal materials exhibit poor affinity to the inert surface of polymer substrates, and the direct deposition results in instability over mechanical agitation. For example, the graphene particles could be quickly spray coated on the PTFE membrane for excellent photothermal performance. However, most of graphene particles were detached from the substrate after sonication for 1 hour (Figure S4.7D). To improve the loading stability of photothermal materials on the substrate, binder materials with sticky functional groups

are usually added.[24, 44, 153] The graphene-loaded PTFE membrane was immersed in dopamine solution to grow PDA on the membrane, improving the deposition of graphene on PTFE membrane. Although the losing of graphene particles from the PTFE substrate was reduced (Figure S4.7E), the detachment was still noted even after the complicated treatment process, highlighting the advantage of *in-situ* polymerization of pyrrole coating. The robustness of the PPy-coating membranes enables us to reuse it multiple times without any noticeable degradation of the structure or PMD performance.

5.5 Conclusions

In summary, we have demonstrated the easy and universal PPy coating on various polymer membranes to construct photothermal membranes allowing highly efficient PMD performance. Utilizing the ethanol as a solvent, polymer substrates, regardless of surface energy and curvature, could be successfully coated with oxidizer, which initiates the deposition of PPy coating in the chemical vapor polymerization process. Unlike the long time required for depositing photothermally-active PDA, it only took 6 hours for PPy growing on membranes to achieve excellent photothermal properties without compromising the interconnected porous network. When treating the ambient saline water under 2.4 sun illumination, the FTCS-PP@PPy membrane achieves a water flux of 2.01 $kg•m^{-2}•h^{-1}$ with a thermal efficiency of 57%, and FTCS-PTFE@PPy membrane achieves a water flux of 2.15 $kg•m^{-2}•h^{-1}$ with a thermal efficiency of 61%. Under identical test condition over 30 cycles, the FTCS-PVDF@PPy membrane achieves average water flux of 2.53 $kg•m^{-2}•h^{-1}$ with a thermal efficiency of 72%, which represents the highest thermal efficiency reported in treating ambient saline water in PMD. In contrast with the poor affinity of existing photothermal materials to the substrates with inert surface, all PPy-coated membranes exhibit outstanding robustness under vigorous mechanical agitation, showing great potential for long-term PMD operation. The universal, highly efficient and mechanically stable PPy coating can be achieved on various porous substrates for freshwater generation in remote regions and disaster-struck communities by utilizing the abundantly available sunlight and saline water.

5.6 Supporting information

Supporting Information for chapter 4 is provided in appendix 4.

5.7 Figures

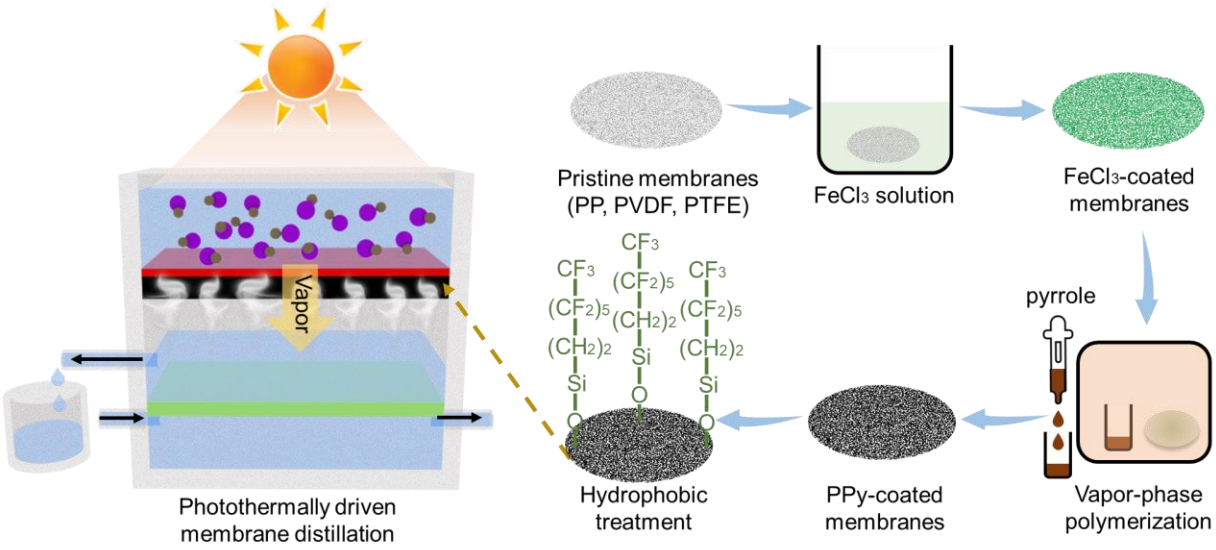

Figure 5.1. Schematic illustration showing the vapor-phase polymerization of pyrrole on the $FeCl_3$ coated polymeric membranes. After hydrophobic treatment using FTCS, the PPy-coated membranes are subjected to air-gap PMD.

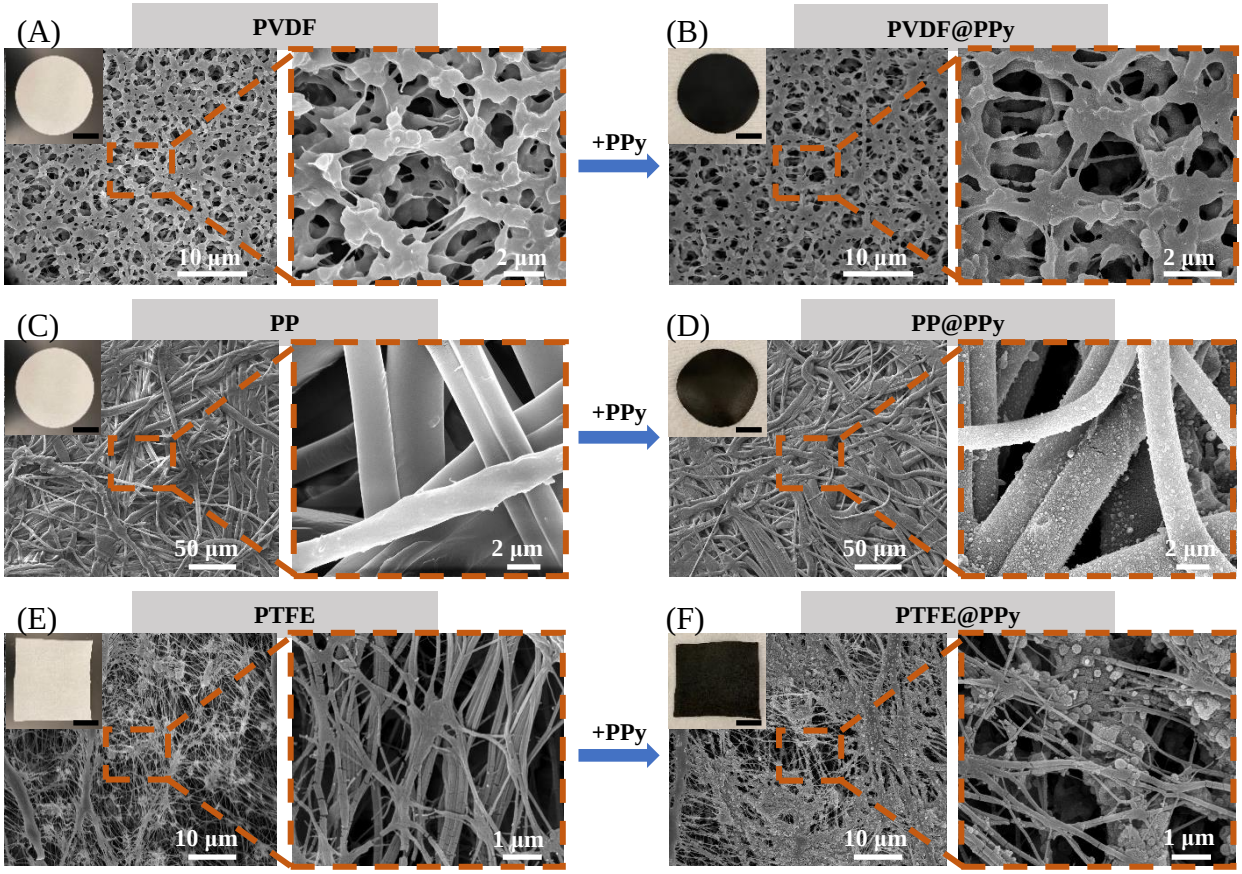

Figure 5.2. SEM images and photographs of polymeric membranes before and after PPy coating. SEM images of (A) PVDF, (B) PPy-coated PVDF, (C) PP, (D) PPy-coated PP, (E) PTEF and (F) PPy-coated PTFE membranes in low magnification and high magnification, insets are the corresponding photographs of membranes with a scale bar of 3 cm.

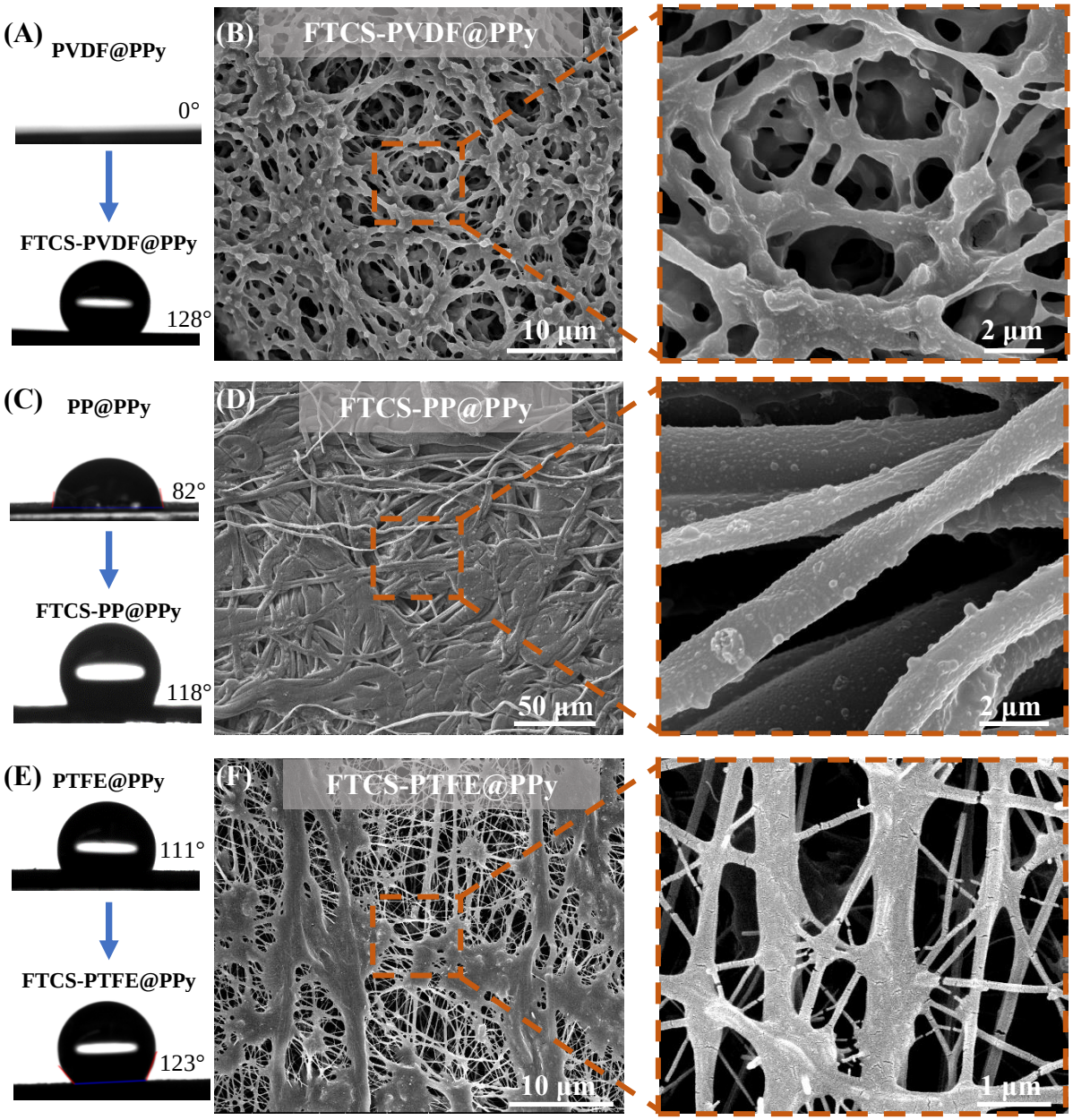

Figure 5.3. Photographs showing the contact angle of (A) PVDF@PPy (top) and FTCS-PVDF@PPy (bottom), (C) PP@PPy (top) and FTCS-PP@PPy (bottom), and (E) PTFE@PPy (top) and FTCS-PTFE@PPy (bottom) membranes. SEM images of (B) FTCS-PVDF@PPy, (D) FTCS-PP@PPy, and (F) FTCS-PTFE@PPy membranes in low magnification and high magnification.

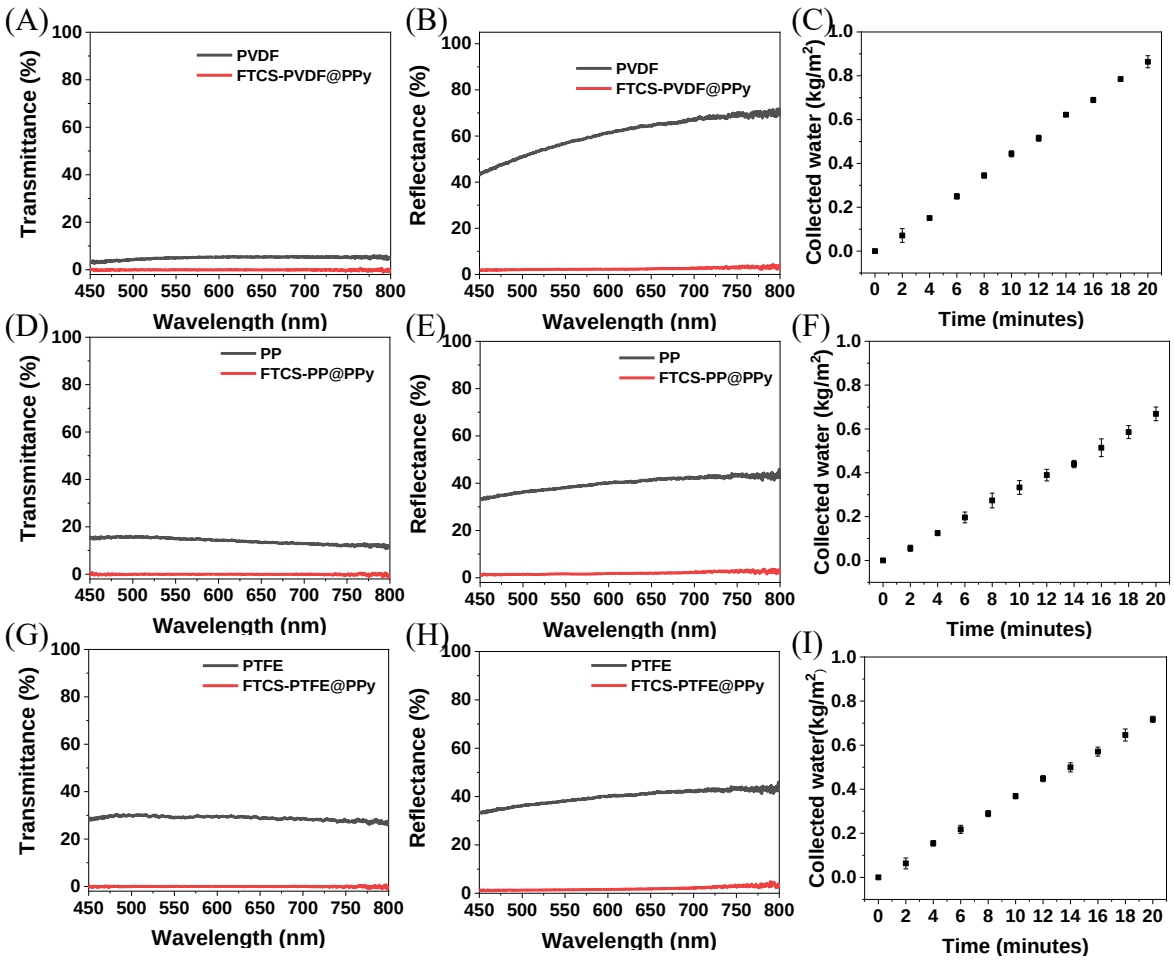

Figure 5.4. (A) Transmittance and (B) reflectance spectra of the pristine PVDF and FTCS-PVDF@PPy membranes. (D) Transmittance and (E) reflectance spectra of the pristine PP and FTCS-PP@PPy membranes. (G) Transmittance and (H) reflectance spectra of the pristine PTFE and FTCS- PTFE@PPy membranes. (C) Collected water of the PMD system using the (C) FTCS-PVDF@PPy, (F) FTCS-PP@PPy, and (I) FTCS-PTFE@PPy membranes.

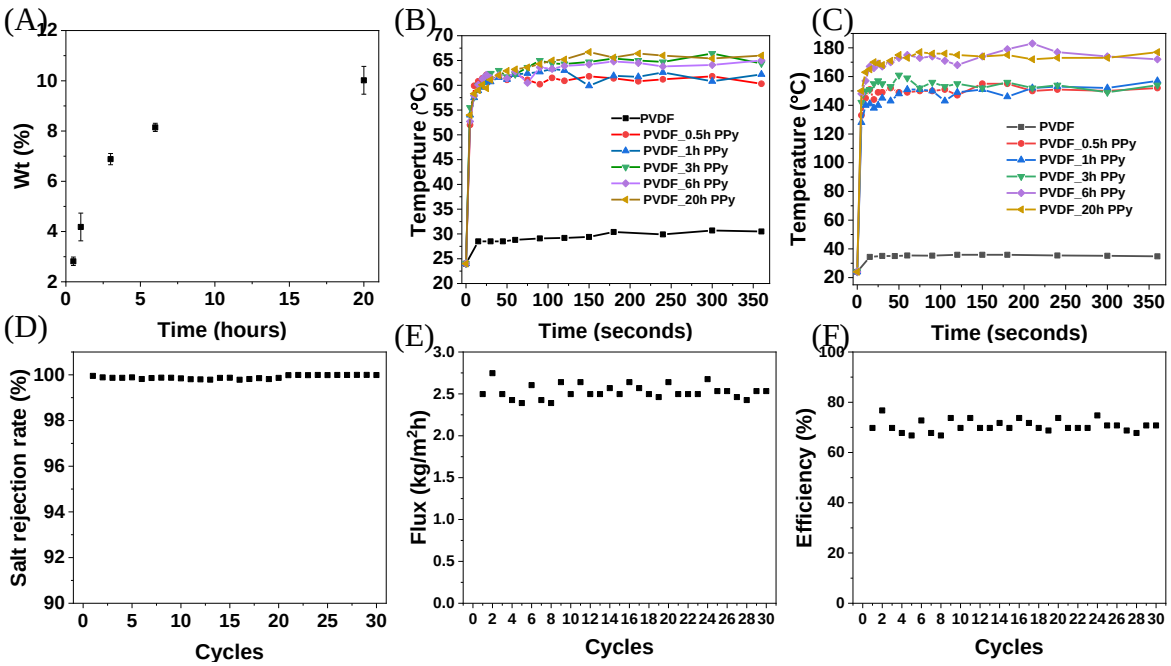

Figure 5.5. (A) Weight percentage of PPy on the PVDF membrane with different time of polymerization. (B) Plots showing the surface temperature of the PVDF membrane loaded with different amount of PPy under simulated sunlight irradiation with (B) 1 sun and (C) 2.4 sun as a function of irradiation time. (D) Salt rejection rate, (E) flux and (F) thermal efficiency of the PMD system using the FTCS-PVDF@PPy membrane in purifying 0.5 M NaCl saline water under 2.4 sun irradiation over 30 consecutive cycles (each cycle for 20 minutes).

Chapter 6: Conclusions

6.1 General conclusions

We have addressed several fundamental challenges in realizing materials and functional solar desalination systems with excellent photothermal performance, low resistance to vapor transfer and high resistance to heat transfer. We have introduced environment-friendly substrates and novel photothermal materials to construct thermally-engineered photothermal membranes for highly efficient PMD. The thermal efficiency of PMD using the novel photothermal membranes increased from 20% to above 60%. This work advances our understanding of the structure, properties, stability and performance of these novel materials and sheds light in designing and realizing photothermal membranes for highly efficient PMD systems.

We have demonstrated HA nanowires as an outstanding substrate material for realizing thermally engineered and environment friendly photothermal membranes for highly efficient PMD. The facile surface modification and large surface area make HA nanowires an outstanding template for PDA coating, resulting in excellent photothermal performance. The interconnected porous structure, formed by the highly flexible and intertwined nanowires, leads to low resistance to vapor transfer. Simultaneously, the low thermal conductivity of HA nanowires layer significantly reduces the conductive heat loss during PMD, resulting in higher thermal efficiency.

Apart from substrates, we have also studied the novel photothermal materials with multifunctionality to achieve highly efficient PMD. We have investigated their structure and properties and introduced structural designs of photothermal materials that overcome existing challenges in PMD membranes. We have investigated the photodegradation of PDA in ROS using plasmonic nanotransducers. Owing to the high sensitivity of LSPR wavelength to localized changes in dielectric medium around the AuNRs, small thickness change in the PDA layer can be monitored quickly by following the LSPR wavelength of AuNRs@PDA. Compared with conventional microscopy methods, the plasmonic nanotransducers offer fast and *in-situ* detection of PDA degradation. We found that •OH plays a significant role on the photodegradation of PDA, whereas H_2O_2 and O_2^- have less effect on the PDA decomposition.

In addition, we have demonstrated MXene as a multifunctional photothermal material in realizing photothermal membranes for highly efficient PMD with dual-mode antibiofouling performance. Through structural and chemical optimization, the MXene composite aerogel possessed high porosity and low thermal conductivity, resulting in high thermal efficiency in PMD. Owing to the excellent photothermal property and electrical conductivity, MXene aerogel enabled photothermal driven and electric field-induced antibiofouling performance.

We have also demonstrated the universal coating of PPy on different polymer membranes for highly efficient PMD performance. Through chemical vapor polymerization, the PPy could be easily and quickly coated on the polymer membranes, regardless of the wettability of the membrane. The PPy coating was highly stable and did not block the pores the substrates. Combined with the excellent photothermal performance, all PPy-coated membranes after hydrophobic treatment achieved highly efficient PMD performance.

6.2 Significance and outlook

In this study, we have demonstrated novel materials and fabrication strategies to realize high-performance photothermal membranes towards highly efficient PMD, there are still outstanding challenges that need to be addressed before these materials can be widely used in the real-world applications.

The average daily solar irradiance is around ~5 kW h per m^2 per day. Based the thermal efficiency achieved for the above photothermal membranes (>60%), the aera of photothermal membranes should be 0.5 m^2 to generate enough drinking water for an adult daily, 2 liters. Therefore, scalability of photothermal membranes in PMD is one of important factors that determines their real-world desalination. Among materials discussed above, HA nanowires The amount of daily drinking water for an adult, PDA and PPy can achieve large-scale manufacturing with low cost. However, MXene composite aerogels involving freeze-drying are not cost-effective. The drying process consumes large amount of energy and increases manufacturing cost, further compromising their viability for real-world application. Future efforts should focus on realizing photothermal membrane with scalable and cost-effective processes.

The lack of industry participation also delays the commercialization of this technique. Researchers mainly focus on developing novel materials and structural designs to maximize the thermal efficiency and to a large extent overlook the real-world problems that confront with the

implementation of these technologies. Considering that great strides have been made in thermal efficiency through novel photothermal and support materials and novel photothermal membrane designs in the past few years, involving industrial partners can support fast translation of the technology from the current stage to real applications.

Despite of these challenges in the transition of those photothermal membranes from laboratory scale to real-world implementation, the high thermal efficiency for freshwater generation makes them as a promising to achieve highly efficient solar-driven desalination around the world. Further exploration and optimization of materials chemistry, physical structure, and system designs will remain critical to advance those photothermal membranes to the real-world applications.

References

1. Ghim, D.; Jiang, Q.; Cao, S.; Singamaneni, S.; Jun, Y.-S., Mechanically interlocked 1T/2H phases of MoS2 nanosheets for solar thermal water purification. *Nano Energy* 2018, 53, 949-957.
2. *The United Nations World Water Development Report 2019 : LEAVING NO ONE BEHIND*. UNESCO: Paris, 2019; p 202.
3. Jiang, Q.; Ghim, D.; Cao, S.; Tadepalli, S.; Liu, K.-K.; Kwon, H.; Luan, J.; Min, Y.; Jun, Y.-S.; Singamaneni, S., Photothermally Active Reduced Graphene Oxide/Bacterial Nanocellulose Composites as Biofouling-Resistant Ultrafiltration Membranes. *Environmental science & technology* 2018, 53, 412-421.
4. Jun, Y.-S.; Wu, X.; Ghim, D.; Jiang, Q.; Cao, S.; Singamaneni, S., Photothermal Membrane Water Treatment for Two Worlds. *Accounts of Chemical Research* 2019.
5. Deshmukh, A.; Boo, C.; Karanikola, V.; Lin, S.; Straub, A. P.; Tong, T.; Warsinger, D. M.; Elimelech, M., Membrane distillation at the water-energy nexus: limits, opportunities, and challenges. *Energy & Environmental Science* 2018, 11, 1177-1196.
6. Boo, C.; Elimelech, M., Thermal desalination membranes: Carbon nanotubes keep up the heat. *Nature nanotechnology* 2017, 12, 501.
7. Goh, P.; Matsuura, T.; Ismail, A.; Hilal, N., Recent trends in membranes and membrane processes for desalination. *Desalination* 2016, 391, 43-60.
8. Ang, E. H.; Tan, Y. Z.; Chew, J. W., Three-Dimensional Plasmonic Spacer Enables Highly Efficient Solar-Enhanced Membrane Distillation of Seawater. *Journal of Materials Chemistry A* 2019.
9. Lawson, K. W.; Lloyd, D. R., Membrane distillation. *Journal of membrane Science* 1997, 124, 1-25.
10. Alkhudhiri, A.; Darwish, N.; Hilal, N., Membrane distillation: a comprehensive review. *Desalination* 2012, 287, 2-18.
11. Cath, T. Y.; Adams, V. D.; Childress, A. E., Experimental study of desalination using direct contact membrane distillation: a new approach to flux enhancement. *Journal of Membrane Science* 2004, 228, 5-16.
12. Camacho, L.; Dumée, L.; Zhang, J.; Li, J.-d.; Duke, M.; Gomez, J.; Gray, S., Advances in membrane distillation for water desalination and purification applications. *Water* 2013, 5, 94-196.
13. Gryta, M., Effectiveness of water desalination by membrane distillation process. *Membranes* 2012, 2, 415-429.
14. Long, R.; Lai, X.; Liu, Z.; Liu, W., Direct contact membrane distillation system for waste heat recovery: Modelling and multi-objective optimization. *Energy* 2018, 148, 1060-1068.
15. Boubakri, A.; Hafiane, A.; Bouguecha, S. A. T., Direct contact membrane distillation: capability to desalt raw water. *Arabian journal of chemistry* 2017, 10, S3475-S3481.
16. Li, C.; Li, X.; Du, X.; Tong, T.; Cath, T. Y.; Lee, J., Antiwetting and Antifouling Janus Membrane for Desalination of Saline Oily Wastewater by Membrane Distillation. *ACS applied materials & interfaces* 2019.
17. Dongare, P. D.; Alabastri, A.; Pedersen, S.; Zodrow, K. R.; Hogan, N. J.; Neumann, O.; Wu, J.; Wang, T.; Deshmukh, A.; Elimelech, M., Nanophotonics-enabled solar membrane

distillation for off-grid water purification. *Proceedings of the National Academy of Sciences* 2017, 114, 6936-6941.
18. Politano, A.; Di Profio, G.; Fontananova, E.; Sanna, V.; Cupolillo, A.; Curcio, E., Overcoming temperature polarization in membrane distillation by thermoplasmonic effects activated by Ag nanofillers in polymeric membranes. *Desalination* 2019, 451, 192-199.
19. Politano, A.; Argurio, P.; Di Profio, G.; Sanna, V.; Cupolillo, A.; Chakraborty, S.; Arafat, H. A.; Curcio, E., Photothermal membrane distillation for seawater desalination. *Advanced Materials* 2017, 29, 1603504.
20. Chen, C.; Kuang, Y.; Hu, L., Challenges and opportunities for solar evaporation. *Joule* 2019.
21. Jun, Y.-S.; Ghim, D.; Wu, X.; Cao, S.; Singamaneni, S., Solar Enabled Water Treatment in Resource Limited Settings. *HDIAC Journal* 2019, 6, 6.
22. Cao, S.; Jiang, Q.; Wu, X.; Ghim, D.; Gholami Derami, H.; Chou, P.-I.; Jun, Y.-S.; Singamaneni, S., Advances in solar evaporator materials for freshwater generation. *Journal of Materials Chemistry A* 2019.
23. Wang, W.; Shi, Y.; Zhang, C.; Hong, S.; Shi, L.; Chang, J.; Li, R.; Jin, Y.; Ong, C.; Zhuo, S.; Wang, P., Simultaneous production of fresh water and electricity via multistage solar photovoltaic membrane distillation. *Nature Communications* 2019, 10, 3012.
24. Dongare, P. D.; Alabastri, A.; Pedersen, S.; Zodrow, K. R.; Hogan, N. J.; Neumann, O.; Wu, J.; Wang, T.; Deshmukh, A.; Elimelech, M.; Li, Q.; Nordlander, P.; Halas, N. J., Nanophotonics-enabled solar membrane distillation for off-grid water purification. *Proceedings of the National Academy of Sciences* 2017, 114, 6936-6941.
25. Han, X.; Wang, W.; Zuo, K.; Chen, L.; Yuan, L.; Liang, J.; Li, Q.; Ajayan, P. M.; Zhao, Y.; Lou, J., Bio-derived ultrathin membrane for solar driven water purification. *Nano Energy* 2019, 60, 567-575.
26. Cao, S.; Jiang, Q.; Wu, X.; Ghim, D.; Derami, H. G.; Chou, P. I.; Jun, Y.-S.; Singamaneni, S., Advances in Solar Evaporator Materials for Freshwater Generation. *Journal of Materials Chemistry A* 2019.
27. Chamani, H.; Matsuura, T.; Rana, D.; Lan, C. Q., Modeling of pore wetting in vacuum membrane distillation. *Journal of membrane science* 2019, 572, 332-342.
28. Wu, X.; Cao, S.; Ghim, D.; Jiang, Q.; Singamaneni, S.; Jun, Y.-S., A thermally engineered polydopamine and bacterial nanocellulose bilayer membrane for photothermal membrane distillation with bactericidal capability. *Nano Energy* 2020, 105353.
29. Cao, S.; Wu, X.; Zhu, Y.; Gupta, R.; Tan, A.; Wang, Z.; Jun, Y.-S.; Singamaneni, S., Polydopamine/hydroxyapatite nanowire-based bilayered membrane for photothermal-driven membrane distillation. *Journal of Materials Chemistry A* 2020, 8, 5147-5156.
30. Shao, Y.; Han, M.; Wang, Y.; Li, G.; Xiao, W.; Li, X.; Wu, X.; Ruan, X.; Yan, X.; He, G.; Jiang, X., Superhydrophobic polypropylene membrane with fabricated antifouling interface for vacuum membrane distillation treating high concentration sodium/magnesium saline water. *Journal of Membrane Science* 2019, 579, 240-252.
31. Tadepalli, S.; Hamper, H.; Park, S. H.; Cao, S.; Naik, R. R.; Singamaneni, S., Adsorption behavior of silk fibroin on amphiphilic graphene oxide. *ACS Biomaterials Science & Engineering* 2016, 2, 1084-1092.
32. Huang, L.; Pei, J.; Jiang, H.; Hu, X., Water desalination under one sun using graphene-based material modified PTFE membrane. *Desalination* 2018, 442, 1-7.

33. Liao, Y.; Wang, R.; Fane, A. G., Fabrication of bioinspired composite nanofiber membranes with robust superhydrophobicity for direct contact membrane distillation. *Environmental science & technology* 2014, 48, 6335-6341.
34. Chen, T.; Soroush, A.; Rahaman, M. S., Highly Hydrophobic Electrospun Reduced Graphene Oxide/Poly (vinylidene fluoride-co-hexafluoropropylene) Membranes for Use in Membrane Distillation. *Industrial & Engineering Chemistry Research* 2018, 57, 14535-14543.
35. Tan, Y. Z.; Wang, H.; Han, L.; Tanis-Kanbur, M. B.; Pranav, M. V.; Chew, J. W., Photothermal-enhanced and fouling-resistant membrane for solar-assisted membrane distillation. *Journal of Membrane Science* 2018, 565, 254-265.
36. Han, L.; Tan, Y. Z.; Xu, C.; Xiao, T.; Trinh, T. A.; Chew, J. W., Zwitterionic grafting of sulfobetaine methacrylate (SBMA) on hydrophobic PVDF membranes for enhanced anti-fouling and anti-wetting in the membrane distillation of oil emulsions. *Journal of Membrane Science* 2019, 588, 117196.
37. Hou, D.; Li, T.; Chen, X.; He, S.; Dai, J.; Mofid, S. A.; Hou, D.; Iddya, A.; Jassby, D.; Yang, R.; Hu, L.; Ren, Z. J., Hydrophobic nanostructured wood membrane for thermally efficient distillation. *Science Advances* 2019, 5, eaaw3203.
38. Cao, S.; Tang, R.; Sudlow, G.; Wang, Z.; Liu, K.-K.; Luan, J.; Tadepalli, S.; Seth, A.; Achilefu, S.; Singamaneni, S., Shape-dependent biodistribution of biocompatible silk microcapsules. *ACS applied materials & interfaces* 2019, 11, 5499-5508.
39. Jiang, Q.; Derami, H. G.; Ghim, D.; Cao, S.; Jun, Y.-S.; Singamaneni, S., Polydopamine-filled bacterial nanocellulose as a biodegradable interfacial photothermal evaporator for highly efficient solar steam generation. *Journal of Materials Chemistry A* 2017, 5, 18397-18402.
40. Cao, S.; Rathi, P.; Wu, X.; Ghim, D.; Jun, Y. S.; Singamaneni, S., Cellulose Nanomaterials in Interfacial Evaporators for Desalination: A "Natural" Choice. *Advanced Materials* 2020, 2000922.
41. Ye, H.; Li, X.; Deng, L.; Li, P.; Zhang, T.; Wang, X.; Hsiao, B. S., Silver Nanoparticle-Enabled Photothermal Nanofibrous Membrane for Light-Driven Membrane Distillation. *Industrial & Engineering Chemistry Research* 2019, 58, 3269-3281.
42. Huang, Q.; Gao, S.; Huang, Y.; Zhang, M.; Xiao, C., Study on photothermal PVDF/ATO nanofiber membrane and its membrane distillation performance. *Journal of Membrane Science* 2019, 582, 203-210.
43. Cao, S.; Jiang, Q.; Wu, X.; Ghim, D.; Derami, H. G.; Chou, P.-I.; Jun, Y.-S.; Singamaneni, S., Advances in solar evaporator materials for freshwater generation. *Journal of Materials Chemistry A* 2019, 7, 24092-24123.
44. Ghim, D.; Wu, X.; Suazo, M.; Jun, Y.-S., Achieving maximum recovery of latent heat in photothermally driven multi-layer stacked membrane distillation. *Nano Energy* 2021, 80, 105444.
45. Krumova, K.; Cosa, G., Overview of reactive oxygen species. 2016.
46. Flemming, H. C.; Schaule, G.; Griebe, T.; Schmitt, J.; Tamachkiarowa, A., Workshop on Membranes in Drinking Water Production Technical Innovations and Health AspectsBiofouling—the Achilles heel of membrane processes. *Desalination* 1997, 113, 215-225.
47. Komlenic, R., Rethinking the causes of membrane biofouling. *Filtration & separation* 2010, 47, 26-28.
48. Baker, J. S.; Dudley, L. Y., Biofouling in membrane systems - A review. *Desalination* 1998, 118, 81-89.
49. *The United Nations world water development report 2019: Leaving No One Behind*. 2019; p 186.

50. Jiang, Q.; Ghim, D.; Cao, S.; Tadepalli, S.; Liu, K.-K.; Kwon, H.; Luan, J.; Min, Y.; Jun, Y.-S.; Singamaneni, S., Photothermally Active Reduced Graphene Oxide/Bacterial Nanocellulose Composites as Biofouling-Resistant Ultrafiltration Membranes. *Environmental Science & Technology* 2019, 53, 412-421.
51. Ang, E. H.; Tan, Y. Z.; Chew, J. W., A three-dimensional plasmonic spacer enables highly efficient solar-enhanced membrane distillation of seawater. *Journal of Materials Chemistry A* 2019, 7, 10206-10211.
52. Wang, Z.; Horseman, T.; Straub, A. P.; Yip, N. Y.; Li, D.; Elimelech, M.; Lin, S., Pathways and challenges for efficient solar-thermal desalination. *Science Advances* 2019, 5, eaax0763.
53. Wu, X.; Jiang, Q.; Ghim, D.; Singamaneni, S.; Jun, Y.-S., Localized heating with a photothermal polydopamine coating facilitates a novel membrane distillation process. *Journal of Materials Chemistry A* 2018, 6, 18799-18807.
54. Jun, Y.-S.; Wu, X.; Ghim, D.; Jiang, Q.; Cao, S.; Singamaneni, S., Photothermal Membrane Water Treatment for Two Worlds. *Accounts of Chemical Research* 2019, 52, 1215-1225.
55. Chiavazzo, E.; Morciano, M.; Viglino, F.; Fasano, M.; Asinari, P., Passive solar high-yield seawater desalination by modular and low-cost distillation. *Nature Sustainability* 2018, 1, 763-772.
56. Chen, F.-F.; Zhu, Y.-J.; Chen, F.; Dong, L.-Y.; Yang, R.-L.; Xiong, Z.-C., Fire alarm wallpaper based on fire-resistant hydroxyapatite nanowire inorganic paper and graphene oxide thermosensitive sensor. *ACS nano* 2018, 12, 3159-3171.
57. Lu, B. Q.; Zhu, Y. J.; Chen, F., Highly flexible and nonflammable inorganic hydroxyapatite paper. *Chemistry–A European Journal* 2014, 20, 1242-1246.
58. Sun, T. W.; Zhu, Y. J.; Chen, F., Highly flexible multifunctional biopaper comprising chitosan reinforced by ultralong hydroxyapatite nanowires. *Chemistry–A European Journal* 2017, 23, 3850-3862.
59. Li, H.; Wu, D.; Wu, J.; Dong, L. Y.; Zhu, Y. J.; Hu, X., Flexible, High-Wettability and Fire-Resistant Separators Based on Hydroxyapatite Nanowires for Advanced Lithium-Ion Batteries. *Advanced Materials* 2017, 29, 1703548.
60. Qin, D.-D.; Zhu, Y.-J.; Chen, F.-F.; Yang, R.-L.; Xiong, Z.-C., Self-floating aerogel composed of carbon nanotubes and ultralong hydroxyapatite nanowires for highly efficient solar energy-assisted water purification. *Carbon* 2019, 150, 233-243.
61. Chen, F.-F.; Zhu, Y.-J.; Xiong, Z.-C.; Sun, T.-W.; Shen, Y.-Q., Highly flexible superhydrophobic and fire-resistant layered inorganic paper. *ACS applied materials & interfaces* 2016, 8, 34715-34724.
62. Xiong, Z. C.; Zhu, Y. J.; Qin, D. D.; Chen, F. F.; Yang, R. L., Flexible Fire-Resistant Photothermal Paper Comprising Ultralong Hydroxyapatite Nanowires and Carbon Nanotubes for Solar Energy-Driven Water Purification. *Small* 2018, 14, 1803387.
63. Zong, L.; Li, M.; Li, C., Intensifying solar-thermal harvest of low-dimension biologic nanostructures for electric power and solar desalination. *Nano energy* 2018, 50, 308-315.
64. Wu, X.; Chen, G. Y.; Zhang, W.; Liu, X.; Xu, H., A plant-transpiration-process-inspired strategy for highly efficient solar evaporation. *Advanced Sustainable Systems* 2017, 1, 1700046.
65. Ray, S. S.; Chen, S.-S.; Ngoc Dan, C. T.; Hsu, H.-T.; Chang, H.-M.; Nguyen, N. C.; Nguyen, H.-T., Casting of a superhydrophobic membrane composed of polysulfone/Cera flava for improved desalination using a membrane distillation process. *RSC Advances* 2018, 8, 1808-1819.

66. Franken, A. C. M.; Nolten, J. A. M.; Mulder, M. H. V.; Bargeman, D.; Smolders, C. A., Wetting criteria for the applicability of membrane distillation. *Journal of Membrane Science* 1987, 33, 315-328.
67. Gholami Derami, H.; Jiang, Q.; Ghim, D.; Cao, S.; Chandar, Y. J.; Morrissey, J. J.; Jun, Y.-S.; Singamaneni, S., A Robust and Scalable Polydopamine/Bacterial Nanocellulose Hybrid Membrane for Efficient Wastewater Treatment. *ACS Applied Nano Materials* 2019, 2, 1092-1101.
68. Feng, J.; Fan, H.; Zha, D.-a.; Wang, L.; Jin, Z., Characterizations of the formation of polydopamine-coated halloysite nanotubes in various pH environments. *Langmuir* 2016, 32, 10377-10386.
69. Pérez-Mitta, G.; Tuninetti, J. S.; Knoll, W.; Trautmann, C.; Toimil-Molares, M. E.; Azzaroni, O., Polydopamine meets solid-state nanopores: A bioinspired integrative surface chemistry approach to tailor the functional properties of nanofluidic diodes. *Journal of the American Chemical Society* 2015, 137, 6011-6017.
70. Jiang, Q.; Tian, L.; Liu, K. K.; Tadepalli, S.; Raliya, R.; Biswas, P.; Naik, R. R.; Singamaneni, S., Bilayered biofoam for highly efficient solar steam generation. *Advanced Materials* 2016, 28, 9400-9407.
71. Ghasemi, H.; Ni, G.; Marconnet, A. M.; Loomis, J.; Yerci, S.; Miljkovic, N.; Chen, G., Solar steam generation by heat localization. *Nature communications* 2014, 5, 4449.
72. Li, C.; Li, X.; Du, X.; Tong, T.; Cath, T. Y.; Lee, J., Antiwetting and Antifouling Janus Membrane for Desalination of Saline Oily Wastewater by Membrane Distillation. *ACS Applied Materials & Interfaces* 2019, 11, 18456-18465.
73. Sun, M.; Boo, C.; Shi, W.; Rolf, J.; Shaulsky, E.; Cheng, W.; Plata, D. L.; Qu, J.; Elimelech, M., Engineering Carbon Nanotube Forest Superstructure for Robust Thermal Desalination Membranes. *Advanced Functional Materials* 2019, 29, 1903125.
74. Leitch, M. E.; Li, C.; Ikkala, O.; Mauter, M. S.; Lowry, G. V., Bacterial nanocellulose aerogel membranes: novel high-porosity materials for membrane distillation. *Environmental Science & Technology Letters* 2016, 3, 85-91.
75. Wang, P., Emerging investigator series: the rise of nano-enabled photothermal materials for water evaporation and clean water production by sunlight. *Environmental Science: Nano* 2018, 5, 1078-1089.
76. Wu, J.; Zodrow, K. R.; Szemraj, P. B.; Li, Q., Photothermal nanocomposite membranes for direct solar membrane distillation. *Journal of Materials Chemistry A* 2017, 5, 23712-23719.
77. An, X.; Xu, G.; Xie, B.; Hu, Y., Structural tailoring of hierarchical fibrous composite membranes to balance mass transfer and heat transfer for state-of-the-art desalination performance in membrane distillation. *Journal of Materials Chemistry A* 2019, 7, 2376-2384.
78. Franken, A.; Nolten, J.; Mulder, M.; Bargeman, D.; Smolders, C., Wetting criteria for the applicability of membrane distillation. *Journal of Membrane Science* 1987, 33, 315-328.
79. Liu, Y.; Ai, K.; Lu, L., Polydopamine and Its Derivative Materials: Synthesis and Promising Applications in Energy, Environmental, and Biomedical Fields. *Chemical Reviews* 2014, 114, 5057-5115.
80. Wu, X.; Cao, S.; Ghim, D.; Jiang, Q.; Singamaneni, S.; Jun, Y.-S., A thermally engineered polydopamine and bacterial nanocellulose bilayer membrane for photothermal membrane distillation with bactericidal capability. *Nano Energy* 2021, 79, 105353.
81. Blough, N. V.; Zepp, R. G., Reactive oxygen species in natural waters. In *Active oxygen in chemistry*, Springer: 1995; pp 280-333.

82. Held, P., An introduction to reactive oxygen species. *Tech Resources-App Guides* 2012, 802, 5-9.
83. Rubio-Clemente, A.; Chica, E.; Peñuela, G. A., Kinetic Modeling of the UV/H2O2 Process: Determining the Effective Hydroxyl Radical Concentration. *Physico-Chemical Wastewater Treatment and Resource Recovery* 2017, 19-41.
84. Bao, X.; Zhao, J.; Sun, J.; Hu, M.; Yang, X., Polydopamine Nanoparticles as Efficient Scavengers for Reactive Oxygen Species in Periodontal Disease. *ACS Nano* 2018, 12, 8882-8892.
85. Lin, J.-H.; Yu, C.-J.; Yang, Y.-C.; Tseng, W.-L., Formation of fluorescent polydopamine dots from hydroxyl radical-induced degradation of polydopamine nanoparticles. *Physical Chemistry Chemical Physics* 2015, 17, 15124-15130.
86. Tian, L.; Liu, K.-K.; Fei, M.; Tadepalli, S.; Cao, S.; Geldmeier, J. A.; Tsukruk, V. V.; Singamaneni, S., Plasmonic Nanogels for Unclonable Optical Tagging. *ACS Applied Materials & Interfaces* 2016, 8, 4031-4041.
87. Willets, K. A.; Van Duyne, R. P., Localized surface plasmon resonance spectroscopy and sensing. *Annu. Rev. Phys. Chem.* 2007, 58, 267-297.
88. Maier, S. A., *Plasmonics: fundamentals and applications*. Springer Science & Business Media: 2007.
89. Ozbay, E., Plasmonics: merging photonics and electronics at nanoscale dimensions. *science* 2006, 311, 189-193.
90. Mayer, K. M.; Hafner, J. H., Localized surface plasmon resonance sensors. *Chemical reviews* 2011, 111, 3828-3857.
91. Anker, J. N.; Hall, W. P.; Lyandres, O.; Shah, N. C.; Zhao, J.; Van Duyne, R. P., Biosensing with plasmonic nanosensors. In *Nanoscience And Technology: A Collection of Reviews from Nature Journals*, World Scientific: 2010; pp 308-319.
92. Bingham, J. M.; Anker, J. N.; Kreno, L. E.; Van Duyne, R. P., Gas sensing with high-resolution localized surface plasmon resonance spectroscopy. *Journal of the American Chemical Society* 2010, 132, 17358-17359.
93. Hall, W. P.; Modica, J.; Anker, J.; Lin, Y.; Mrksich, M.; Van Duyne, R. P., A conformation-and ion-sensitive plasmonic biosensor. *Nano letters* 2011, 11, 1098-1105.
94. Novo, C.; Funston, A. M.; Gooding, A. K.; Mulvaney, P., Electrochemical charging of single gold nanorods. *Journal of the American Chemical Society* 2009, 131, 14664-14666.
95. Novo, C.; Funston, A. M.; Mulvaney, P., Direct observation of chemical reactions on single gold nanocrystals using surface plasmon spectroscopy. *Nature nanotechnology* 2008, 3, 598.
96. Huang, X.; Neretina, S.; El-Sayed, M. A., Gold nanorods: from synthesis and properties to biological and biomedical applications. *Advanced Materials* 2009, 21, 4880-4910.
97. Tian, L.; Chen, E.; Gandra, N.; Abbas, A.; Singamaneni, S., Gold nanorods as plasmonic nanotransducers: distance-dependent refractive index sensitivity. *Langmuir* 2012, 28, 17435-17442.
98. Tian, L.; Fei, M.; Kattumenu, R.; Abbas, A.; Singamaneni, S., Gold nanorods as nanotransducers to monitor the growth and swelling of ultrathin polymer films. *Nanotechnology* 2012, 23, 255502.
99. Tadepalli, S.; Kuang, Z.; Jiang, Q.; Liu, K.-K.; Fisher, M. A.; Morrissey, J. J.; Kharasch, E. D.; Slocik, J. M.; Naik, R. R.; Singamaneni, S., Peptide functionalized gold nanorods for the sensitive detection of a cardiac biomarker using plasmonic paper devices. *Scientific reports* 2015, 5, 16206.

100. Park, J.; Fouché, L. D.; Hammond, P. T., Multicomponent patterning of layer-by-layer assembled polyelectrolyte/nanoparticle composite thin films with controlled alignment. *Advanced Materials* 2005, 17, 2575-2579.
101. Decher, G., Fuzzy nanoassemblies: toward layered polymeric multicomposites. *science* 1997, 277, 1232-1237.
102. Lu, G.; Hou, L.; Zhang, T.; Li, W.; Liu, J.; Perriat, P.; Gong, Q., Anisotropic plasmonic sensing of individual or coupled gold nanorods. *The Journal of Physical Chemistry C* 2011, 115, 22877-22885.
103. Chen, C.; Kuang, Y.; Hu, L., Challenges and Opportunities for Solar Evaporation. *Joule* 2019, 3, 683-718.
104. Cao, S.; Rathi, P.; Wu, X.; Ghim, D.; Jun, Y.-S.; Singamaneni, S., Cellulose Nanomaterials in Interfacial Evaporators for Desalination: A "Natural" Choice. *Advanced Materials* n/a, 2000922.
105. Kuang, Y.; Chen, C.; He, S.; Hitz, E. M.; Wang, Y.; Gan, W.; Mi, R.; Hu, L., A High-Performance Self-Regenerating Solar Evaporator for Continuous Water Desalination. *Advanced Materials* 2019, 31, 1900498.
106. Cao, S.; Jiang, Q.; Wu, X.; Ghim, D.; Gholami Derami, H.; Chou, P.-I.; Jun, Y.-S.; Singamaneni, S., Advances in solar evaporator materials for freshwater generation. *Journal of Materials Chemistry A* 2019, 7, 24092-24123.
107. Ni, G.; Zandavi, S. H.; Javid, S. M.; Boriskina, S. V.; Cooper, T. A.; Chen, G., A salt-rejecting floating solar still for low-cost desalination. *Energy & Environmental Science* 2018, 11, 1510-1519.
108. Zhu, L.; Gao, M.; Peh, C. K. N.; Wang, X.; Ho, G. W., Self-Contained Monolithic Carbon Sponges for Solar-Driven Interfacial Water Evaporation Distillation and Electricity Generation. *Advanced Energy Materials* 2018, 8, 1702149.
109. Dongare, P. D.; Alabastri, A.; Pedersen, S.; Zodrow, K. R.; Hogan, N. J.; Neumann, O.; Wu, J.; Wang, T.; Deshmukh, A.; Elimelech, M.; Li, Q.; Nordlander, P.; Halas, N. J., Nanophotonics-enabled solar membrane distillation for off-grid water purification. *Proceedings of the National Academy of Sciences of the United States of America* 2017, 114, 6936-6941.
110. Anasori, B.; Lukatskaya, M. R.; Gogotsi, Y., 2D metal carbides and nitrides (MXenes) for energy storage. *Nature Reviews Materials* 2017, 2, 16098.
111. Hong, S.; Ming, F.; Shi, Y.; Li, R.; Kim, I. S.; Tang, C. Y.; Alshareef, H. N.; Wang, P., Two-Dimensional Ti3C2Tx MXene Membranes as Nanofluidic Osmotic Power Generators. *ACS Nano* 2019, 13, 8917-8925.
112. Alhabeb, M.; Maleski, K.; Anasori, B.; Lelyukh, P.; Clark, L.; Sin, S.; Gogotsi, Y., Guidelines for Synthesis and Processing of Two-Dimensional Titanium Carbide (Ti3C2Tx MXene). *Chemistry of Materials* 2017, 29, 7633-7644.
113. Xie, Z.; Duo, Y.; Lin, Z.; Fan, T.; Xing, C.; Yu, L.; Wang, R.; Qiu, M.; Zhang, Y.; Zhao, Y.; Yan, X.; Zhang, H., The Rise of 2D Photothermal Materials beyond Graphene for Clean Water Production. *Advanced Science* 2020, 7, 1902236.
114. Li, R.; Zhang, L.; Shi, L.; Wang, P., MXene Ti3C2: An Effective 2D Light-to-Heat Conversion Material. *ACS Nano* 2017, 11, 3752-3759.
115. Zhang, Q.; Yi, G.; Fu, Z.; Yu, H.; Chen, S.; Quan, X., Vertically Aligned Janus MXene-Based Aerogels for Solar Desalination with High Efficiency and Salt Resistance. *ACS Nano* 2019, 13, 13196-13207.

116. Ming, X.; Guo, A.; Zhang, Q.; Guo, Z.; Yu, F.; Hou, B.; Wang, Y.; Homewood, K. P.; Wang, X., 3D macroscopic graphene oxide/MXene architectures for multifunctional water purification. *Carbon* 2020, 167, 285-295.
117. Liu, J.; Zhang, H.-B.; Xie, X.; Yang, R.; Liu, Z.; Liu, Y.; Yu, Z.-Z., Multifunctional, Superelastic, and Lightweight MXene/Polyimide Aerogels. *Small* 2018, 14, 1802479.
118. Krecker, M. C.; Bukharina, D.; Hatter, C. B.; Gogotsi, Y.; Tsukruk, V. V., Bioencapsulated MXene Flakes for Enhanced Stability and Composite Precursors. *Advanced Functional Materials* 2020, 30, 2004554.
119. Tang, L.; Zhao, X.; Feng, C.; Bai, L.; Yang, J.; Bao, R.; Liu, Z.; Yang, M.; Yang, W., Bacterial cellulose/MXene hybrid aerogels for photodriven shape-stabilized composite phase change materials. *Solar Energy Materials and Solar Cells* 2019, 203, 110174.
120. Zhao, J.; Yang, Y.; Yang, C.; Tian, Y.; Han, Y.; Liu, J.; Yin, X.; Que, W., A hydrophobic surface enabled salt-blocking 2D Ti3C2 MXene membrane for efficient and stable solar desalination. *Journal of Materials Chemistry A* 2018, 6, 16196-16204.
121. Liu, J.; Zhang, H.-B.; Sun, R.; Liu, Y.; Liu, Z.; Zhou, A.; Yu, Z.-Z., Hydrophobic, Flexible, and Lightweight MXene Foams for High-Performance Electromagnetic-Interference Shielding. *Advanced Materials* 2017, 29, 1702367.
122. Zhao, X.; Zha, X.-J.; Tang, L.-S.; Pu, J.-H.; Ke, K.; Bao, R.-Y.; Liu, Z.-y.; Yang, M.-B.; Yang, W., Self-assembled core-shell polydopamine@MXene with synergistic solar absorption capability for highly efficient solar-to-vapor generation. *Nano Research* 2020, 13, 255-264.
123. Fan, X.; Yang, Y.; Shi, X.; Liu, Y.; Li, H.; Liang, J.; Chen, Y., A MXene-Based Hierarchical Design Enabling Highly Efficient and Stable Solar-Water Desalination with Good Salt Resistance. *Advanced Functional Materials* n/a, 2007110.
124. Zhao, X.; Peng, L.-M.; Tang, C.-Y.; Pu, J.-H.; Zha, X.-J.; Ke, K.; Bao, R.-Y.; Yang, M.-B.; Yang, W., All-weather-available, continuous steam generation based on the synergistic photo-thermal and electro-thermal conversion by MXene-based aerogels. *Materials Horizons* 2020, 7, 855-865.
125. Li, K.; Chang, T.-H.; Li, Z.; Yang, H.; Fu, F.; Li, T.; Ho, J. S.; Chen, P.-Y., Biomimetic MXene Textures with Enhanced Light-to-Heat Conversion for Solar Steam Generation and Wearable Thermal Management. *Advanced Energy Materials* 2019, 9, 1901687.
126. Chen, L.; Shi, X.; Yu, N.; Zhang, X.; Du, X.; Lin, J., Measurement and analysis of thermal conductivity of Ti3C2Tx MXene films. *Materials* 2018, 11, 1701.
127. Gholivand, H.; Fuladi, S.; Hemmat, Z.; Salehi-Khojin, A.; Khalili-Araghi, F., Effect of surface termination on the lattice thermal conductivity of monolayer Ti3C2Tz MXenes. *Journal of Applied Physics* 2019, 126, 065101.
128. Lee, Y.; Kim, S. J.; Kim, Y.-J.; Lim, Y.; Chae, Y.; Lee, B.-J.; Kim, Y.-T.; Han, H.; Gogotsi, Y.; Ahn, C. W., Oxidation-resistant titanium carbide MXene films. *Journal of Materials Chemistry A* 2020, 8, 573-581.
129. Chae, Y.; Kim, S. J.; Cho, S.-Y.; Choi, J.; Maleski, K.; Lee, B.-J.; Jung, H.-T.; Gogotsi, Y.; Lee, Y.; Ahn, C. W., An investigation into the factors governing the oxidation of two-dimensional Ti3C2 MXene. *Nanoscale* 2019, 11, 8387-8393.
130. Zhang, C. J.; Pinilla, S.; McEvoy, N.; Cullen, C. P.; Anasori, B.; Long, E.; Park, S.-H.; Seral-Ascaso, A.; Shmeliov, A.; Krishnan, D.; Morant, C.; Liu, X.; Duesberg, G. S.; Gogotsi, Y.; Nicolosi, V., Oxidation Stability of Colloidal Two-Dimensional Titanium Carbides (MXenes). *Chemistry of Materials* 2017, 29, 4848-4856.
131. Xia, F.; Lao, J.; Yu, R.; Sang, X.; Luo, J.; Li, Y.; Wu, J., Ambient oxidation of Ti3C2 MXene initialized by atomic defects. *Nanoscale* 2019, 11, 23330-23337.

132. Luzinov, I.; Minko, S.; Tsukruk, V. V., Adaptive and responsive surfaces through controlled reorganization of interfacial polymer layers. *Progress in Polymer Science* 2004, 29, 635-698.
133. Vasudev, M. C.; Anderson, K. D.; Bunning, T. J.; Tsukruk, V. V.; Naik, R. R., Exploration of Plasma-Enhanced Chemical Vapor Deposition as a Method for Thin-Film Fabrication with Biological Applications. *ACS Applied Materials & Interfaces* 2013, 5, 3983-3994.
134. Jiang, L.; Chen, L.; Zhu, L., Electrically conductive membranes for anti-biofouling in membrane distillation with two novel operation modes: Capacitor mode and resistor mode. *Water Research* 2019, 161, 297-307.
135. Baek, Y.; Yoon, H.; Shim, S.; Choi, J.; Yoon, J., Electroconductive Feed Spacer as a Tool for Biofouling Control in a Membrane System for Water Treatment. *Environmental Science & Technology Letters* 2014, 1, 179-184.
136. de Lannoy, C.-F.; Jassby, D.; Gloe, K.; Gordon, A. D.; Wiesner, M. R., Aquatic Biofouling Prevention by Electrically Charged Nanocomposite Polymer Thin Film Membranes. *Environmental Science & Technology* 2013, 47, 2760-2768.
137. Zha, X.-J.; Zhao, X.; Pu, J.-H.; Tang, L.-S.; Ke, K.; Bao, R.-Y.; Bai, L.; Liu, Z.-Y.; Yang, M.-B.; Yang, W., Flexible Anti-Biofouling MXene/Cellulose Fibrous Membrane for Sustainable Solar-Driven Water Purification. *ACS Applied Materials & Interfaces* 2019, 11, 36589-36597.
138. Xiong, Z.-C.; Zhu, Y.-J.; Qin, D.-D.; Chen, F.-F.; Yang, R.-L., Flexible Fire-Resistant Photothermal Paper Comprising Ultralong Hydroxyapatite Nanowires and Carbon Nanotubes for Solar Energy-Driven Water Purification. *Small* 2018, 14, 1803387.
139. Jiang, Q.; Tian, L.; Liu, K.-K.; Tadepalli, S.; Raliya, R.; Biswas, P.; Naik, R. R.; Singamaneni, S., Bilayered Biofoam for Highly Efficient Solar Steam Generation. *Advanced Materials* 2016, 28, 9400-9407.
140. Liu, G.; Shen, J.; Liu, Q.; Liu, G.; Xiong, J.; Yang, J.; Jin, W., Ultrathin two-dimensional MXene membrane for pervaporation desalination. *Journal of Membrane Science* 2018, 548, 548-558.
141. Zhao, M.-Q.; Xie, X.; Ren, C. E.; Makaryan, T.; Anasori, B.; Wang, G.; Gogotsi, Y., Hollow MXene Spheres and 3D Macroporous MXene Frameworks for Na-Ion Storage. *Advanced Materials* 2017, 29, 1702410.
142. Gryta, M., Fouling in direct contact membrane distillation process. *Journal of Membrane Science* 2008, 325, 383-394.
143. Habib, T.; Zhao, X.; Shah, S. A.; Chen, Y.; Sun, W.; An, H.; Lutkenhaus, J. L.; Radovic, M.; Green, M. J., Oxidation stability of Ti3C2Tx MXene nanosheets in solvents and composite films. *npj 2D Materials and Applications* 2019, 3, 8.
144. Zhao, X.; Zha, X.-J.; Pu, J.-H.; Bai, L.; Bao, R.-Y.; Liu, Z.-Y.; Yang, M.-B.; Yang, W., Macroporous three-dimensional MXene architectures for highly efficient solar steam generation. *Journal of Materials Chemistry A* 2019, 7, 10446-10455.
145. Halim, J.; Cook, K. M.; Naguib, M.; Eklund, P.; Gogotsi, Y.; Rosen, J.; Barsoum, M. W., X-ray photoelectron spectroscopy of select multi-layered transition metal carbides (MXenes). *Applied Surface Science* 2016, 362, 406-417.
146. Spinks, A. T.; Dunstan, R. H.; Harrison, T.; Coombes, P.; Kuczera, G., Thermal inactivation of water-borne pathogenic and indicator bacteria at sub-boiling temperatures. *Water Research* 2006, 40, 1326-1332.
147. Wu, Z.; Shang, T.; Deng, Y.; Tao, Y.; Yang, Q.-H., The Assembly of MXenes from 2D to 3D. *Advanced Science* 2020, 7, 1903077.

148. Wang, Z.; Kang, S.; Cao, S.; Krecker, M.; Tsukruk, V. V.; Singamaneni, S., Protein-based functional nanocomposites. *MRS Bulletin* 2020, 45, 1017-1026.
149. Krishnamurthi, V. R.; Rogers, A.; Peifer, J.; Niyonshuti, I.; Chen, J.; Wang, Y., Microampere electric currents caused bacterial membrane damage and two-way leakage in short time. *bioRxiv* 2020, 2020.03.13.991067.
150. Jiang, Q.; Gholami Derami, H.; Ghim, D.; Cao, S.; Jun, Y.-S.; Singamaneni, S., Polydopamine-filled bacterial nanocellulose as a biodegradable interfacial photothermal evaporator for highly efficient solar steam generation. *Journal of Materials Chemistry A* 2017, 5, 18397-18402.
151. Gao, M.; Peh, C. K.; Meng, F. L.; Ho, G. W., Photothermal Membrane Distillation toward Solar Water Production. *Small Methods* n/a, 2001200.
152. Gong, B.; Yang, H.; Wu, S.; Yan, J.; Cen, K.; Bo, Z.; Ostrikov, K. K., Superstructure-Enabled Anti-Fouling Membrane for Efficient Photothermal Distillation. *ACS Sustainable Chemistry & Engineering* 2019, 7, 20151-20158.
153. Zhang, Y.; Li, K.; Liu, L.; Wang, K.; Xiang, J.; Hou, D.; Wang, J., Titanium nitride nanoparticle embedded membrane for photothermal membrane distillation. *Chemosphere* 2020, 256, 127053.
154. Fujiwara, M.; Kikuchi, M., Solar desalination of seawater using double-dye-modified PTFE membrane. *Water Research* 2017, 127, 96-103.
155. Fujiwara, M., Water desalination using visible light by disperse red 1 modified PTFE membrane. *Desalination* 2017, 404, 79-86.
156. Huang, J.; Hu, Y.; Bai, Y.; He, Y.; Zhu, J., Novel solar membrane distillation enabled by a PDMS/CNT/PVDF membrane with localized heating. *Desalination* 2020, 489, 114529.
157. Zhou, X.; Zhao, F.; Guo, Y.; Rosenberger, B.; Yu, G., Architecting highly hydratable polymer networks to tune the water state for solar water purification. *Science Advances* 2019, 5, eaaw5484.
158. Huang, X.; Yu, Y.-H.; de Llergo, Oscar L.; Marquez, S. M.; Cheng, Z., Facile polypyrrole thin film coating on polypropylene membrane for efficient solar-driven interfacial water evaporation. *RSC Advances* 2017, 7, 9495-9499.
159. Fan, Y.; Bai, W.; Mu, P.; Su, Y.; Zhu, Z.; Sun, H.; Liang, W.; Li, A., Conductively monolithic polypyrrole 3-D porous architecture with micron-sized channels as superior salt-resistant solar steam generators. *Solar Energy Materials and Solar Cells* 2020, 206, 110347.
160. Hao, D.; Yang, Y.; Xu, B.; Cai, Z., Efficient solar water vapor generation enabled by water-absorbing polypyrrole coated cotton fabric with enhanced heat localization. *Applied Thermal Engineering* 2018, 141, 406-412.
161. Zhang, L.; Tang, B.; Wu, J.; Li, R.; Wang, P., Hydrophobic Light-to-Heat Conversion Membranes with Self-Healing Ability for Interfacial Solar Heating. *Advanced Materials* 2015, 27, 4889-4894.
162. Xu, Y.; Wang, J.; Yu, F.; Guo, Z.; Cheng, H.; Yin, J.; Yan, L.; Wang, X., Flexible and Efficient Solar Thermal Generators Based on Polypyrrole Coated Natural Latex Foam for Multimedia Purification. *ACS Sustainable Chemistry & Engineering* 2020, 8, 12053-12062.
163. Wang, Z.; Yan, Y.; Shen, X.; Jin, C.; Sun, Q.; Li, H., A wood–polypyrrole composite as a photothermal conversion device for solar evaporation enhancement. *Journal of Materials Chemistry A* 2019, 7, 20706-20712.
164. Huang, W.; Hu, G.; Tian, C.; Wang, X.; Tu, J.; Cao, Y.; Zhang, K., Nature-inspired salt resistant polypyrrole–wood for highly efficient solar steam generation. *Sustainable Energy & Fuels* 2019, 3, 3000-3008.

165. Xiao, C.; Chen, L.; Mu, P.; Jia, J.; Sun, H.; Zhu, Z.; Liang, W.; Li, A., Sugarcane-Based Photothermal Materials for Efficient Solar Steam Generation. *ChemistrySelect* 2019, 4, 7891-7895.
166. Xie, Z.; Zhu, J.; Zhang, L., Three-Dimensionally Structured Polypyrrole-Coated Setaria viridis Spike Composites for Efficient Solar Steam Generation. *ACS Applied Materials & Interfaces* 2021, 13, 9027-9035.
167. Wang, C.; Wang, Y.; Song, X.; Huang, M.; Jiang, H., A Facile and General Strategy to Deposit Polypyrrole on Various Substrates for Efficient Solar-Driven Evaporation. *Advanced Sustainable Systems* 2019, 3, 1800108.
168. Wang, S.; Fan, Y.; Wang, F.; Su, Y.; Zhou, X.; Zhu, Z.; Sun, H.; Liang, W.; Li, A., Potentially scalable fabrication of salt-rejection evaporator based on electrogenerated polypyrrole-coated nickel foam for efficient solar steam generation. *Desalination* 2021, 505, 114982.
169. Wang, X.; Liu, Q.; Wu, S.; Xu, B.; Xu, H., Multilayer Polypyrrole Nanosheets with Self-Organized Surface Structures for Flexible and Efficient Solar–Thermal Energy Conversion. *Advanced Materials* 2019, 31, 1807716.
170. Wang, Y.; Wang, C.; Song, X.; Huang, M.; Megarajan, S. K.; Shaukat, S. F.; Jiang, H., Improved light-harvesting and thermal management for efficient solar-driven water evaporation using 3D photothermal cones. *Journal of Materials Chemistry A* 2018, 6, 9874-9881.
171. Luan, J.; Morrissey, J. J.; Wang, Z.; Derami, H. G.; Liu, K.-K.; Cao, S.; Jiang, Q.; Wang, C.; Kharasch, E. D.; Naik, R. R.; Singamaneni, S., Add-on plasmonic patch as a universal fluorescence enhancer. *Light: Science & Applications* 2018, 7, 29.
172. Delplanque, A.; Henry, E.; Lautru, J.; Leh, H.; Buckle, M.; Nogues, C., UV/ozone surface treatment increases hydrophilicity and enhances functionality of SU-8 photoresist polymer. *Applied Surface Science* 2014, 314, 280-285.
173. Kim, B. H.; Lee, D. H.; Kim, J. Y.; Shin, D. O.; Jeong, H. Y.; Hong, S.; Yun, J. M.; Koo, C. M.; Lee, H.; Kim, S. O., Mussel-Inspired Block Copolymer Lithography for Low Surface Energy Materials of Teflon, Graphene, and Gold. *Advanced Materials* 2011, 23, 5618-5622.
174. Kim, J.; Sohn, D.; Sung, Y.; Kim, E.-R., Fabrication and characterization of conductive polypyrrole thin film prepared by in situ vapor-phase polymerization. *Synthetic Metals* 2003, 132, 309-313.
175. Hanif, Z.; Shin, D.; Choi, D.; Park, S. J., Development of a vapor phase polymerization method using a wet-on-wet process to coat polypyrrole on never-dried nanocellulose crystals for fabrication of compression strain sensor. *Chemical Engineering Journal* 2020, 381, 122700.
176. Buitrago-Sierra, R.; García-Fernández, M. J.; Pastor-Blas, M. M.; Sepúlveda-Escribano, A., Environmentally friendly reduction of a platinum catalyst precursor supported on polypyrrole. *Green Chemistry* 2013, 15, 1981-1990.
177. Šetka, M.; Calavia, R.; Vojkůvka, L.; Llobet, E.; Drbohlavová, J.; Vallejos, S., Raman and XPS studies of ammonia sensitive polypyrrole nanorods and nanoparticles. *Scientific Reports* 2019, 9, 8465.
178. Tabačiarová, J.; Mičušík, M.; Fedorko, P.; Omastová, M., Study of polypyrrole aging by XPS, FTIR and conductivity measurements. *Polymer Degradation and Stability* 2015, 120, 392-401.
179. Aghaei, R.; Eshaghi, A., Optical and superhydrophilic properties of nanoporous silica-silica nanocomposite thin film. *Journal of Alloys and Compounds* 2017, 699, 112-118.
180. Fujiwara, M.; Kikuchi, M., Solar desalination of seawater using double-dye-modified PTFE membrane. *Water Res.* 2017, 127, 96-103.

181. Dongare, P. D.; Alabastri, A.; Pedersen, S.; Zodrow, K. R.; Hogan, N. J.; Neumann, O.; Wu, J.; Wang, T.; Deshmukh, A.; Elimelech, M., Nanophotonics-enabled solar membrane distillation for off-grid water purification. *Proc. Natl. Acad. Sci.* 2017, 114, 6936-6941.
182. Wu, J.; Zodrow, K. R.; Szemraj, P. B.; Li, Q., Photothermal nanocomposite membranes for direct solar membrane distillation. *J. Mater. Chem. A* 2017, 5, 23712-23719.
183. Politano, A.; Argurio, P.; Di Profio, G.; Sanna, V.; Cupolillo, A.; Chakraborty, S.; Arafat, H. A.; Curcio, E., Photothermal membrane distillation for seawater desalination. *Adv. Mater.* 2017, 29.
184. Wu, X.; Jiang, Q.; Ghim, D.; Singamaneni, S.; Jun, Y.-S., Localized heating with a photothermal polydopamine coating facilitates a novel membrane distillation process. *J. Mater. Chem. A* 2018, 6, 18799-18807.
185. Tan, Y. Z.; Wang, H.; Han, L.; Tanis-Kanbur, M. B.; Pranav, M. V.; Chew, J. W., Photothermal-enhanced and fouling-resistant membrane for solar-assisted membrane distillation. *J. Membr. Sci.* 2018, 565, 254-265.
186. Tian, Y.; Zhou, M.; Shi, H.; Gao, S.; Xie, G.; Zhu, M.; Wu, M.; Chen, J.; Niu, Z., Integration of Cell-Penetrating Peptides with Rod-like Bionanoparticles: Virus-Inspired Gene-Silencing Technology. *Nano Letters* 2018.
187. Gong, B.; Yang, H.; Wu, S.; Yan, J.; Cen, K.; Bo, Z.; Ostrikov, K. K., Superstructure-Enabled Anti-Fouling Membrane for Efficient Photothermal Distillation. *ACS Sustainable Chem. Eng.* 2019, 7, 20151-20158.
188. Gong, B.; Yang, H.; Wu, S.; Xiong, G.; Yan, J.; Cen, K.; Bo, Z.; Ostrikov, K., Graphene array-based anti-fouling solar vapour gap membrane distillation with high energy efficiency. *Nano-Micro Lett.* 2019, 11, 51.
189. Cao, S.; Wu, X.; Zhu, Y.; Gupta, R.; Tan, A.; Wang, Z.; Jun, Y.-S.; Singamaneni, S., Polydopamine/hydroxyapatite nanowire-based bilayered membrane for photothermal-driven membrane distillation. *J. Mater. Chem. A* 2020, 8, 5147-5156.
190. Li, W.; Chen, Y.; Yao, L.; Ren, X.; Li, Y.; Deng, L., Fe_3O_4/PVDF-HFP photothermal membrane with in-situ heating for sustainable, stable and efficient pilot-scale solar-driven membrane distillation. *Desalination* 2020, 478, 114288.
191. Zhang, Y.; Li, K.; Liu, L.; Wang, K.; Xiang, J.; Hou, D.; Wang, J., Titanium nitride nanoparticle embedded membrane for photothermal membrane distillation. *Chemosphere* 2020, 127053.

Appendix

Appendix 1

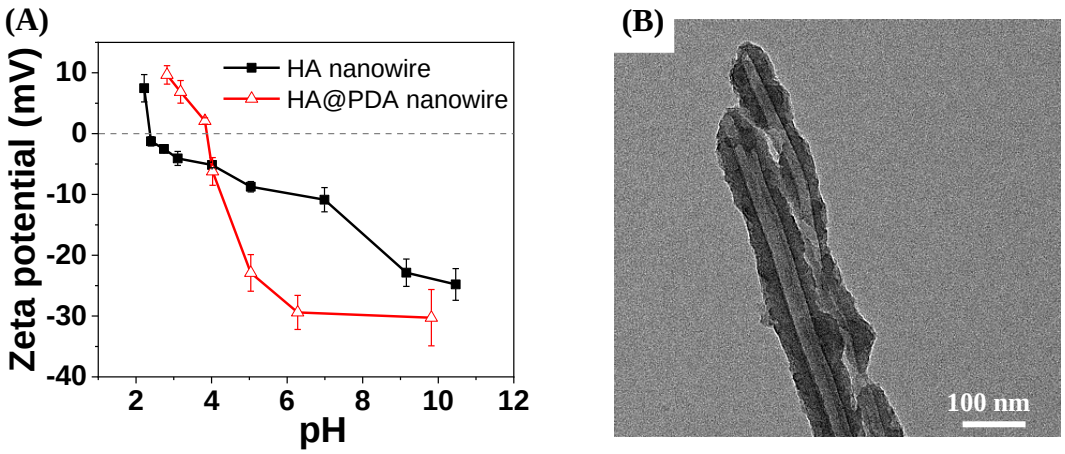

Figure S1.1. (A) Zeta potential of HA nanowires and HA@PDA nanowires. (B) TEM image of PDA hollow tubes.

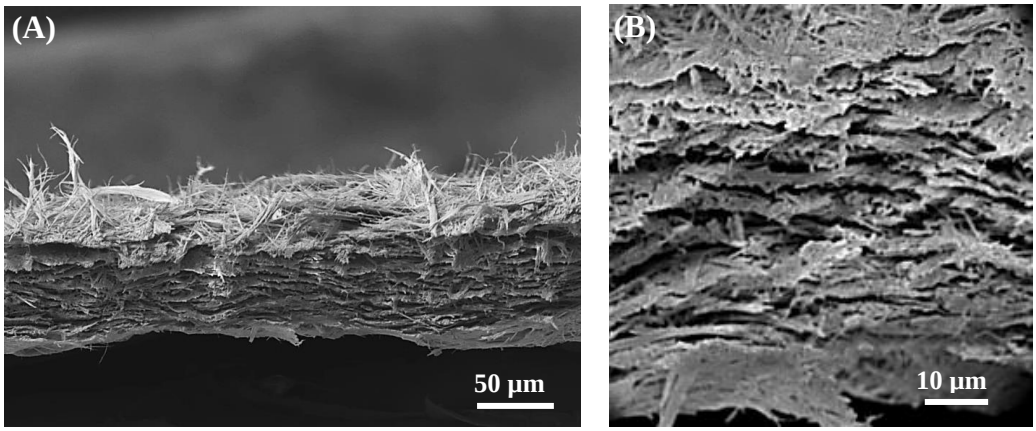

Figure S1.2. The cross-section SEM images of the HA@PDA film in low magnification (A) and high magnification (B).

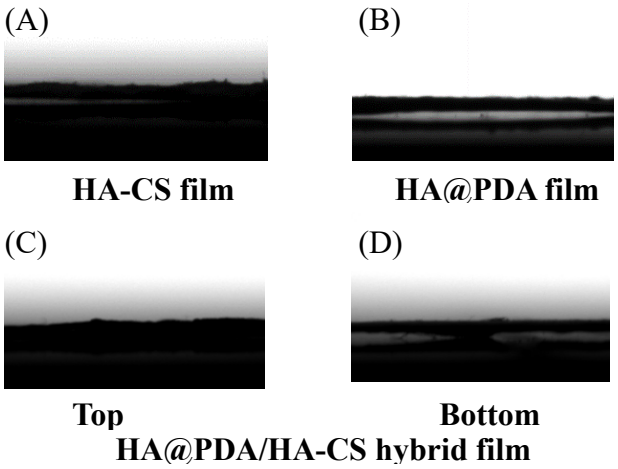

Figure S1.3. Contact angle of representative (A) HA-CS film, (B) HA@PDA film, and (C) top and (D) bottom of HA@PDA/HA-CS bilayered film before FTCS treatment.

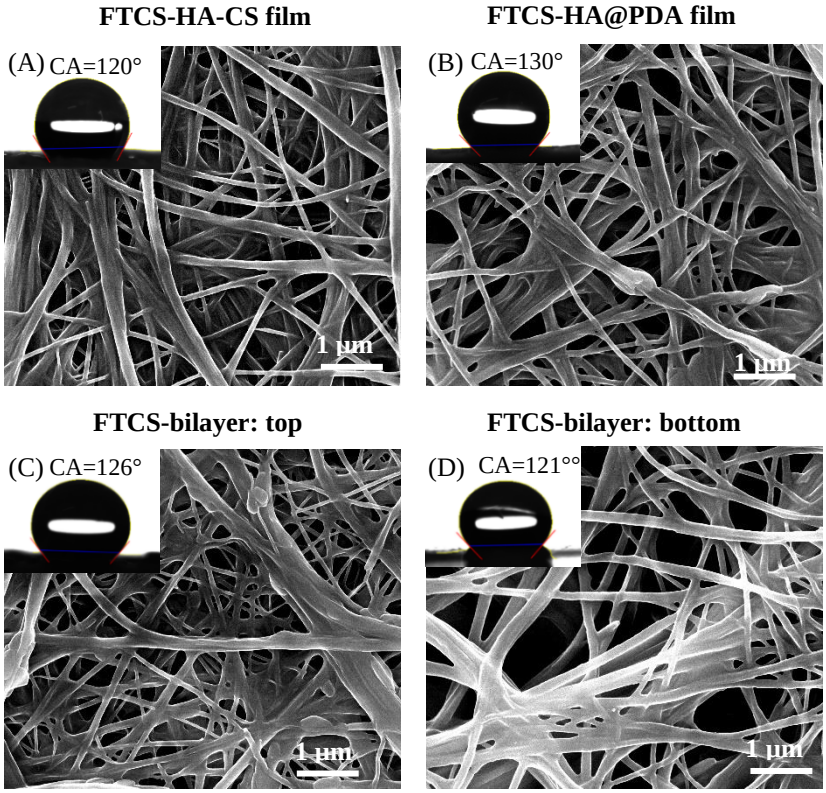

Figure S1.4. SEM images of representative HA-CS film (A), HA@PDA film (B), and top (C) and bottom (D) of HA@PDA/HA-CS bilayered film after FTCS treatment (insets are the contact angles for the corresponding films).

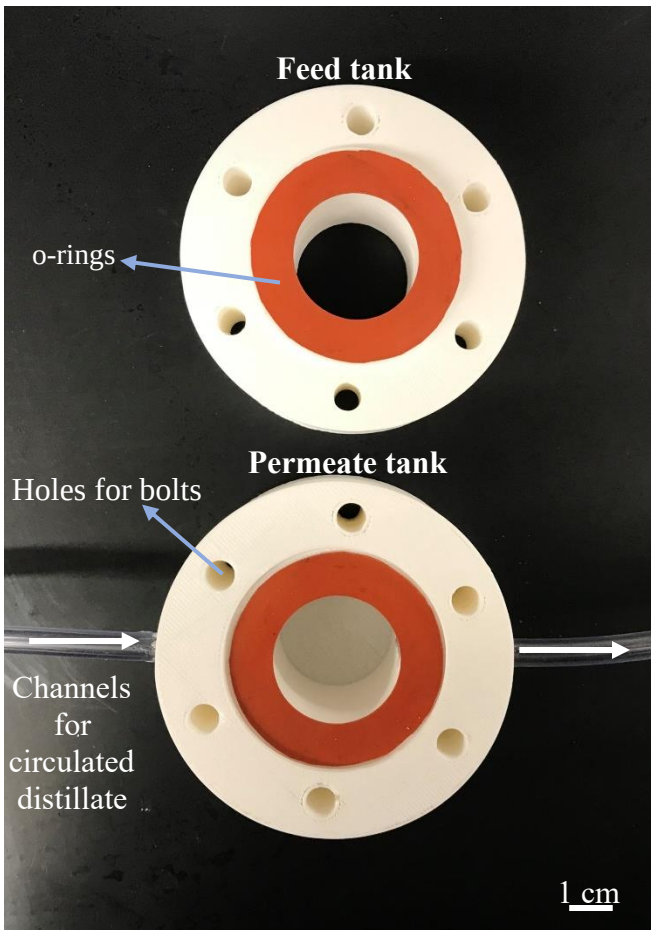

Figure S1.5. Photograph of a 3D-printing module of DCMD for PMD test, comprising of the feed tank and permeate tank. 0.5 M NaCl solution at ambient temperature (20 °C) was circulated at a speed of 3.6 ml•min^{-1} in the feed tank. During PMD test, the feed tank was exposure to simulated sunlight. The distillate at room temperature with a flow rate of 16.2 ml•min^{-1} was circulated in the permeate tank. The photothermal membrane was placed between two pieces of silicone-rubber o-rings to avoid leakage, which was fixed between the feed tank and permeate tank, respectively. Bolts and nots were placed in the holes of the feed tank and permeate tank for fixing, respectively.

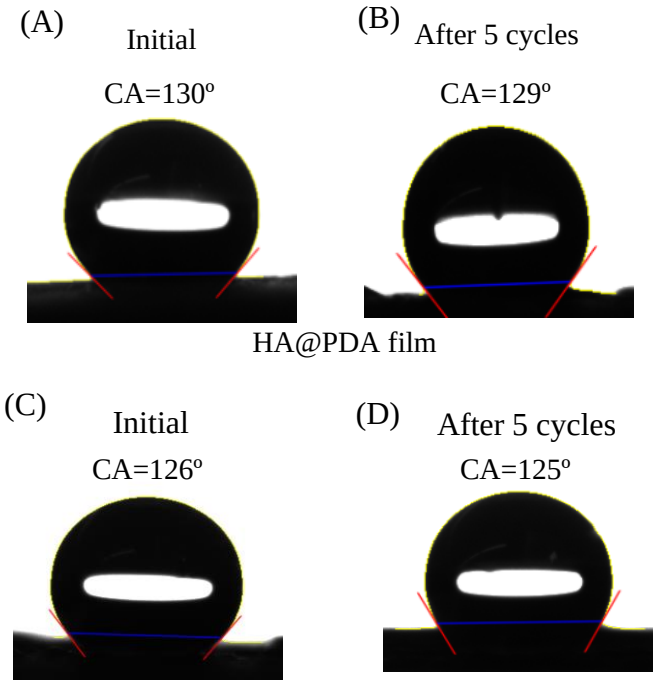

Figure S1.6. Contact angle of representative HA@PDA film before PMD test (A) and after (B) 5 cycles PMD test. Contact angle of HA@PDA/HA-CS bilayered film before PMD test (C) and after (D) 5 cycles PMD test.

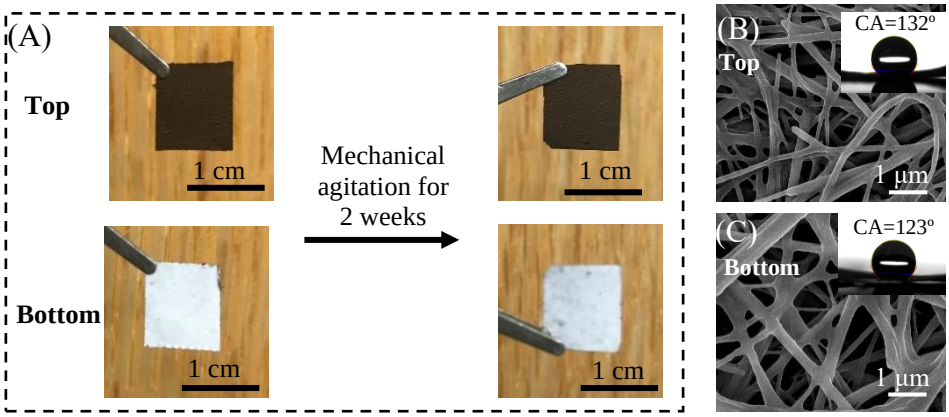

Figure S1.7. Photographs (A) and SEM images (B-C) of the top and bottom layer of HA@PDA/HA-CS film after mechanical agitation for 2 weeks (insets of SEM images are the contact angles for the corresponding film). The film with length of 1 cm and width of 1 cm was placed in a 50 ml test tube filled with water and subjected to a tube rotator for mechanical agitation.

Appendix 2

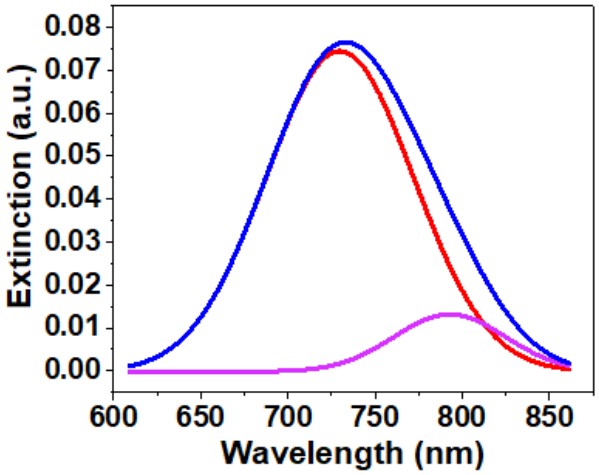

Figure S2.1. Representative extinction spectra of AuNRs with peak deconvolution using two Gaussian peaks.

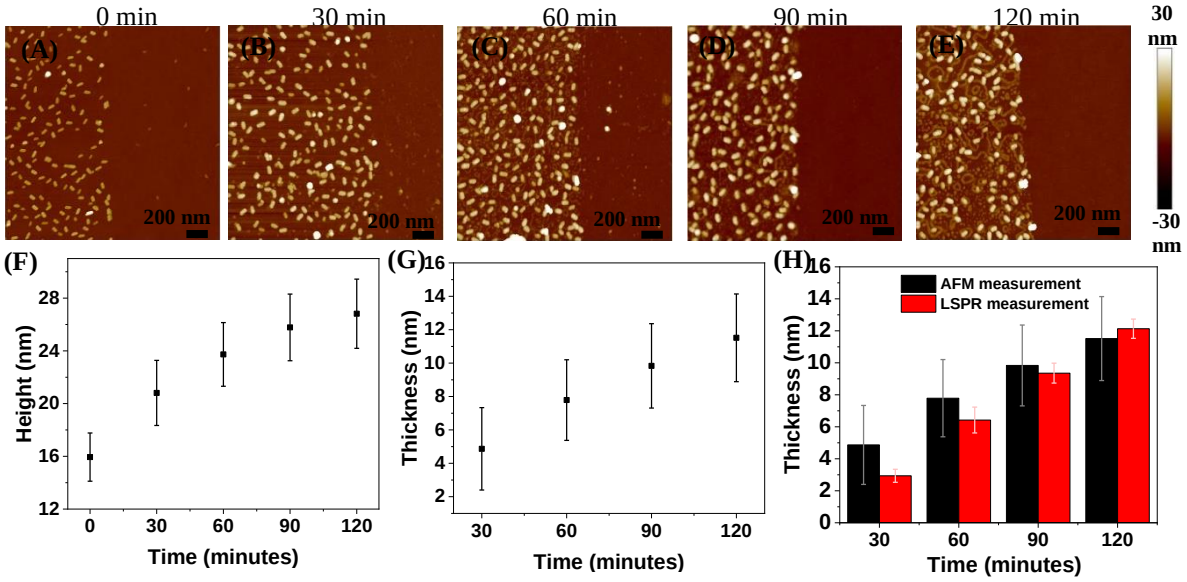

Figure S2.2. AFM images of (A) pure AuNRs on glass substrate, AuNRs substrates after exposure to DA solution for (B) 30 minutes, (C) 60 minutes, (D) 90 minutes, and (E) 120 minutes. (F) Plot of height of AuNRs@PDA and (G) the thickness of PDA on AuNRs after exposure of AuNRs substrates to DA solution for different time. (H) The thickness of PDA on AuNRs obtained from AFM and LSPR measurement.

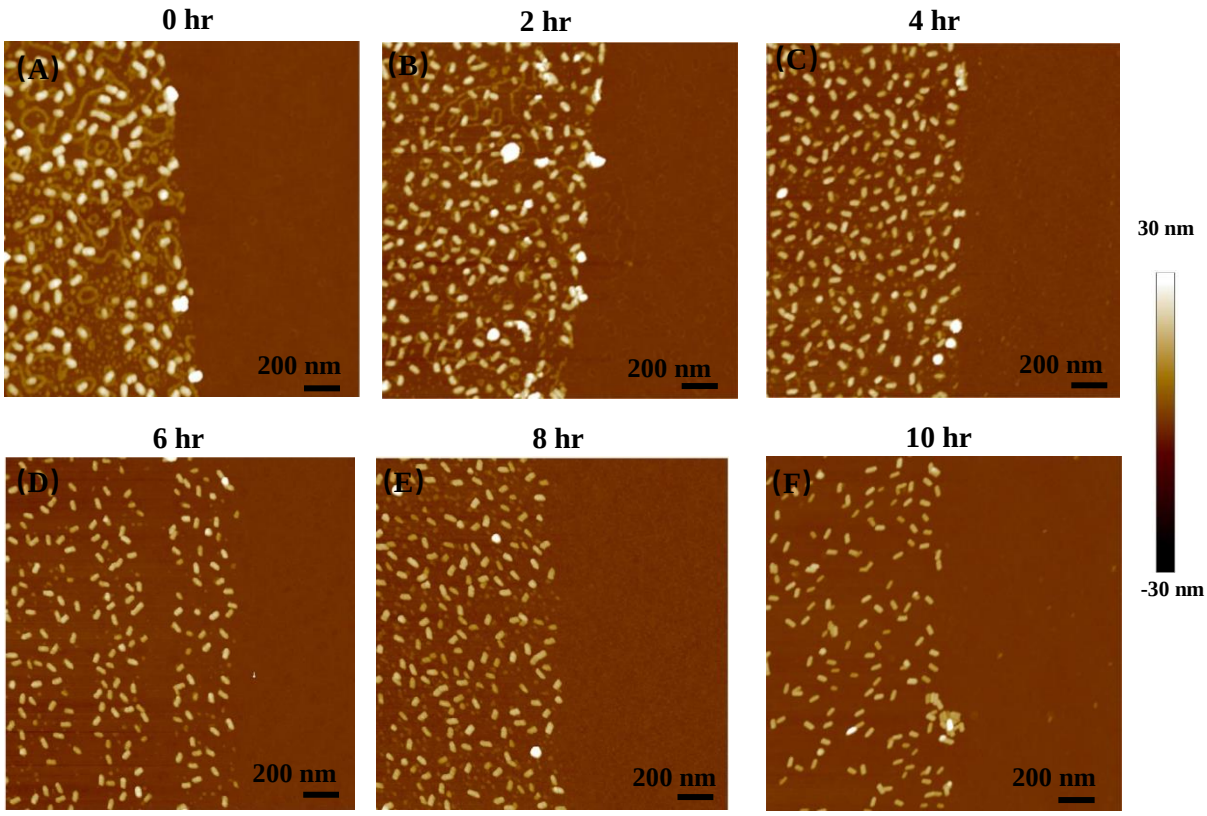

Figure S2.3. AFM images of AuNRs@PDA substrates after exposing to 0.12% H_2O_2 under UV for (A) 0, (B) 2, (C) 4, (D) 6, (E) 8, and (F) 10 hours.

Appendix 3

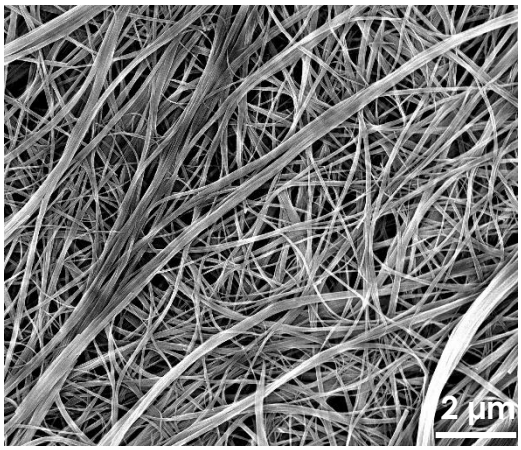

Figure S3.1. SEM image of HA nanowires.

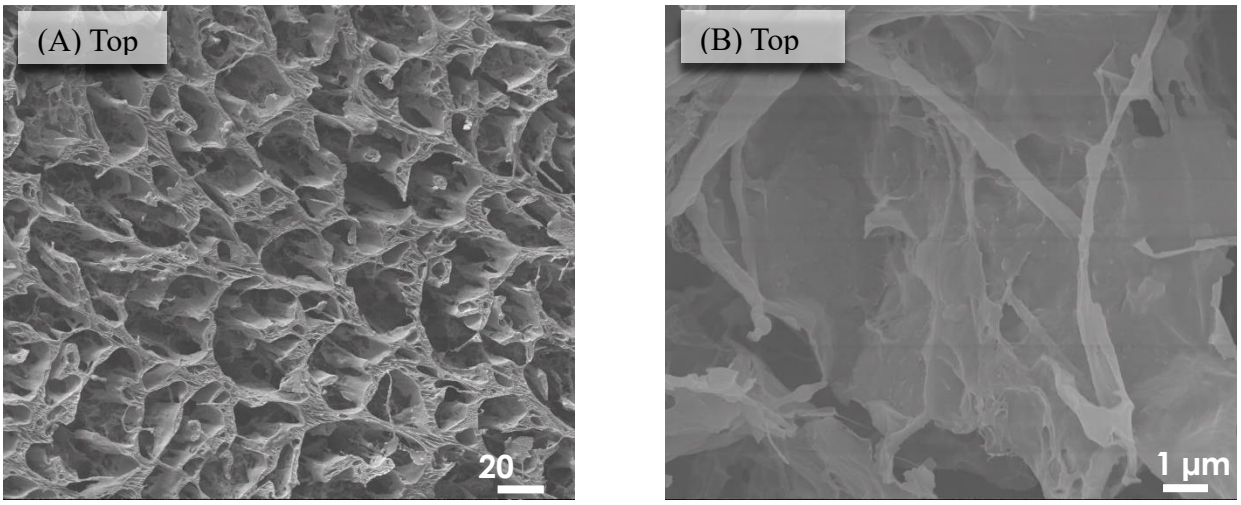

Figure S3.2. SEM images of FTCS-MXene/PVA/HA aerogel in low magnification (A) and high magnification.

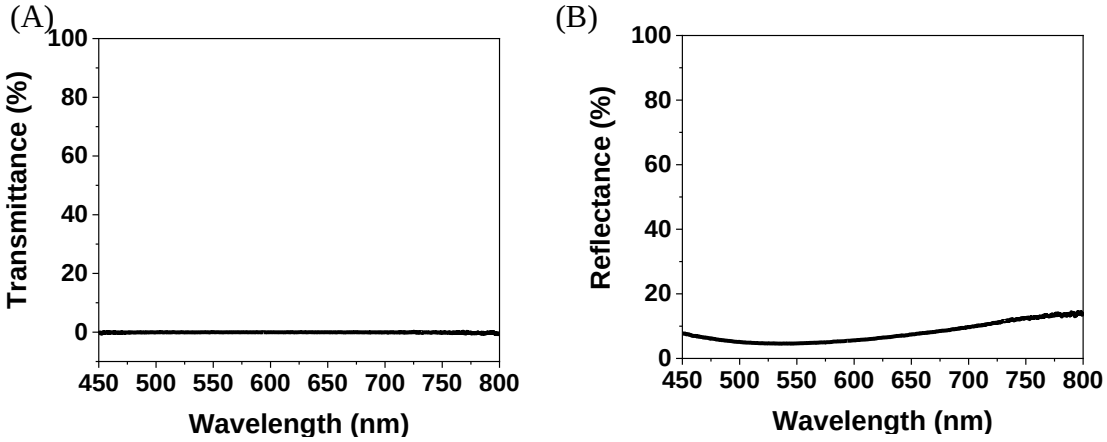

Figure S3.3. (A) Reflectance and (B) transmittance spectra of the compact MXene film (three different points of the sample are measured).

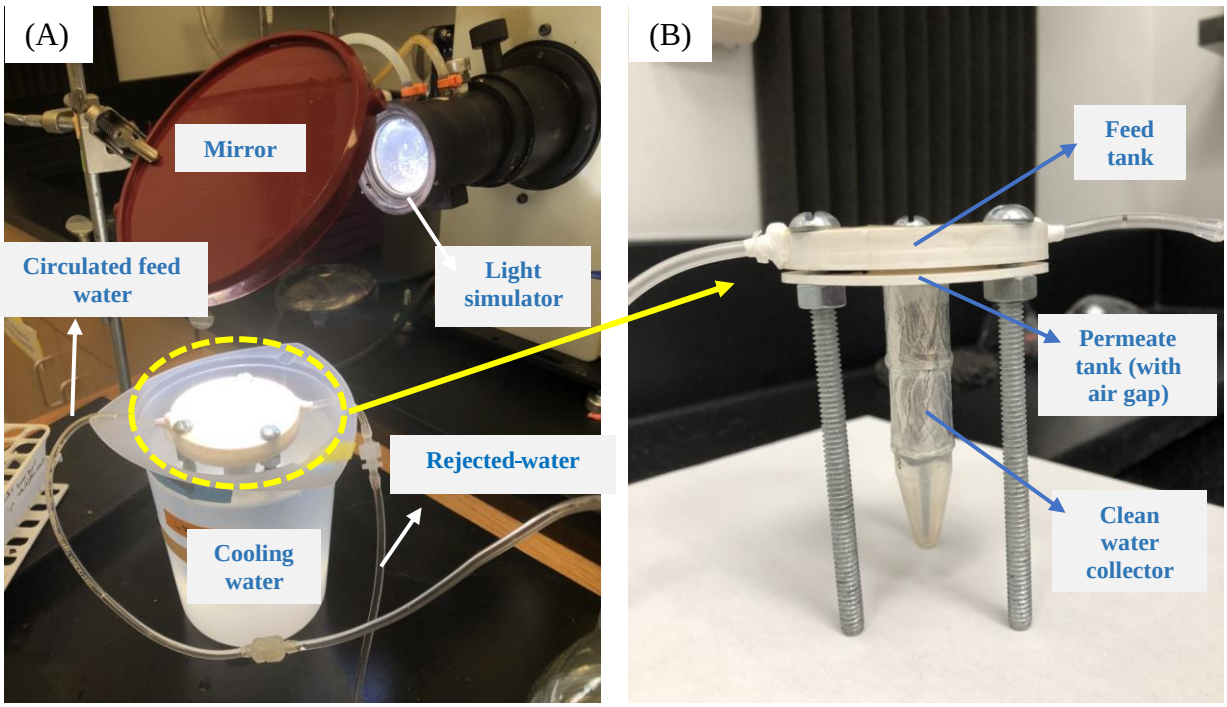

Figure S3.4. Photograph of (A) the PMD test system and (B) a 3D-printed AMD module. The AMD module is comprised of the feed tank and permeate tank with 2 mm air gap. Bolts and nuts are placed in the holes of the feed tank and permeate tank for fixing, respectively. NaCl solution (0.5 M) at ambient temperature is circulated at varying speeds in the feed tank. During PMD test, the feed tank is exposed to simulated sunlight. The photothermal membrane is fixed between the feed tank and permeate tank. Aluminum foil is used as the condensation surface on the permeate side. A 15 mL centrifuge tube, whose wall is cooled by ambient water, is connected to the aluminum foil to collect the condensed distillate.

(A)

(B

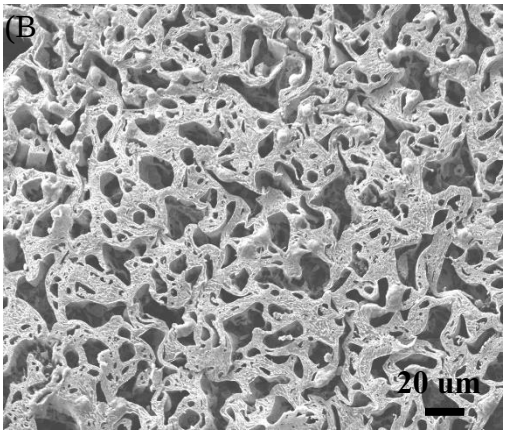

Figure S3.5. (A) Photographs and (B) SEM image of FTCS-MXene/PVA/HA aerogel after mechanical agitation for 2 weeks.

Table S3.1. Comparison of current PMD membranes and performance.

Membrane	**Feed composition**	**Feed T (ºC)**	**Water retention time (min)**	**MD type**	**Irradiation (kW m^{-2})**	**Flux (kg m^{-2} h^{-1})**	**Efficiency (%)**
Dye (DR1) - PTFE[155]	0.59 M NaCl	20	0	AMD*	1	0.24	16
Dye (DR1 + DB14) - PTFE[180]	Artificial seawater	20	0	AMD	1	0.78	53
Carbon Black/PVA-PVDF[181]	0.17 M NaCl	20	0.25	DCMD**	0.7	0.22	21

Carbon Black - PVDF[182]	0.17 M NaCl	35	0.02	DCMD	1.367	0.79-1.51	40-75
Ag NPs-PVDF[183]	0.5 M NaCl	30	NA	VMD ***	23.2 (UV)	25.7	29
FTCS-PDA-PVDF[184]	0.5 M NaCl	20	4.36	DCMD	0.75	0.49	45
rGO/pDA-PTFE[32]	DI water	20	0	AMD	1	0.72	49
MXene-PVDF[185]	0.17 M NaCl	65	0.06	DCMD	7	1	10
Commercial absorber (cermetcoated aluminum alloy substrate)-PVDF-HFP (1 layer) [186]	0.6 M NaCl	20	0	AMD	1	0.73	51
FTCS-CB-PVDF[187]	Natural seawater	20	0.13	DCMD	1	0.78	55

	collected from the Hainan Island						
PEDOT-PSS-graphene–nickel foam[188]	Natural seawater from Hainan Island	20	0	AMD	1	1.1	73****
CNT-carbonized eggshell - PVDF[25]	0.6 M NaCl	20	NA	DCMD	1	1.11	76****
FTCS-PDA-HA[189]	0.5 M NaCl	20	1.57	DCMD	1	0.89	62*****
PDMS/CNT/PVDF (1 layer) [156]	0.6 M NaCl	30-35	0	AMD	1	0.9	60
Fe_3O_4/PVDF-HFP[190]	0.6 M NaCl	26	NA	DCMD	1	0.97	53
TiN-PVA-PVDF[191]	0.6 M NaCl	26	0	AMD	1	0.94	64****

FTCS-PDA/BNC[80]	0.5 M NaCl	20	4.36	DCMD	1	1	68*****
This work	0.5 M NaCl	20	2	AMD	0.8	0.72	61

*AMD: air gap membrane distillation.

**DCMD: direct contact membrane distillation.

***VMD: vacuum membrane distillation.

*****Three references reported higher efficiencies than our work, but their water retention time were either zero or not specified.

******The thermal efficiency of our membrane is comparable with recently reported highly efficient photothermal membranes among PMD systems with similar irradiation, water retention time, and feed water temperatures.

Appendix 4

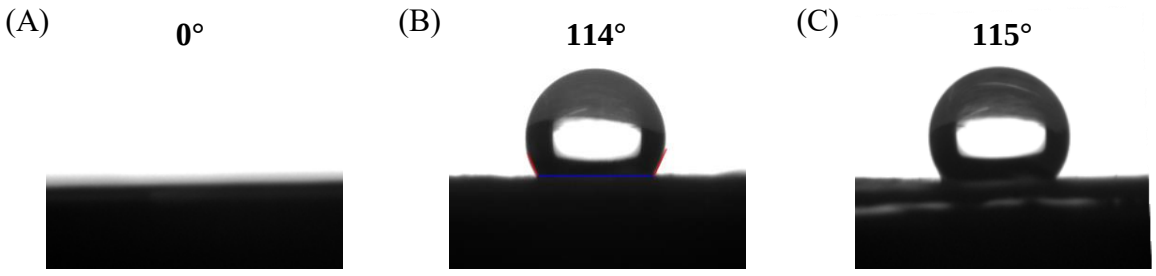

Figure S4.1. The water contact angle of pristine (A) PVDF, (B) PP and (C) PTFE membranes.

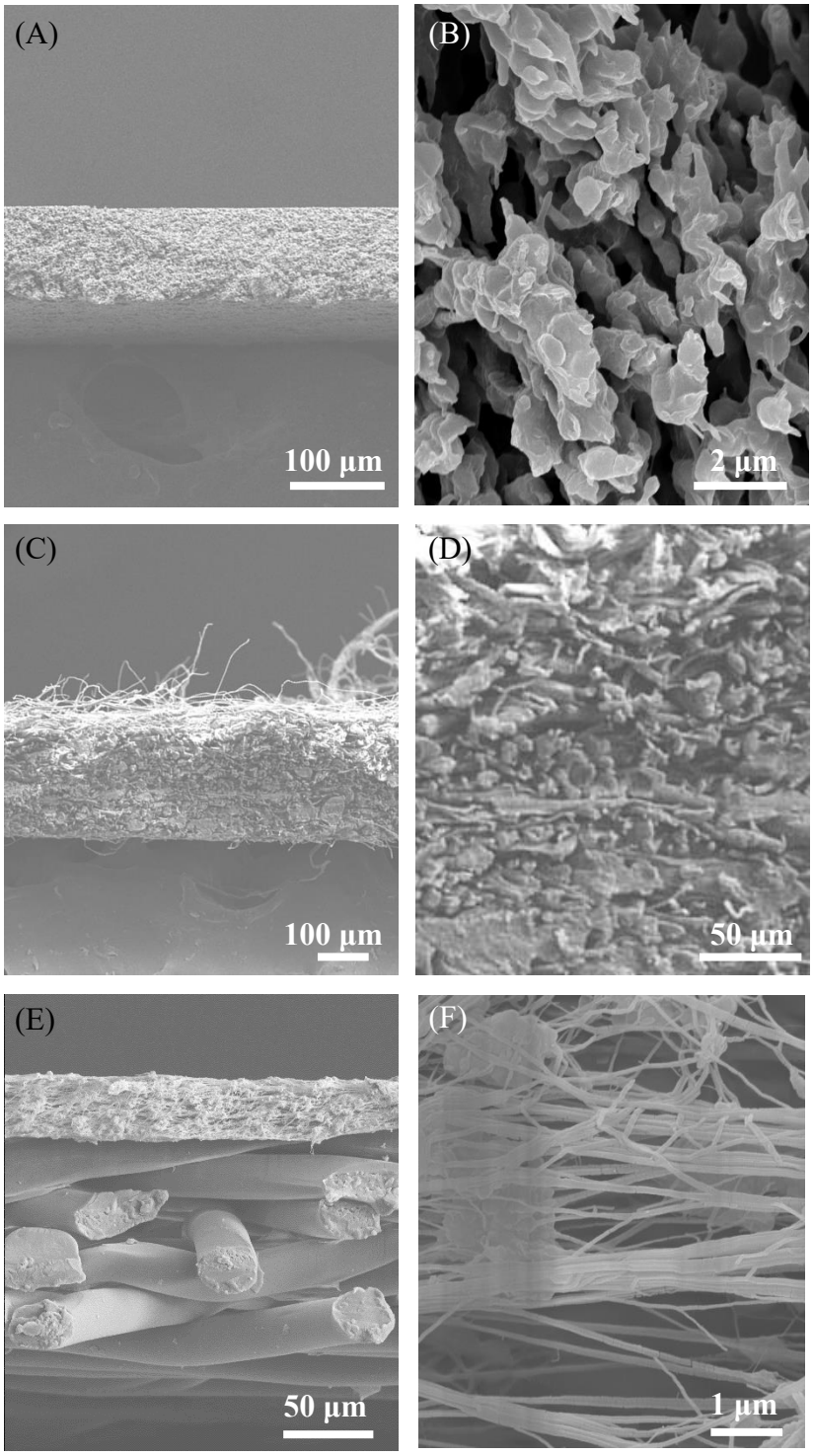

Figure S4.2. The cross-section SEM images of PVDF membranes in low magnification (A) and high magnification (B). The cross-section SEM images of PP membranes in low magnification (C) and high magnification (D). The cross-section SEM images of PTFE membranes in low magnification (E) and high magnification (F).

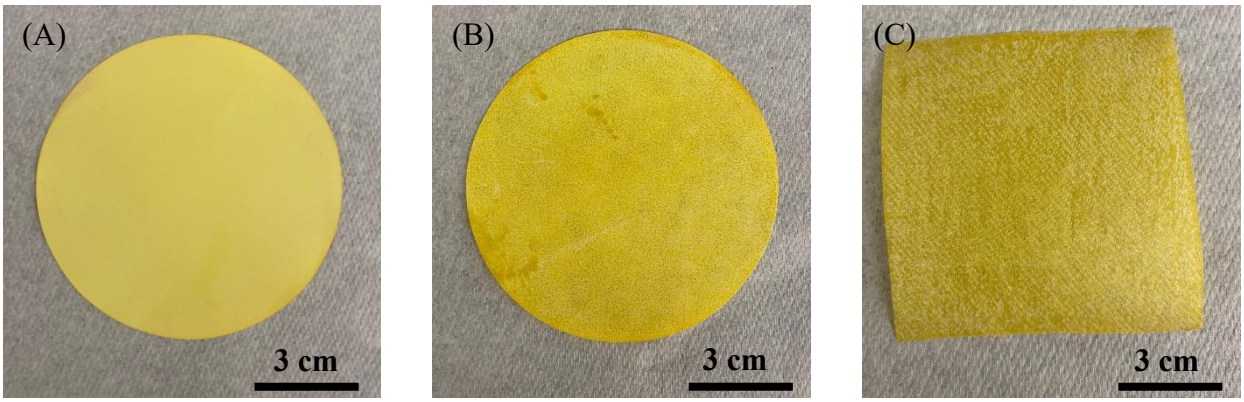

Figure S4.3. The photographs of $FeCl_3$-coated (A) PVDF, (B) PP and (C) PTFE membranes.

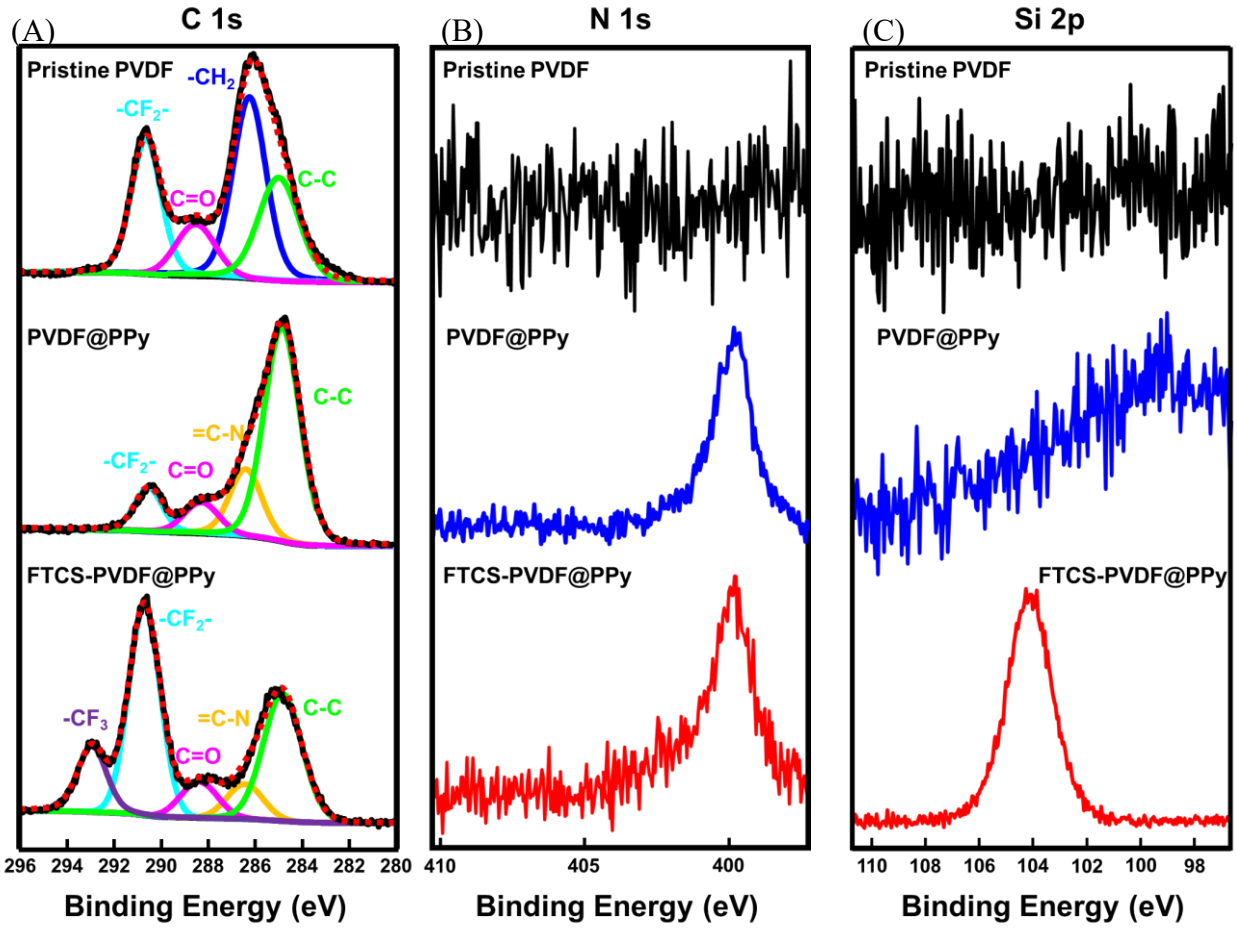

Figure S4.4. XPS spectra of the pristine PVDF, PVDF@PPy, and FTCS-PVDF@PPy membranes, showing the (A) C 1s, (B) N 1s, and (C) Si 2p peaks.

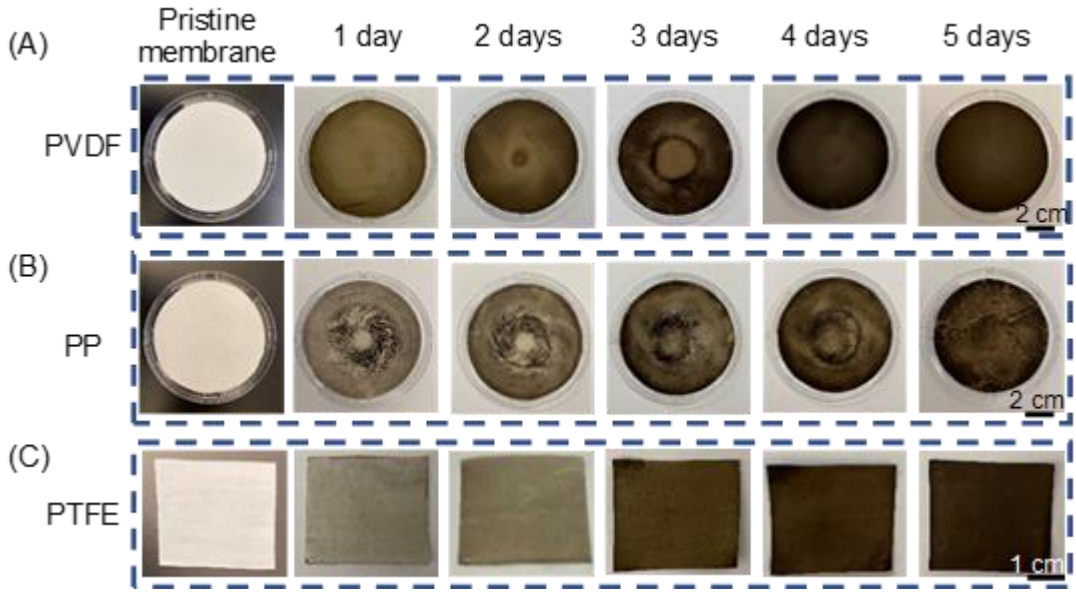

Figure S4.5. Photographs of (A) PVDF, (B) PP, and (C) PTFE membranes during PDA self-polymerization for different days.

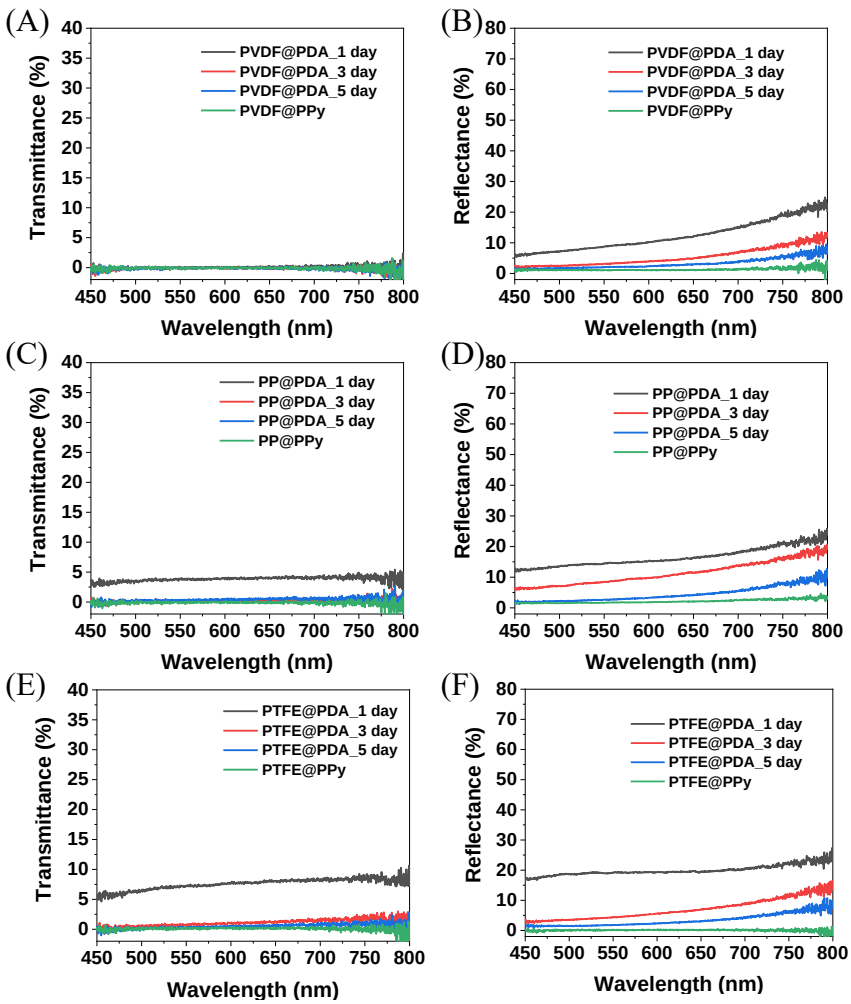

Figure S4.6. (A) Transmittance and (B) reflectance of PVDF@PPy and PVDF membranes after polymerization of dopamine for different time. (C) Transmittance and (D) reflectance of PP@PPy and PP membranes after polymerization of dopamine for different time. (E) Transmittance and (F) reflectance of PTFE@PPy and PTFE membranes after polymerization of dopamine for different time.

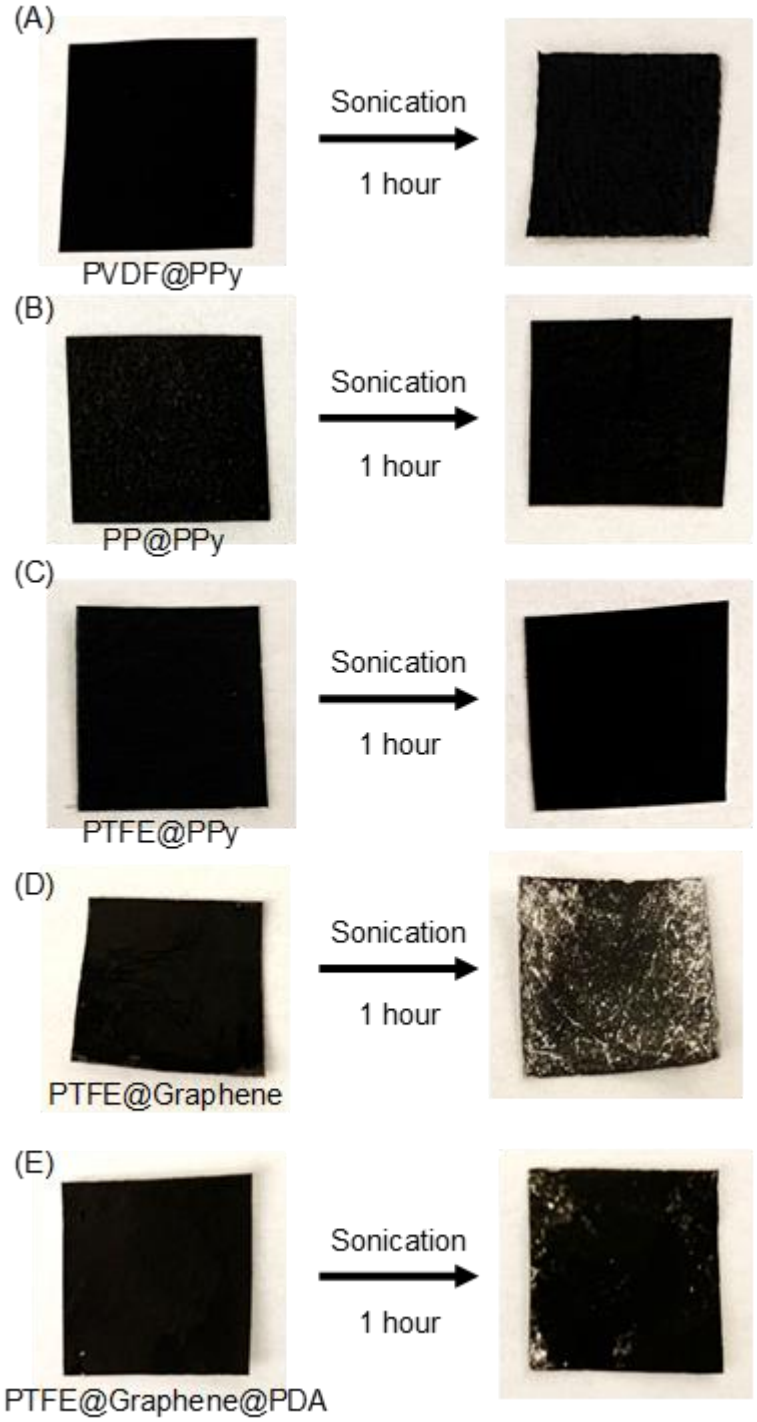

Figure S4.7. Stability of PPy coated membranes. Photographs of (A) PVDF@PPy, (B) PP@PPy, (C) PTFE@PPy, (D) PTFE@Graphene, and (E) PTFE@Graphene@PDA membranes before and after sonication for 1 hour.

Curriculum Vitae

Sisi Cao

Education

2021 Ph.D., Mechanical Engineering and Materials Science, Washington University in St. Louis, St. Louis, USA

Advisor: Prof. Srikanth Singamaneni

Dissertation: Novel Photothermal Materials and Thermally Engineered Membranes for Solar Desalination

2015 M.S., Mechanical Engineering and Materials Science, Washington University in St. Louis, St. Louis, USA

2013 B.Eng., Materials Science and Engineering, Hunan University, China

Research experience

2015-2021 Graduate research assistance, Washington University in St. Louis, St. Louis, USA

2009-2013 Undergraduate research assistant, Hunan University, China

Publications

1. **Cao, S.**; Wu, X.; Zhu, Y.; Gupta, P.; Martinez, A.; Zhang, Y.; Liu, L.; Jun, Y.-S.; Singamaneni, S., MXene aerogel for efficient photothermally-driven membrane distillation with dual-mode antimicrobial capability. Under reviewing in Journal of Materials Chemistry A 2021.

2. Wu, X.;* **Cao, S.**;* Ghim, D.; Jiang, Q.; Singamaneni, S.; Jun, Y.-S., A thermally engineered polydopamine and bacterial nanocellulose bilayer membrane for photothermal membrane distillation with bactericidal capability. Nano Energy 2021, 79, 105353. (*co-first author)

3. **Cao, S.**; Rathi, P.; Wu, X.; Ghim, D.; Jun, Y.-S.; Singamaneni, S., Cellulose Nanomaterials in Interfacial Evaporators for Desalination: A "Natural" Choice. Advanced Materials n/a, 2000922.

4. **Cao, S.**; Wu, X.; Zhu, Y.; Gupta, R.; Tan, A.; Wang, Z.; Jun, Y.-S.; Singamaneni, S., Polydopamine/hydroxyapatite nanowire-based bilayered membrane for photothermal-driven membrane distillation. Journal of Materials Chemistry A 2020, 8, 5147-5156.

5. **Cao, S.**; Jiang, Q.; Wu, X.; Ghim, D.; Gholami Derami, H.; Chou, P.-I.; Jun, Y.-S.; Singamaneni, S., Advances in solar evaporator materials for freshwater generation. Journal of Materials Chemistry A 2019, 7, 24092-24123.

6. **Cao, S.**; Tang, R.; Sudlow, G.; Wang, Z.; Liu, K.-K.; Luan, J.; Tadepalli, S.; Seth, A.; Achilefu, S.; Singamaneni, S., Shape-Dependent Biodistribution of Biocompatible Silk Microcapsules. ACS Applied Materials & Interfaces 2019, 11, 5499-5508.

7. Liang, C.; Luan, J.; Wang, Z.; Jiang, Q.; Gupta, R.; **Cao, S.**; Liu, K.-K.; Morrissey, J. J.; Kharasch, E. D.; Naik, R. R.; Singamaneni, S., Gold Nanorod Size-Dependent Fluorescence Enhancement for Ultrasensitive Fluoroimmunoassays. ACS Applied Materials & Interfaces 2021, 13, 11414-11423.

8. Wang, Z.; Luan, J.; Seth, A.; Liu, L.; You, M.; Gupta, P.; Rathi, P.; Wang, Y.; **Cao, S.**; Jiang, Q.; Zhang, X.; Gupta, R.; Zhou, Q.; Morrissey, J. J.; Scheller, E. L.; Rudra, J. S.; Singamaneni, S., Microneedle patch for the ultrasensitive quantification of protein biomarkers in interstitial fluid. Nature Biomedical Engineering 2021, 5, 64-76.

9. Wang, Z.; Kang, S.; **Cao, S.**; Krecker, M.; Tsukruk, V. V.; Singamaneni, S., Protein-based functional nanocomposites. MRS Bulletin 2020, 45, 1017-1026.

10. Luan, J.; Seth, A.; Gupta, R.; Wang, Z.; Rathi, P.; **Cao, S.**; Gholami Derami, H.; Tang, R.; Xu, B.; Achilefu, S.; Morrissey, J. J.; Singamaneni, S., Ultrabright fluorescent nanoscale labels for the femtomolar detection of analytes with standard bioassays. Nature Biomedical Engineering 2020, 4, 518-530.

11. Tadepalli, S.; **Cao, S.**; Saha, D.; Liu, K.-K.; Chen, A.; Bae, S. h.; Raman, B.; Singamaneni, S., Remote-controlled insect navigation using plasmonic nanotattoos. bioRxiv 2020, 2020.02.10.942540.

12. Jiang, Q.; Ghim, D.; **Cao, S.**; Tadepalli, S.; Liu, K.-K.; Kwon, H.; Luan, J.; Min, Y.; Jun, Y.-S.; Singamaneni, S., Photothermally Active Reduced Graphene Oxide/Bacterial Nanocellulose Composites as Biofouling-Resistant Ultrafiltration Membranes. Environmental Science & Technology 2019, 53, 412-421.

13. Gholami Derami, H.; Jiang, Q.; Ghim, D.; **Cao, S.**; Chandar, Y. J.; Morrissey, J. J.; Jun, Y.-S.; Singamaneni, S., A Robust and Scalable Polydopamine/Bacterial Nanocellulose Hybrid Membrane for Efficient Wastewater Treatment. ACS Applied Nano Materials 2019, 2, 1092-1101.

14. Kolluru, C.; Gupta, R.; Jiang, Q.; Williams, M.; Gholami Derami, H.; **Cao, S.**; Noel, R. K.; Singamaneni, S.; Prausnitz, M. R., Plasmonic Paper Microneedle Patch for On-Patch Detection of Molecules in Dermal Interstitial Fluid. ACS Sensors 2019, 4, 1569-1576.

15. Yilmaz, H.; Bae, S. H.; **Cao, S.**; Wang, Z.; Raman, B.; Singamaneni, S., Gold-Nanorod-Based Plasmonic Nose for Analysis of Chemical Mixtures. ACS Applied Nano Materials 2019, 2, 3897-3905.

16. Jun, Y.-S.; Wu, X.; Ghim, D.; Jiang, Q.; **Cao, S.**; Singamaneni, S., Photothermal Membrane Water Treatment for Two Worlds. Accounts of Chemical Research 2019, 52, 1215-1225.

17. Gupta, P.; Luan, J.; Wang, Z.; **Cao, S.**; Bae, S. H.; Naik, R. R.; Singamaneni, S., On-Demand Electromagnetic Hotspot Generation in Surface-Enhanced Raman Scattering Substrates via "Add-On" Plasmonic Patch. ACS Applied Materials & Interfaces 2019, 11, 37939-37946.

18. Morrissey, J.; Maofeng, Z.; Luan, J.; Wang, Z.; **Cao, S.**; Singamaneni, S., SAT-144 AN ULTRASENSITIVE SURFACE ENHANCED RAMAN SCATTERING (SERS)-BASED ASSAY FOR KIDNEY INJURY MOLECULE-1 (KIM-1). Kidney International Reports 2019, 4, S64-S65.

19. Ghim, D.; Jiang, Q.; **Cao, S.**; Singamaneni, S.; Jun, Y.-S., Mechanically interlocked 1T/2H phases of MoS2 nanosheets for solar thermal water purification. Nano Energy 2018, 53, 949-957.

20. Luan, J.; Morrissey, J. J.; Wang, Z.; Derami, H. G.; Liu, K.-K.; **Cao, S.**; Jiang, Q.; Wang, C.; Kharasch, E. D.; Naik, R. R.; Singamaneni, S., Add-on plasmonic patch as a universal fluorescence enhancer. Light: Science & Applications 2018, 7, 29.

21. Wang, C.; Sudlow, G.; Wang, Z.; **Cao, S.**; Jiang, Q.; Neiner, A.; Morrissey, J. J.; Kharasch, E. D.; Achilefu, S.; Singamaneni, S., Metal-Organic Framework Encapsulation Preserves the Bioactivity of Protein Therapeutics. Advanced Healthcare Materials 2018, 7, 1800950.

22. Tadepalli, S.; Yim, J.; **Cao, S.**; Wang, Z.; Naik, R. R.; Singamaneni, S., Metal–Organic Framework Encapsulation for the Preservation and Photothermal Enhancement of Enzyme Activity. Small 2018, 14, 1702382.

23. Jiang, Q.; Chandar, Y. J.; **Cao, S.**; Kharasch, E. D.; Singamaneni, S.; Morrissey, J. J., Rapid, Point-of-Care, Paper-Based Plasmonic Biosensor for Zika Virus Diagnosis. Advanced Biosystems 2017, 1, 1700096.

24. Jiang, Q.; Gholami Derami, H.; Ghim, D.; **Cao, S.**; Jun, Y.-S.; Singamaneni, S., Polydopamine-filled bacterial nanocellulose as a biodegradable interfacial photothermal evaporator for highly efficient solar steam generation. Journal of Materials Chemistry A 2017, 5, 18397-18402.

25. Tadepalli, S.; Hamper, H.; Park, S. H.; **Cao, S.**; Naik, R. R.; Singamaneni, S., Adsorption Behavior of Silk Fibroin on Amphiphilic Graphene Oxide. ACS Biomaterials Science & Engineering 2016, 2, 1084-1092.

26. Tian, L.; Liu, K.-K.; Fei, M.; Tadepalli, S.; **Cao, S.**; Geldmeier, J. A.; Tsukruk, V. V.; Singamaneni, S., Plasmonic Nanogels for Unclonable Optical Tagging. ACS Applied Materials & Interfaces 2016, 8, 4031-4041.